Stony Brook University

Theory of nuclear matter of neutron stars and core collapsing supernovae

A Dissertation Presented

by

Yeunhwan Lim

to

The Graduate School

in Partial Fulfillment of the

Requirements

for the Degree of

Doctor of Philosophy

in

Physics

Stony Brook University

August 2012

Stony Brook University

The Graduate School

Yeunhwan Lim

We, the dissertation committee for the above candidate for the Doctor of Philosophy degree, hereby recommend acceptance of this dissertation.

James M. Lattimer – Dissertation Advisor
Professor, Department of Physics and Astronomy

Michael Zingale – Chairperson of Defense
Associate Professor, Department of Physics and Astronomy

Alan C. Calder
Assistant Professor, Department of Physics and Astronomy

Dominik Schneble
Associate Professor, Department of Physics and Astronomy

Daniel M. Davis
Professor, Department of Geosciences
Department of Geosciences, SUNY Stony Brook

This dissertation is accepted by the Graduate School.

Charles Taber
Interim Dean of the Graduate School

Abstract of the Dissertation

Theory of nuclear matter of neutron stars and core collapsing supernovae

by

Yeunhwan Lim

Doctor of Philosophy

in

Physics

Stony Brook University

2012

Nuclear astrophysics is essential to microphysics for the complex hydrodynamics simulation of numerical supernovae explosions and neutron star merger calculations. Because many aspects of equation of state (hereafter, EOS) including symmetry and thermal properties are uncertain and not well constrained by experiments, it is important to develop EOS with easily adjustable parameters.

The purpose of this thesis is to develop the nuclear matter theory and an EOS code for hot dense matter. This thesis has two major parts. In the first part, we develop a Finite-Range Thomas Fermi (hereafter, FRTF) model for supernovae and neutron star matter based on the nuclear model of Seyler and Blanchard, and Myers and Swiatecki. The nuclear model is extended to finite temperature and a Wigner-Seitz geometry to model dense matter. We also extend the model to include additional density dependent interactions to better fit known nuclear incompressibilities, pure neutron matter, and the nuclear optical potential.

Using our model, we evaluate nuclear surface properties using a semi-infinite interface. The coexistence curve of nuclear matter for two-phase equilibrium is calculated. Furthermore we calculate energy, radii, and surface thickness of closed shell nuclei in which the spin-orbit interactions can be neglected. To get an optimized parameter set for FRTF, we explore the allowed ranges of symmetry

energy and the density derivative of symmetry energy. We summarize recent experimental results, astrophysical inference, and theoretical pure neutron matter calculations. The correlation between symmetry energy and the surface symmetry energy in liquid droplet model is also obtained. The beta equilibrium matter is used to model the neutron star crust.

The second part of the thesis is devoted to construction of a code to compute the nuclear EOS for hot dense matter that would be distributed to astrophysics community. With this code, users will be able to generate tables with adjustable parameters describing the symmetry, incompressibility, and thermal properties of nuclear matter. We use the liquid droplet approach to generate thermodynamically consistent nuclear EOS. table. Compared to previous attempts, we include neutron skin, Coulumb diffusion, and Coulomb exchange. In addition, we compute the surface tension as a function of proton fraction and temperature consistently with the bulk energy. For comparison, we generate an EOS table using the SLy4 non-relativistic Skyrme force model. For both FRTF and SLy4, more than 10 % of entries of EOS tables consists of nuclei, alpha particles, and nucleons.

To Jaenyeong, Jonghyun, and Jongbum

Contents

List of Figures

Symbols

Nuclear Physics Symbol

$\mathcal{E}$	energy density (MeV/fm^3)
p	pressure (MeV/fm^3)
B	binding energy per baryon at saturation density (MeV)
K	nuclear incompressibility (MeV)
K'	density derivative of nuclear incompressibility (MeV)
ρ	baryon number density (fm^{-3})
ρ_0	nuclear saturation density (fm^{-3})
T	temperature (MeV)
$\mu_n(\mu_p)$	neutron (proton) chemical potential (MeV)
$\tau_n(\tau_p)$	neutron (proton) momentum density (1/fm^5)
$\mathcal{H}_B, \mathcal{H}_g, \mathcal{H}_C, \mathcal{H}_J$	Hamiltonian density contribution from bulk, gradient, Coulomb, and spin-orbit coupling respectively
$t_0, t_1, t_2, t_3, x_0, x_1, x_2, x_3$	coefficients in the Skyrme force model
Q_{nn}, Q_{pp}, Q_{np}	density gradient interaction coefficients
$\mathbf{J}$, $\mathbf{J}_n$, $\mathbf{J}_p$	spin-orbit interaction
ψ	nuclear wave function
σ	Pauli spin matrix
$g_\omega, g_\rho, g_\sigma$	coupling constant in the relativistic mean field model
A_μ	photon field

ρ, ω_μ, σ	ρ, ω, σ field respectively
$m_\rho, m_\omega, m_\sigma$	mass of ρ, ω, and σ boson respectively
$\mathbf{B}_{\mu\nu}, F_{\mu\nu}$	tensor field
P_o	zero temperature Fermi-momentum (MeV/c)
T_o	zero temperature kinetic energy (MeV)
W	total interaction energy (MeV)
a	nuclear diffuseness parameter
r_{12}, p_{12}	relative distance and relative momentum
$C_{L,U}$	interaction energy density functional
$\alpha_{L,U}, \beta_{L,U}, \sigma_{L,U}, \eta_{L,U}$	coefficient in the finite range Thomas Fermi model
$\langle g \rangle$	Gaussian finite range integral
$f(r_{12})$	Yukawa-like distance function
$\bar{\rho}, \hat{\rho}$	average density
I_1, I_2, I_4	momentum integrals
$\tilde{g}$	finite range integral
$F_{1/2}, F_{3/2}$	Fermi integral
m_t^*	effective mass for type t nucleon
V_t	nuclear potential for type t nucleon
$U_n(r, p)$	optical potential
Ψ_t	degeneracy parameter for type t nucleon
p	pressure (MeV/fm^3)
f_t	Fermi-Dirac distribution function for type t nucleon
S	entropy density (k_B/fm^3)
S_v	symmetry energy (MeV)
$L(= 3S_v')$	density derivative of symmetry energy (MeV)
ω	surface tension of nuclear matter (MeV/fm^2)

ω_δ	Taylor expansion coefficient in surface tension
t_{90-10}	surface thickness of 90% -10% nuclear matter density
Q	gradient term in finite range Thomas Fermi model
t	neutron skin thickness (fm)
T_c	critical temperature (MeV)
p_N	pure neutron matter pressure (MeV/fm^3)
$V_{1L,U}, V_{2L,U}, V_{3L,U}, v_{1L,U}, v_{2L,u}, v_{3L,U}, t_3$	coefficient for Gaussian type nuclear force model
k_f	Fermi wave number
D_{nn}, D_{np}, D_{pp}	gradient terms in thermodynamic instability
ν	metric function in general relativity
I	momentum of inertia of rotating neutron star
$\rho_i^{\text{in,out}}$	density of in and out of nucleus in parameterized density profile
E_s	surface energy in liquid droplet model
E_{diff}	Coulomb diffuseness coefficient in liquid droplet model
E_{ex}	Coulomb exchange coefficient in liquid droplet model
E_{shell}	nuclear shell effect energy in liquid droplet model
S_s	surface symmetry energy
N_s	number of neutrons on the surface of nuclei in liquid droplet model
Δ	nuclear energy gap (MeV)
f_N, f_o, f_α	free energy per baryon contribution from heavy nuclei, outside nucleons, alpha particles
$f_{\text{bulk}}, f_{\text{Coul}}, f_{\text{surf}}, f_{\text{trans}}$	free energy per baryon from bulk, Coulomb interaction, surface, and translation repectively
ν_t	skin density of type t nucleon in liquid droplet model
r_N	radius of heavy nuclei in liquid droplet model
Y_p	total proton fraction in liquid droplet model

$x_{i,o}$	proton fraction of heavy nuclei, outside nucleons
ρ_α	alpha particle density
v_α	volume of alpha particle
B_α	alpha particle binding energy
u	volume fraction of heavy nuclei to Wigner-Seitz cell in liquid droplet model
$h(x,T)$	surface tension function in liquid droplet model
$\hat{\mu}$	$\mu_n - \mu_p$
$s(u), c(u), D(u), \mathcal{D}(u)$	geometric functions in liquid droplet model

List of Tables

Acknowledgements

I deeply appreciate my advisor, Prof. James M. Lattimer, that he taught me nuclear astrophysics and how I could simplify the complex problems. His door was always open and I could get invaluable advice.

I would also like to thank Prof. Alan Calder who always listened to my questions and helped me to get answers. I appreciate Prof. Mike Zingale for serving as my committee chairperson and trying to help me when I had important things. I also want to thank Prof. Dominik Schneble and Prof. Daniel M. Davis for serving on my thesis committee.

My nuclear astrophysics group friends (Dr. Chris Malone, Dr. Aaron Jackson, Brendan, Adam, Rahul, ...) were always there for me. I can't express my appreciation enough.

Last but not least, I would like to thank my family, Jaenyeong, Jonghyun, and Jongbum. They always made me happy and encouraged me to finish my Ph.D.

Chapter 1

Introduction

Stars give us light by burning hydrogen fuel. The simple Einstein's equation, $E = mc^2$ is behind sun's energy. Hydrogen turns into helium and helium burns into carbon, nitrogen, and oxygen. Finally, the neutron rich elements iron is formed. After an iron core forms, a star begins to collapse since it cannot support itself against gravitational collapse. During this process, which as known as a Type II supernova explosion, a neutron star is formed if the mass of main sequence star is about $8 \sim 20$ $M_\odot$. Stars with greater than 20 $M_\odot$ are thought to form black holes. An enormous amount of energy ($\sim 10^{53}$ erg) is released from supernova explosion. The source of the energy is gravitational binding energy and the most of the energy is carried away by neutrinos. Right after core collapse, the initial temperature of neutron star is believed to be 10^{11}K [38]. Neutron stars cool down quickly by neutrino emission. After the temperature drops below the Fermi temperature, neutron star is cold.
The existence of neutron stars was first suggested by Walter Baade and Fritz Zwicky in 1934 [38] only a year after the discovery of neutrons by James Chadwick. Landau, Bohr, and Rosenfeld discussed the idea of one giant nuclei in the core of a star before the discovery of neutron [67] but their paper was not published.
A neutron star has mostly neutrons ($\sim$90%), protons and electrons. If the chemical potential of electrons is greater than the rest mass of kaon, there might be kaon condensation so the kaon replaces the role of electrons for charge neutrality. As the density increases, the chemical potential of neutrons and protons can be greater than the rest mass of hyperons, then hyperons ($\Sigma^{+,-,0}$, Λ, Ξ^-) might appear.
A neutron star is divided into an inner core, outer core, inner crust and outer crust. The outer crust consists of lattice nuclei with free gas of electrons. As density increase, the chemical potential of neutrons becomes greater than zero and neutrons drip out of heavy nuclei. Thus, the inner crust has a free gas of neutrons with lattice nuclei. Between the boundary of inner crust and outer core, heavy nuclei become exotic. Because of high pressure, the spherical nuclei become oblate to minimize the energy, and as the density increases more, oblate nuclei merge together to become a cylindrical phase, a cylindrical phase becomes a slab phase, a slab phase turns into a cylindrical hole, and a cylindrical hole becomes a spherical hole, and finally a spherical hole can become uniform nuclear matter. The outer core thus does not have any nuclei structure. The inner core, which is more dense than the outer core, is believed to have exotic nuclear matter. Some nuclear physicists argue that there might be quark matter in the core of neutron stars. Many of them use the MIT bag model

to explain the existence of quark matter but it's still an open question. MIT bag model describes the quarks are freely moving in a bag. If the distance between quarks is increases, the force increases so strong that they cannot get out of the bag. To maintain the bag, negative pressure is introduced, which is known as the bag constant (B). Since we cannot do any experiment to reveal the existence of quark matter at such high densities on the earth yet, the theoretical prediction of quark matter depends on the parameters, especially the bag constant in quark matter.

One thing is for sure is that the densities of neutron stars are extremely high. It is believed that the central density of the core in neutron stars is $4\rho_0 \sim 10\rho_0$[†], where a ρ_0 is the nuclear saturation density, 3×10^{14}g/cm^3.

The typical radius of neutron star is around 10km. The mass of neutron is about 1.2M$_\odot$ to 2.0 M$_\odot$. Since neutron stars are so compact, the surface gravity of neutron stars is extremely high, about 2×10^{11} times earth gravity. In these conditions, general relativity is essential to find out the mass-radius relation of neutron stars. The Tolman-Oppenhimer-Volkov (TOV) equation solves the internal structure of spherically symmetric neutron stars. Thus, the nuclear physics and the TOV equation play together to give mass-relation of neutron stars. The nuclear physics beyond ρ_0 is not known well and the central density is much higher than ρ_0, various nuclear force models give different mass-radius relation of neutron stars. Fig.

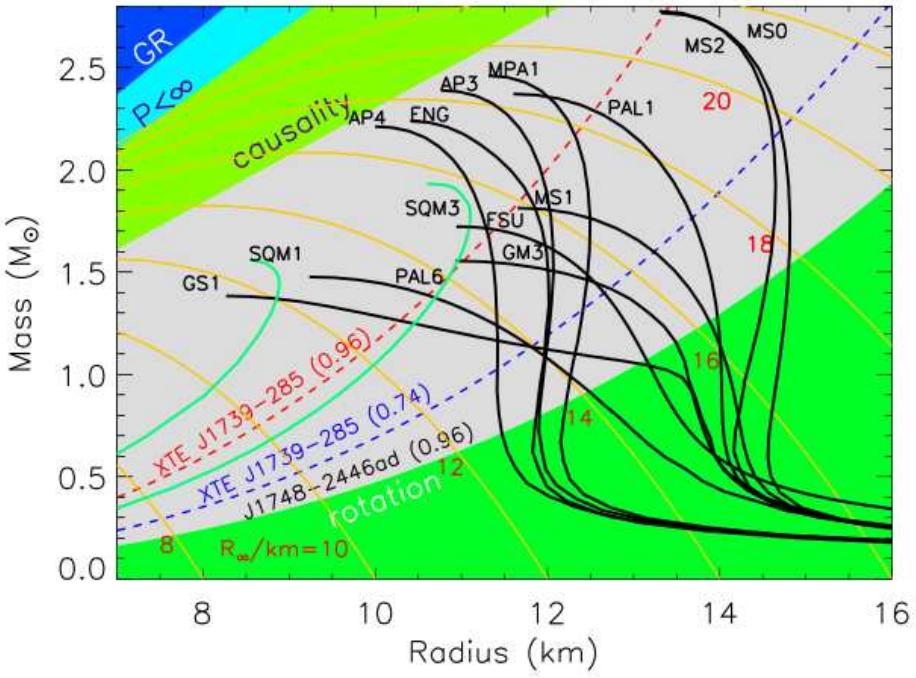

Figure 1.1: Mass and radius relation of cold neutron stars [19]. Each nuclear force model shows different mass-radius relation of neutron stars.

1.1 shows the mass-radius relation of cold neutron stars using various nuclear force models.

[†] $\rho_0 \simeq 0.16\text{fm}^{-3}$. ρ_0 denotes nuclear saturation density which is central density of heavy nuclei. But, in general, it is a nuclear parameter to be determined from standard nuclear matter properties.

Since the mass of neutron star is dominated by its core and the density of the core is much beyond the nuclear saturation density, the nuclear force models should be investigated more than the current level of understanding.

In contrast to neutron stars, supernovae explosions and neutron star mergers result in extremely high temperature. Thus, we need to know thermodynamic properties of nuclear matter for a wide range of densities ($10^{-9} \sim 1.6/\mathrm{fm}^3$) , temperature ($0 \sim 30$ MeV), and proton compositions ($0 \sim 0.56$). This thesis concerns nuclear physics under such extreme conditions, which are far beyond those achievable by nuclear physics experiments on earth. Hence, a theoretical extrapolation is needed for high density, high temperature, and low proton fraction. For zero temperature, the extrapolation of nuclear properties at high density density ($\lesssim 10\rho_0$) can be checked by the mass-radius relation of neutron stars [53]. Unfortunately, the extrapolation to high temperature cannot be checked with anything from experiment or astrophysical observations at this time.

The nuclear thermodynamic information is called 'Nuclear Equation Of State' (EOS) and provided as a tabulated form because of memory constraints. The table should contain free energy density, pressure, entropy as a function of baryon number density, proton fraction, and temperature.

For the simulations of supernovae explosions, only a few EOS tables available now. The most famous one is Lattimer & Swesty [22] (LS) EOS in which they combined non-relativistic potential model with liquid droplet approach. In their EOS they considered phase transitions from three dimensional nuclei to three dimensional bubble. It is difficult in their code to arbitrarily vary nuclear parameters.

H. Shen et al. [59] (STOS) built a table using relativistic mean field model (RMF) and Thomas Fermi approximation. To perform the Thomas Fermi approximation, they employed the parametrized density profile method, in which density profile follows a mathematical polynomial (see chapter 5) so to avoid the numerical difficulty of differential equations. A new version [60] is available now and it contains hyperon interactions.

G. Shen et al. [61] (SHT) provided a few version of tables using RMF parameter sets. They employed the Hartree approximation to find the nuclear density profile. It is difficult and very time consuming to develop another table using their code. Table 1.1 show the range of

Table 1.1: Range of Tables

	LS 220	STOS	SHT
$\rho(\mathrm{fm}^{-3})$	$10^{-6} \sim 1$ (121)	$7.58 \times 10^{-11} \sim 6.022$ (110)	$10^{-8} \sim 1.496$ (328)
Y_p	$0.01 \sim 0.5$ (50)	$0 \sim 0.65$ (66)	$0 \sim 0.56$ (57)
T (MeV)	$0.3 \sim 30$ (50)	$0.1 \sim 398.1$ (90)	$0 \sim 75.0$ (109)

the independent variables and the number of grid points (number in the parenthesis). STOS tables deals wide range of densities and temperature. The number of grid points, however, is small so that the interpolations from that table might not be suitable for the simulation, which needs high thermodynamic consistencies. That is, except for the LS EOS, the pressure and entropy densities from STOS and SHT are obtained from the numerical derivatives ($P = -\rho^2 \frac{\Delta F}{\Delta \rho}$, $S = -\frac{\Delta F}{\Delta T}$). But this numerical formalism might not give enough accuracy for

the thermodynamic identity, $P = \mu_n \rho_n + \mu_p \rho_p - F$ if the grid spacing is relatively large. On the other hand, the LS EOS, which used the liquid droplet approach, provides analytic solutions for thermodynamic variables. The liquid droplet approach enables us to get algebraic solutions for all thermodynamic derivatives. All three approaches used Wigner-Seitz cell method in which one heavy nucleus presents at the center of the cell and electrons, nucleons, and alpha particle exist around the heavy nucleus.
Recently, researchers are trying to build EOS using multi-component nuclei. That is, for given independent variables (ρ, Y_p, T), several types of nuclei are assumed present. Since the electron capture or neutrino weak process are depends on average mass number ($\langle A \rangle$), it is assumed that this multi-component nuclei method would give better EOS than the single heavy nucleus method. Hempel et al. [63, 64] used relativistic mean field models (TM1, TMA, FSU Gold) and nuclear statistical equilibrium method to add the alpha, deutron, and triton. Blinnikov et al. [65] used Saha equation to find the fraction of multi-component nuclei and nuclear mass formula. Furusawa et al. [66] also used Saha equation and relativistic mean filed model. They also considered phase transition using geometric function. Except for Hempel et al., these EOS tables are under construction. Hempel et al. EOS provides the fraction of alpha, deutron, and triton fraction ; however, their fraction are so small that their presence does not effect $\langle A \rangle$ very much. Furthermore, even though the idea of multi-component nuclei may provide better information for weak interaction, their choice of nuclear force model might not satisfy observations of the mass-radius relation of neutron stars. The recent discovery of a $1.97 M_\odot$ neutron star (PSR J16142230) and the Steiner et al.

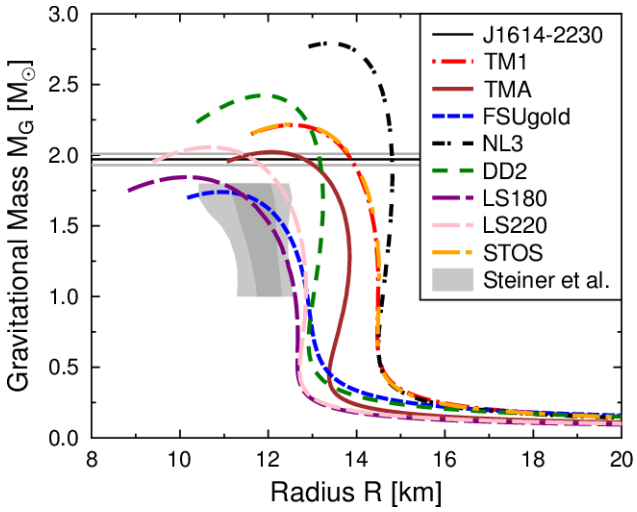

Figure 1.2: Mass and radius relation of cold neutron stars in EOS table. [19]. Only LS220 can satisfy $1.97 M_\odot$ neutron star and the mass-radius criteria.

[53] mass-radius criteria exclude most of the tabulated EOSs. Fig. 1.2 shows the mass-radius relation in which we can find from EOS table. Since the Shen et al. use TM1 parameter, they gives the same mass-radius relation. In general, RMFs give larger radii for given neutron star's mass than the non-relativistic potential models. FSU Gold was invented to reduce the radius for a given mass of neutron star, but it cannot reproduce $1.97 M_\odot$ neutron star. As

shown in Fig. 1.2, LS220 is the only one EOS which satisfy both astrophysical phenomena. Our research starts from inadequacy of current EOS to model allowable variation in uncertain nuclear physics. For this end, we investigate the nuclear force model (Finite Range model) and extract the best parameter set which explains nuclear phenomena such as energies and radii, as well as pure neutron matter and astrophysical data. With the improved nuclear physics model, we build the new EOS tables which can be used for proto-neutron star, supernovae explosions, and binary mergers which involves neutron star.
We extend the Lattimer-Swesty [22] approach to produce user friendly code to incorporate additional physics and adjustable parameters. User will be able to generate tables with only a few cpu hours to compute. This code development (Chapter 6) is contained in the second part of the thesis.
In order to calibrate this liquid droplet formalism, we employ the FRTF model which permits the computation of nuclei immersed in dense matter. This is a more sophisticated approach but still too computationally intensive to generate a complete table. In addition, it, as well as the tables of H.Shen and G.Shen, predicts complex behaviors of matter near the transition between nuclei and uniform matter. This complex behavior results from very small free energy difference between configurations with different mass numbers. In reality, matter near the transition will be smoothed because of the thermal fluctuation. The liquid droplet approach is more suitable in this region. However, it is necessary to calibrate to liquid droplet model so that it successfully models at low densities where laboratory data is available. Another great advantage of making tables using the liquid droplet approach is that it allows the analytic prediction of thermodynamically consistent derivatives. The table would have the wide range of variables such as $\rho : 10^{-10} \sim 1.6$ fm^{-3}, $T : 0 \sim 60$MeV, $Y_p : 0 \sim 0.6$ with more grid points than other tables.

1.1 Organization of Chapters

This work focuses on developing a Finite Range force model and its application to neutron star and making nuclear equation of state (EOS) table. Chapter 2 explains the Finite Range Thomas Fermi model of Yukawa type using a truncated model. Chapter 3 improves the truncated model in Chapter 2. Chapter 4 investigates another type of Finite Range model - the Gaussian type. Chapter 5 illustrate nuclear physics and neutron stars. Finally, Chapter 6 is devoted to making nuclear EOS table. The appendix describes some numerical approximations that we developed.

Chapter 2

The Finite-Range Force Model

† Nuclear physics plays an important role in the understanding of astrophysical phenomena such as neutron stars and supernovae explosions. As described in the introduction, it is really important to choose the good nuclear force model to make E.O.S. tables. There are a lot of kind of nuclear force models, and different types of nuclear physics model can describe the same or different nuclear phenomena. However, the number of models can be used to make E.O.S. table is limited. We explain some of nuclear force models which is related with making E.O.S. table briefly. Our finite-range force model will then be described after the brief explanation.

2.1 Schematic Nuclear force model

Near the nuclear saturation density at small temperatures, the energy density of the uniform nuclear matter can be approximated by [56],

$$\mathcal{E}(\rho,T,x)=\rho\left[-B+\frac{K}{18}\left(1-\frac{\rho}{\rho_o}\right)+S_v\frac{\rho}{\rho_o}(1-2x)^2+a\left(\frac{\rho_o}{\rho}\right)^{2/3}T^2\right] \tag{2.1}$$

where $B\simeq -16$ MeV is the binding energy per baryon, x is the proton fraction, S_v is the symmetry energy, $K(\simeq 230\text{MeV})$ is the nuclear incompressibility, and $a(\simeq 1/15\text{MeV}^{-1})$ is the nuclear level density parameter. Mathematically, this is just a Taylor expansion for ρ, x, and T at $\rho=\rho_o$, $x=1/2$, and $T=0$ MeV.
From thermodynamic derivatives, we can find the pressure, chemical potentials, and entropy

†This chapter is based on Y. Lim and J.M. Lattimer's work. This part will be submitted to the journal Nuclear Physics A.

density:

$$
\begin{aligned}
p &= \frac{\rho^2}{\rho_o}\left[\frac{K}{9}\left(\frac{\rho}{\rho_o}-1\right)+S_v(1-2x)^2\right]+\frac{2a}{3}\rho\left(\frac{\rho_o}{\rho}\right)^{2/3}T^2\,,\\
\mu_n &= -B+\frac{K}{18}\left(1-\frac{\rho}{\rho_o}\right)+2S_v\frac{\rho}{\rho_o}(1-2x)-\frac{a}{3}\left(\frac{\rho_o}{\rho}\right)^{2/3}T^2\,,\\
\hat{\mu} &= 4S_v\frac{\rho}{\rho_o}(1-2x)\,,\\
S &= 2a\rho\left(\frac{\rho_o}{\rho}\right)^{2/3}T\,.
\end{aligned}
\tag{2.2}
$$

These schematic model quantities give reasonable features of nuclear matter, such as the pressure vanishes both at ρ_o and zero density, and becomes negative between them. The proton and neutron chemical potentials approach negative infinity in the limit of low density. This schematic model can be used for a test problem to generate coexistence curve of dense and dilute matter and to find the critical temperature of coexistence. This model gives qualitative numbers so we can estimate the range of validity of realistic models.

2.2 Realistic nuclear force model

Even though the schematic nuclear model can give a good estimation of nuclear matter, it can not be used in the low density ($\rho < 0.01\text{fm}^{-3}$) and high temperature ($T > 5$ MeV) region. Instead we need to rely on more sophisticated models which explain both the high and low density regions, namely the widely used non-relativistic potential and relativistic mean field models of the nuclear force.

As pointed out in Steiner et al. [32], the total Hamiltonian density is the sum of the kinetic energy density and local density dependent interaction energy density. These local properties simplify the numerical calculation of nuclei and nuclear matter since we can apply the variational principle without any mathematical or numerical difficulties.

Both potential and mean field models explain the properties of a single nucleus very well. However, we need to be careful when applying those models in high density regions (see section 6.3).

2.2.1 Non-Relativistic Potential Model

The non-relativistic potential model, which is often called the 'Skyrme force model', is a density and momentum density functional in a mathematical sense. In this model, the Hamiltonian density is composed of bulk, gradient, Coulomb energy, and spin-orbit coupling components,

$$\mathcal{H} = \mathcal{H}_B + \mathcal{H}_g + \mathcal{H}_C + \mathcal{H}_J\,. \tag{2.3}$$

The bulk part is divided by kinetic energy density, two-body interaction, and many body interactions of nucleons [32],

$$\begin{aligned}\mathcal{H}_B =&\frac{\hbar^2}{2m_n}\tau_n + \frac{\hbar^2}{2m_p}\tau_p \\ &+ \rho(\tau_n+\tau_p)\left[\frac{t_1}{4}\Big(1+\frac{x_1}{2}\Big) + \frac{t_2}{4}\Big(1+\frac{x_2}{2}\Big)\right] \\ &+ (\tau_n\rho_n+\tau_p\rho_p)\left[\frac{t_2}{4}\Big(\frac{1}{2}+x_2\Big) - \frac{t_1}{4}\Big(\frac{1}{2}+x_1\Big)\right] \\ &+ \frac{t_0}{2}\left[\Big(1+\frac{x_0}{2}\Big)\rho^2 - \Big(\frac{1}{2}+x_0\Big)(\rho_n^2+\rho_p^2)\right] \\ &+ \frac{t_3}{12}\left[\Big(1+\frac{x_3}{2}\Big)\rho^2 - \Big(\frac{1}{2}+x_3\Big)(\rho_n^2+\rho_p^2)\right]\rho^\epsilon\,,\end{aligned} \tag{2.4}$$

where $x_0, \ldots, t_3$, and ϵ are parameters specifying the interaction strengths, which are determined from nuclear data fitting.
The density gradient term, which is responsible for the surface tension of a single nucleus, is given by [32]

$$\mathcal{H}_g = \frac{1}{2}\Big[Q_{nn}(\nabla\rho_n)^2 + 2Q_{np}\nabla\rho_n\nabla\rho_p + Q_{pp}(\nabla\rho_p)^2\Big]\,, \tag{2.5}$$

where the Q parameters are given by

$$\begin{aligned}Q_{nn} = Q_{pp} &= \frac{3}{16}\Big[t_1(1-x_1) - t_2(1+x_2)\Big]\,, \\ Q_{np} = Q_{pn} &= \frac{1}{8}\Big[3t_1\left(1+\frac{x_1}{2}\right) - t_2\left(1+\frac{x_2}{2}\right)\Big]\,.\end{aligned} \tag{2.6}$$

The Coulomb energy interaction is

$$\mathcal{H}_C(\mathbf{r}) = \frac{e^2\rho_p(\mathbf{r})}{2}\int d^3r'\frac{\rho_p(\mathbf{r}')}{|\mathbf{r}-\mathbf{r}'|} - \frac{3e^2}{4}\left(\frac{3}{\pi}\right)^{1/3}\rho_p(\mathbf{r}')^{4/3}\,, \tag{2.7}$$

where the first term is a classical Coulomb energy interaction, and the second term is an exchange Coulomb interaction.
The spin-orbit interaction is given by

$$\begin{aligned}\mathcal{H}_J =& -\frac{W_0}{2}(\rho_n\nabla\cdot\mathbf{J}_n + \rho_p\nabla\cdot\mathbf{J}_p + \rho\nabla\cdot\mathbf{J}) \\ &+ \frac{t_1}{16}(\mathbf{J}_n^2 + \mathbf{J}_p^2 - x_1\mathbf{J}^2) - \frac{t_2}{16}(\mathbf{J}_n^2 + \mathbf{J}_p^2 + x_2\mathbf{J}^2)\,,\end{aligned} \tag{2.8}$$

where $\mathbf{J}_n = \sum_{n,i}\psi_i^\dagger\sigma\times\nabla\psi_i$, $\mathbf{J} = \mathbf{J}_n + \mathbf{J}_p$. There are more than 100 parameter set in this Skyrme force model. Combined with the Hartree-Fock[†] approximation, this Skyrme force

[†]In the Hartree-Fock or Hartree Approximation, the trial wave function is assumed as initial guess and keep iterating until $E_{N+1} - E_N < \delta$, where δ is a tolerance for energy difference. This is a mathematical

nuclear energy density functional is quite successful in demonstrating the binding energy, root mean square radius, and charged radius of a single nucleus. This force model, however, should be chosen carefully when studying high density ($\gtrsim \rho_0$) region (see section 6.3).

2.2.2 Relativistic Mean Field Model

At high density, for example $n = \rho_0$, the Fermi momentum at zero temperature is given as

$$p_f c = \hbar c (3\pi^2 \rho_0)^{1/3} \sim 330\text{MeV}\,. \tag{2.9}$$

Therefore, the expansion of the total energy $\sqrt{m^2c^4 + p^2c^2}$ to $mc^2 + \frac{p^2}{2m}$ is not valid anymore, and the relativistic effects need to be considered.
The relativistic mean field model explains the origin of nuclear force from ρ, ω, and σ meson exchanges. In the mean field model, the Lagrangian formalism satisfies relativity and causality, and is given by [32]

$$\begin{aligned}\mathcal{L} =& \bar{\Psi}\left[i\partial\!\!\!/ - g_\omega \boldsymbol{\omega\!\!\!/} \cdot \boldsymbol{\tau} - M + g_\sigma \sigma - \frac{1}{2}(1+\tau)A\!\!\!/\right]\Psi + \frac{1}{2}(\partial_\mu \sigma)^2 \\ & - V(\sigma) - \frac{1}{4} f_{\mu\nu} f^{\mu\nu} + \frac{1}{2} m_\omega^2 \omega^\mu \omega_\mu - \frac{1}{4}\boldsymbol{B}_{\mu\nu}\boldsymbol{B}^{\mu\nu} + \frac{1}{2} m_\rho^2 \boldsymbol{\rho}^\mu \boldsymbol{\rho}_\mu - \frac{1}{4} F_{\mu\nu} F^{\mu\nu} \\ & + \frac{\zeta}{24} g_\omega^4 (\omega^\mu \omega_\mu)^2 + \frac{\xi}{24} g_\rho^4 (\boldsymbol{\rho}^\mu \cdot \boldsymbol{\rho}_\mu)^2 + g_\rho^2 f(\sigma, \omega_\mu \omega^\mu) \boldsymbol{\rho}^\mu \cdot \boldsymbol{\rho}_\mu\end{aligned} \tag{2.10}$$

where $V(\sigma)$ and $f(\sigma, \omega_\mu \omega^\mu)$ are

$$\begin{aligned} V(\sigma) =& \frac{1}{2} m_\sigma \sigma^2 + \frac{\kappa}{6}(g_\sigma \sigma)^3 + \frac{\lambda}{6}(g_\sigma \sigma)^4\,, \\ f(\sigma, \omega_\mu \omega^\mu) =& \sum_{i=1}^{6} a_i \sigma^i + \sum_{j=1}^{3} (\omega_\mu \omega^\mu)^j\,. \end{aligned} \tag{2.11}$$

Here, A_μ is photon field, $f_{\mu\nu} = \partial_\mu \omega_\nu - \partial_\nu \omega_\mu$, $\boldsymbol{B}_{\mu\nu} = \partial_\mu \boldsymbol{\rho}_\nu - \partial_\nu \boldsymbol{\rho}_\mu$, and $F_{\mu\nu} = \partial_\mu A_\nu - \partial_\nu A_\mu$. Like a non-relativistic potential model, the RMF is useful to study single nucleus' properties. It seems that the RMF should be used to study nuclear physics at high density region since it is relativistic and the hyperon's appearance can be controlled by coupling constant. However, it does not show the proper mass and radius relation of neutron stars. Therefore, we are not focused on this RMF formalism anymore.

2.3 Finite-Range Model and its Extension to Finite Temperature

The interaction between nucleons is short ranged, on the order of $1 \sim 2$ fm. To take into account this short ranged interaction, we need to add the density dependent interaction form. The π meson exchange model was successful in accounting for the nuclear interactions, and

analogue of 'Cauchy criterion'

we can get the $\frac{e^{-r/r_0}}{r}$ interaction form from the π exchange model. This idea was enlarged by several authors [24, 30]. We re-examine this idea and add new interaction terms to reflect the recent nuclear experiments and to explain the mass and radius of cold neutron stars.

2.3.1 The Interaction Energy

We begin with the truncated version of the Myers & Swiatecki [26] finite-range model, which is an extended version of the Seyler & Blanchard [30, 31] finite-range model. We will generalize this force to finite temperatures. Initially, we ignore the Coulomb contributions to the total energy. The symmetric matter saturation density is ρ_o, and the zero-temperature Fermi momentum P_o is $(P_o/\hbar)^3 = 3\pi^2\rho_o/2$. The zero-temperature kinetic energy is $T_o = P_o^2/2m_b$ where m_b is the baryon mass. We will assume the interaction energy is

$$W = -\frac{1}{h^3}\int d^3r_1 \int d^3r_2 f(r_{12}/a) \sum_t \left[\int C_L f_{t1} f_{t2} d^3p_{t1} d^3p_{t2} + \int C_U f_{t1} f_{t'2} d^3p_{t1} d^3p_{t'2} \right] \quad (2.12)$$

where f_{ti} is the Fermi occupation function for particle ti [†]. The position index $i = 1$ or 2 and the isospin index $t = n$ or p. The notation is such that if $t = n$ then $t' = p$ and vice versa. p_{ti} is the momentum of the nucleon at position i of species t. The finite-range function is taken to be Yukawa-like,

$$f(r_{12}/a) = \frac{1}{4\pi r_{12} a^2} e^{-r_{12}/a}, \qquad r_{12} = |\boldsymbol{r_1} - \boldsymbol{r_2}|. \quad (2.13)$$

The finite-range function f is normalized so that $\int d^3r_2 f(r_{12}/a) = 1$ for all r_1. The range parameter a will be determined by fitting matter surface profiles or surface energies to laboratory values. The quantities $C_{L,U}$ are momentum- and density-dependent interaction functionals for like (L) and unlike (U) pairs of particles. Myers & Swiatecki chose them, with some changes in notation, to be

$$C_{L,U}(p_1, p_2, \bar{\rho}) = \frac{h^3}{4} T_o \rho_o \left(\frac{3}{4\pi P_o^3}\right)^2 \left[\alpha_{L,U} - \beta_{L,U} \left(\frac{p_{12}}{P_o}\right)^2 - \sigma_{L,U} \left(\frac{2\bar{\rho}}{\rho_o}\right)^{2/3} \right] \quad (2.14)$$

where $\alpha_L, \alpha_U, \beta_L, \beta_U, \sigma_L, \sigma_U$ are constants. These constants are to be determined by fitting saturation properties of cold nuclear matter and other considerations. In Eq. (2.14) , $p_{12} = |\boldsymbol{p_1} - \boldsymbol{p_2}|$. The quantity $\bar{\rho}(r)$ is the mean density, which is chosen to be

$$\bar{\rho}^{2/3} = (\rho_1^{2/3} + \rho_2^{2/3})/2 \quad (2.15)$$

where ρ_1 and ρ_2 are the baryon densities at positions r_1 and r_2, respectively.

[†] t indicates proton or neutron and i represents position of the particle.

2.3.2 Thermodynamic Quantities

The total energy is the sum of the free particle kinetic energy and the interaction energy, which can be expressed as

$$\begin{aligned} E = & \int d^3r_1 \frac{\hbar^2}{2m_b}(\tau_n + \tau_p) - \frac{T_o\rho_o}{4}\int d^3r_1 \int d^3r_2 f(r_{12}/a)\times \\ & \sum_t \Big[\alpha_L I_1(\rho_{t1},\rho_{t2}) - \beta_L I_2(\rho_{t1},\tau_{t1},\rho_{t2},\tau_{t2}) - \sigma_L I_4(\rho_{t1},\rho_{t2}) + \\ & \alpha_U I_1(\rho_{t1},\rho_{t'2}) - \beta_U I_2(\rho_{t1},\tau_{t1},\rho_{t'2},\tau_{t'2}) - \sigma_U I_4(\rho_{t1},\rho_{t'2})\Big], \end{aligned} \tag{2.16}$$

where the double momentum integrals I_1, I_2 and I_4 are analytic and are expressed as

$$\begin{aligned} I_1(\rho_1,\rho_2) =& \left(\frac{3}{4\pi P_o^3}\right)^2 \int_0^\infty f_1 d^3p_1 \int_0^\infty f_2 d^3p_2 = \left(\frac{2}{\rho_o}\right)^2 \rho_1\rho_2, \\ I_2(\rho_1,\tau_1,\rho_2,\tau_2) =& \left(\frac{3}{4\pi P_o^3}\right)^2 \int_0^\infty f_1 d^3p_1 \int_0^\infty f_2 d^3p_2 \left(\frac{p_{12}}{P_o}\right)^2 \\ =& \left(\frac{2\hbar}{\rho_o P_o}\right)^2 (\tau_1\rho_2 + \rho_1\tau_2), \\ I_4(\rho_1,\rho_2) =& \frac{1}{2}\left(\frac{3}{4\pi P_o^3}\right)^2 \left(\frac{2}{\rho_o}\right)^{2/3} \left(\rho_1^{2/3} + \rho_2^{2/3}\right) \int_0^\infty f_1 d^3p_1 \int_0^\infty f_2 d^3p_2 \\ =& \frac{1}{2}\left(\frac{2}{\rho_o}\right)^{8/3} \rho_1\rho_2 \left(\rho_1^{2/3} + \rho_2^{2/3}\right). \end{aligned} \tag{2.17}$$

In the Thomas-Fermi approximation, the number and kinetic densities have their usual forms in finite temperature matter:

$$\rho_t = \frac{1}{4\pi^3\hbar^3}\int_0^\infty f_t d^3p; \qquad \tau_t = \frac{1}{4\pi^3\hbar^5}\int_0^\infty f_t p^2 d^3p, \tag{2.18}$$

where the Fermi occupation function is

$$f_t = \left[1 + \exp\left(\frac{\epsilon_t - \mu_t}{T}\right)\right]^{-1}. \tag{2.19}$$

The single particle energies ϵ_t, which are functions of the momentum p_t and the nucleon densities, are evaluated below. The nucleon chemical potentials are μ_t.

The total energy, beginning with Eq. (2.38) and using the results in Eqs. (2.17) and

(2.18), becomes

$$E = \int d^3r_1 \sum_t \Bigg\{ \frac{\hbar^2}{2m_b}\tau_t - \frac{T_o}{\rho_o}\int d^3r_2 f(r_{12}/a)\times \\ \Bigg[\alpha_L\rho_{t1}\rho_{t2} + \alpha_U\rho_{t1}\rho_{t'2} - \beta'_L(\rho_{t1}\tau_{t2}+\rho_{t2}\tau_{t1}) - \beta'_U(\rho_{t1}\tau_{t'2}+\rho_{t'2}\tau_{t1}) \\ - \sigma'_L\rho_{t1}\rho_{t2}\Big(\rho_{t1}^{2/3}+\rho_{t2}^{2/3}\Big) - \sigma'_U\rho_{t1}\rho_{t'2}\Big(\rho_{t1}^{2/3}+\rho_{t'2}^{2/3}\Big)\Bigg]\Bigg\} \tag{2.20}$$

where we introduce the new constants

$$\beta'_{L,U} = \beta_{L,U}\left(\frac{2}{3\pi^2\rho_o}\right)^{2/3}, \qquad \sigma'_{L,U} = \frac{\sigma_{L,U}}{2}\left(\frac{2}{\rho_o}\right)^{2/3}.$$

The energy density is then the integrand of the d^3r_1 integration in Eq. (2.20):

$$\mathcal{E}(r) = \sum_t \Bigg\{ \frac{\hbar^2}{2m_b}\tau_t - \frac{T_o}{\rho_o}\Bigg[\rho_t(\alpha_L\tilde{\rho}_t + \alpha_U\tilde{\rho}_{t'}) - \beta'_L(\tau_t\tilde{\rho}_t + \rho_t\tilde{\tau}_t) \\ - \beta'_U(\rho_t\tilde{\tau}_{t'} + \tau_t\tilde{\rho}_{t'}) - \sigma'_L\rho_t\Big(\tilde{\rho}_t\rho_t^{2/3} + \widetilde{\rho_t^{5/3}}\Big) - \sigma'_U\rho_t\Big(\rho_t^{2/3}\tilde{\rho}_{t'} + \widetilde{\rho_{t'}^{5/3}}\Big)\Bigg]\Bigg\}, \tag{2.21}$$

where we define the finite-range integral as

$$\widetilde{g(r)} \equiv \int d^3r' f(|r-r'|/a)g(r') \tag{2.22}$$

where the notation changes from $r_1 \to r$ and $r_2 \to r'$. Using the definitions for the effective masses m_t^* and the potential V_t in

$$\delta E = \int d^3r \delta\mathcal{E} = \sum_t \int d^3r \left[V_t\delta\rho_t + \frac{\hbar^2}{2m_t^*}\delta\tau_t \right], \tag{2.23}$$

we find, after noting that r and r' can be reversed within double integrals,

$$\begin{aligned} \frac{\hbar^2}{2m_t^*} =& \frac{\hbar^2}{2m_b} + \frac{2T_o}{\rho_o}(\beta'_L\tilde{\rho}_t + \beta'_U\tilde{\rho}_{t'}), \\ V_t =& -\frac{2T_o}{\rho_o}\Bigg[\alpha_L\tilde{\rho}_t + \alpha_U\tilde{\rho}_{t'} - \beta'_L\tilde{\tau}_t - \beta'_U\tilde{\tau}_{t'} \\ & - \sigma'_L\left(\frac{5}{3}\rho_t^{2/3}\tilde{\rho}_t + \widetilde{\rho_t^{5/3}}\right) - \sigma'_U\left(\frac{5}{3}\rho_t^{2/3}\tilde{\rho}_{t'} + \widetilde{\rho_{t'}^{5/3}}\right)\Bigg]. \end{aligned} \tag{2.24}$$

In addition, we note that at zero temperature, the total potential felt by a neutron at the

point r and with momentum p is

$$U_n(r,p) = V_n(r) + \frac{2T_o}{\rho_o}\Big[\beta_L\tilde{\rho}_n + \beta_U\tilde{\rho}_p\Big]\left(\frac{p}{P_o}\right)^2. \tag{2.25}$$

With these explicit relations, one can now employ the methodology of Lattimer & Ravenhall [21] to determine thermodynamic quantities. The single-particle energy is

$$\epsilon_t = \frac{p^2}{2m_t^*} + V_t. \tag{2.26}$$

It follows from Eq. (2.18) that the densities and kinetic densities are

$$\rho_t = \frac{1}{2\pi^2}\left(\frac{2m_t^*T}{\hbar^2}\right)^{3/2}F_{1/2}(\Psi_t), \quad \tau_t = \frac{1}{2\pi^2}\left(\frac{2m_t^*T}{\hbar^2}\right)^{5/2}F_{3/2}(\Psi_t), \tag{2.27}$$

where $\Psi_t = (\mu_t - V_t)/T$ is the degeneracy parameter. The inversion of the first of these yields the chemical potential:

$$\mu_t = V_t + TF_{1/2}^{-1}\left[2\pi^2\rho_t\left(\frac{\hbar^2}{2m_t^*T}\right)^{3/2}\right]. \tag{2.28}$$

The entropy density S_t is given by Landau's quasi-particle formula [22]

$$S_t = -\frac{2}{h^3}\int d^3p\Big[f_t\ln f_t + (1-f_t)\ln(1-f_t)\Big] = \frac{5\hbar^2}{6m_t^*T}\tau_t - \frac{\mu_t - V_t}{T}\rho_t. \tag{2.29}$$

The pressure follows from the thermodynamic identity

$$\begin{aligned} p &= \sum_t(\mu_t\rho_t + TS_t) - \mathcal{E} \\ &= \sum_t\left[\frac{\hbar^2}{3m_b}\tau_t - \frac{T_o}{\rho_o}\left\{\rho_t(\alpha_L\tilde{\rho}_t + \alpha_U\tilde{\rho}_{t'}) - \beta_L'\left(\rho_t\tilde{\tau}_t + \frac{7}{3}\tilde{\rho}_t\tau_t\right)\right.\right. \\ &\quad \left.\left. - \beta_U'\left(\rho_t\tilde{\tau}_{t'} + \frac{7}{3}\tilde{\rho}_{t'}\tau_t\right) - \sigma_L'\rho_t\left(\frac{7}{3}\rho_t^{2/3}\tilde{\rho}_t + \widetilde{\rho_t^{5/3}}\right) - \sigma_U'\rho_t\left(\frac{7}{3}\rho_t^{2/3}\tilde{\rho}_{t'} + \widetilde{\rho_{t'}^{5/3}}\right)\right\}\right]. \end{aligned} \tag{2.30}$$

The pressure relation can be simplified, upon eliminating the terms involving $\widetilde{\rho_t^{5/3}}$, to

$$p = \sum_t\left[\frac{\hbar^2\tau_t}{3m_t^*} + \frac{\rho_t}{2}(\mu_t - T\Psi_t) + \frac{T_o}{\rho_o}\left([\beta_L'\tilde{\rho}_t + \beta_U'\tilde{\rho}_{t'}]\tau_t + \frac{2}{3}\rho_t^{5/3}[\sigma_L'\tilde{\rho}_t + \sigma_U'\tilde{\rho}_{t'}]\right)\right]. \tag{2.31}$$

2.3.3 Properties of Uniform Matter

For the case of uniform matter, $\tilde{g} = g$, the energy density becomes

$$\begin{aligned}\mathcal{E} =& \sum_t \left\{ \frac{\hbar^2}{2m_t^*}\tau_t - \frac{T_o}{\rho_o}\rho_t\Big(\alpha_L\rho_t + \alpha_U\rho_{t'} - 2\sigma'_L\rho_t^{5/3} - 2\sigma'_U\rho_{t'}^{5/3}\Big)\right\} \\ =& \sum_t \left\{ \frac{\hbar^2}{2m_b}\tau_t - \frac{T_o}{\rho_o}\rho_t\Big[\alpha_L\rho_t + \alpha_U\rho_{t'} - 2\Big(\beta'_L\tau_t + \beta'_U\tau_{t'} + \rho_t^{2/3}[\sigma'_L\rho_t + \sigma'_U\rho_{t'}]\Big)\Big]\right\}.\end{aligned} \tag{2.32}$$

Here, the effective masses are

$$\frac{\hbar^2}{2m_t^*} = \frac{\hbar^2}{2m_b} + \frac{2T_o}{\rho_o}(\beta'_L\rho_t + \beta'_U\rho_{t'}). \tag{2.33}$$

Note that the energy density reduces to a Skyrme-like model. The potentials become

$$V_t = -\frac{2T_o}{\rho_o}\left[\alpha_L\rho_t + \alpha_U\rho_{t'} - \beta'_L\tau_t - \beta'_U\tau_{t'} - \frac{8}{3}\sigma'_L\rho_t^{5/3} - \sigma'_U\rho_{t'}(\frac{5}{3}\rho_t^{2/3} + \rho_{t'}^{2/3})\right] \tag{2.34}$$

The pressure can then be written as

$$\begin{aligned}p =& \sum_t \left\{ \frac{\hbar^2\tau_t}{3m_t^*} - \frac{T_o}{\rho_o}\rho_t\left[\alpha_L\rho_t + \alpha_U\rho_{t'} - 2(\beta'_L\tau_t + \beta'_U\tau_{t'}) - \frac{10}{3}\rho_t^{2/3}\big(\sigma'_L\rho_t + \sigma'_U\rho_{t'}\big)\right]\right\} \\ =& \sum_t \left\{ \frac{\hbar^2\tau_t}{3m_b} - \frac{T_o}{\rho_o}\rho_t\left[\alpha_L\rho_t + \alpha_U\rho_{t'} - \frac{10}{3}\Big(\beta'_L\tau_t + \beta'_U\tau_{t'} + \rho_t^{2/3}\big[\sigma'_L\rho_t + \sigma'_U\rho_{t'}\big]\Big)\right]\right\}.\end{aligned} \tag{2.35}$$

The chemical potentials and entropy density are given by Eqs. (2.28) and (2.29), respectively.

2.3.4 The Zero-Temperature Limit

The zero-temperature limit is needed in order to establish the parameters of the force from experimental constraints. In the zero-temperature limit, one finds from limiting expressions for the Fermi integrals:

$$\begin{aligned}\rho_t =& \frac{1}{\pi^2}\left(\frac{2m_t^*(\mu_t - V_t)}{\hbar^2}\right)^{3/2}, \\ \tau_t =& \frac{1}{\pi^2}\left(\frac{2m_t^*(\mu_t - V_t)}{\hbar^2}\right)^{5/2} = \frac{3}{5}(3\pi^2)^{2/3}\rho_t^{5/3}.\end{aligned} \tag{2.36}$$

Furthermore, for the case of symmetric nuclear matter ($\rho_n = \rho_p = \rho_o/2$), one obtains

$$\frac{\hbar^2}{2m_b}\tau_n\Big|_{\rho=\rho_o,x=1/2} = \frac{\hbar^2}{2m_b}\tau_p\Big|_{\rho=\rho_o,x=1/2} = \frac{3}{10}T_o\rho_o. \tag{2.37}$$

Thus, in the case of zero temperature, the energy density is

$$\begin{aligned}\mathcal{E} =&T_o\sum_t \rho_t\Bigg\{\frac{3}{5}\left(\frac{2\rho_t}{\rho_o}\right)^{2/3} - \frac{1}{\rho_o}\Bigg[\alpha_L\tilde{\rho}_t + \alpha_U\tilde{\rho}_{t'} - \\ &\frac{1}{2}\left(\frac{2}{\rho_o}\right)^{2/3}\left(\beta''_L\left[\rho_t^{2/3}\tilde{\rho}_t + \widetilde{\rho_t^{5/3}}\right] + \beta''_U\left[\rho_t^{2/3}\tilde{\rho}_{t'} + \widetilde{\rho_{t'}^{5/3}}\right]\right)\Bigg]\Bigg\}\end{aligned} \tag{2.38}$$

where

$$\beta''_{(L,U)} = \left(\frac{\rho_o}{2}\right)^{2/3}\left[\frac{6}{5}\left(3\pi^2\right)^{2/3}\beta'_{(L,U)} + 2\sigma'_{(L,U)}\right] = \frac{6}{5}\beta_{(L,U)} + \sigma_{(L,U)}. \tag{2.39}$$

The potentials at zero temperature become

$$V_t = -\frac{2T_o}{\rho_o}\left[\alpha_L\tilde{\rho}_t + \alpha_U\tilde{\rho}_{t'} - \frac{1}{2}\left(\frac{2}{\rho_o}\right)^{2/3}\left(\beta''_L\widetilde{\rho_t^{5/3}} + \beta''_U\widetilde{\rho_{t'}^{5/3}}\right) - \frac{5}{3}\rho_t^{2/3}\left(\sigma'_L\tilde{\rho}_t + \sigma'_U\tilde{\rho}_{t'}\right)\right] \tag{2.40}$$

The expression for the effective mass of Eq. (2.33) is still valid, so the Euler equations at zero temperature, using Eq. (2.36), take the form

$$\begin{aligned}\mu_t =&\frac{\hbar^2}{2m_t^*}\left(3\pi^2\rho_t\right)^{2/3} + V_t = T_o\left(\frac{2\rho_t}{\rho_o}\right)^{2/3} - \frac{2T_o}{\rho_o}\times \\ &\left[\alpha_L\tilde{\rho}_t + \alpha_U\tilde{\rho}_{t'} - \frac{1}{2}\left(\frac{2}{\rho_o}\right)^{2/3}\left[\beta''_L\left(\widetilde{\rho_t^{5/3}} + \frac{5}{3}\rho_t^{2/3}\tilde{\rho}_t\right) + \beta''_U\left(\widetilde{\rho_{t'}^{5/3}} + \frac{5}{3}\rho_t^{2/3}\tilde{\rho}_{t'}\right)\right]\right].\end{aligned} \tag{2.41}$$

The pressure at zero temperature, using the notation $u_t = \rho_t/\rho_o$, becomes

$$\begin{aligned}p =&\rho_o T_o\sum_t u_t\Bigg[\frac{2}{5}2^{2/3}u_t^{2/3} - \alpha_L\tilde{u}_t - \alpha_U\tilde{u}_{t'} \\ &+2^{-1/3}\left[\beta''_L(\widetilde{u_t^{5/3}} + \frac{7}{3}u_t^{2/3}\tilde{u}_t) + \beta''_U(\widetilde{u_{t'}^{5/3}} + \frac{7}{3}u_t^{2/3}\tilde{u}_{t'})\right]\Bigg].\end{aligned} \tag{2.42}$$

Once again eliminating terms involving $\widetilde{\rho_t^{5/3}}$, the pressure relation can be simplified to

$$p = \rho_o\sum_t u_t\left[\frac{\mu_t}{2} + (2u_t)^{2/3}T_o\left(\frac{\beta''_L}{3}\tilde{u}_t + \frac{\beta''_U}{3}\tilde{u}_{t'} - \frac{1}{10}\right)\right]. \tag{2.43}$$

2.3.5 Uniform Matter at Zero Temperature and the Saturation Constraints

Next, we consider uniform matter at zero temperature. Using the notation $u = (\rho_n + \rho_p)/\rho_o$ and $x = \rho_p/(\rho_n + \rho_p)$, the bulk energy density at zero temperature is

$$\mathcal{E} = T_o\rho_o\Big\{\frac{3}{5}2^{2/3}u^{5/3}\Big[(1-x)^{5/3}+x^{5/3}\Big] - u^2\Big(\alpha_L[(1-x)^2+x^2]+2\alpha_U(1-x)x\Big) \\ +2^{2/3}u^{8/3}\Big(\beta''_L\Big[(1-x)^{8/3}+x^{8/3}\Big]+\beta''_U x(1-x)\Big[(1-x)^{2/3}+x^{2/3}\Big]\Big)\Big\}. \tag{2.44}$$

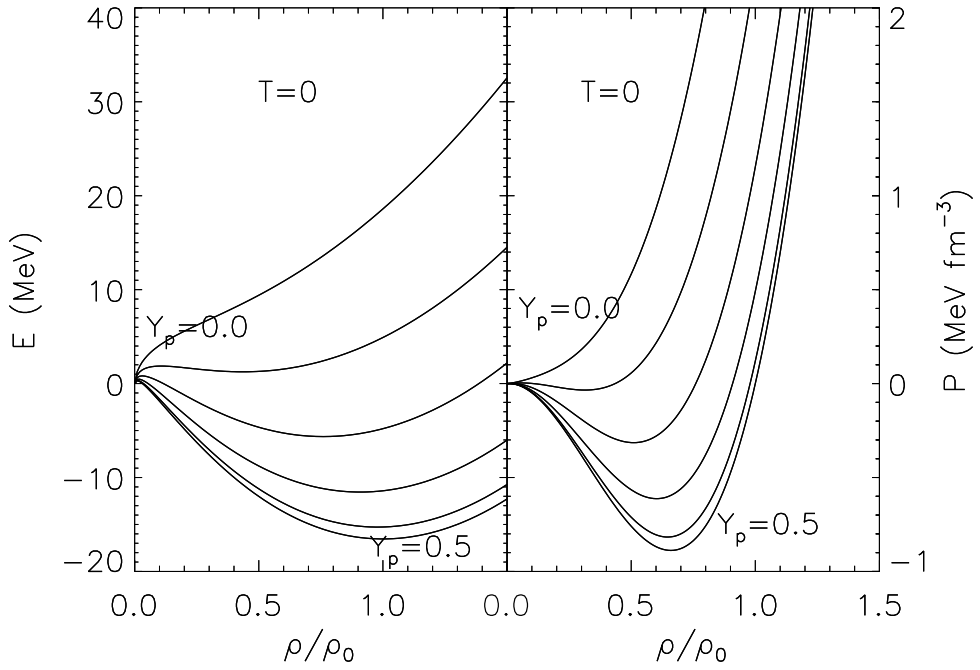

Figure 2.1: The energy per baryon E and pressure p for zero-temperature matter as a function of composition Y_p. The assumed saturation constraints are: $\rho_o = 0.16545$ fm^{-3}, $E_o = -16.533$ MeV, $p_o = 0$, $S_v = 31.63$ MeV and $S'_v = 17.93$ MeV.

Fig. 2.1 shows the energy per nucleon $E = \mathcal{E}/\rho$ and the pressure p of uniform matter as a function of density and composition Y_p for the case of zero-temperature matter. Obviously, there are substantial regions in which the incompressibility, $(\partial P/\partial n)_{T,Y_p}$, is negative and the matter is hydrodynamically unstable. It is straightforward to show that the free energy can be lowered if matter spontaneously divides into two phases of differing densities with the same temperature. For asymmetric matter, each phase has differing compositions as well. These phases are in bulk equilibrium, which is described in the next section.

For standard nuclear matter, $u = 1$ and $x = 1/2$. Letting $\alpha = \alpha_L + \alpha_U$ and $\beta'' = \beta''_L + \beta''_U = (6/5)\beta + \sigma$, using $\beta = \beta_L + \beta_U$ and $\sigma = \sigma_L + \sigma_U$, and defining the binding energy as $B = -\mathcal{E}_o/\rho_o$, one finds the energy per particle to be

$$\frac{\mathcal{E}_o}{\rho_o} = -B = T_o\left[\frac{3}{5} - \frac{\alpha}{2} + \frac{\beta''}{2}\right], \tag{2.45}$$

while the pressure becomes

$$p_o = 0 = \rho_o T_o\left[\frac{2}{5} - \frac{\alpha}{2} + \frac{5}{6}\beta''\right], \tag{2.46}$$

and the incompressibility parameter reduces to

$$K_o = 9\frac{dP}{d\rho}\bigg|_{\rho=\rho_o,x=1/2} = T_o[6 - 9\alpha + 20\beta'']. \tag{2.47}$$

These can be combined as

$$K_o = \frac{9}{5}T_o + 15B \simeq 316 \text{ MeV}, \tag{2.48}$$

and

$$\alpha = \frac{9}{5} + \frac{5B}{T_o} \simeq 3.995, \qquad \beta'' = \frac{3}{5} + \frac{3B}{T_o} \simeq 1.917, \tag{2.49}$$

using $T_o \simeq 37.68$ MeV and $B \simeq 16.54$ MeV. (For the purposes of illustration, we use the parameter set established by Myers & Swiatecki [26].) The bulk symmetry parameter is

$$S_v = \frac{1}{8}\frac{d^2(\mathcal{E}/\rho)}{dx^2}\bigg|_{\rho=\rho_o,x=1/2} = T_o\left[\frac{1}{3} + \frac{\alpha_U - \alpha_L}{2} + \frac{5}{9}(2\beta''_L - \beta''_U)\right]. \tag{2.50}$$

The derivatives of the symmetry energy and the incompressibilities at saturation are

$$S'_v = \frac{\rho_o}{8}\frac{d^3(\mathcal{E}/\rho)}{d\rho dx^2}\bigg|_{\rho=\rho_o,x=1/2} = T_o\left[\frac{2}{9} + \frac{\alpha_U - \alpha_L}{2} + \frac{25}{27}(2\beta''_L - \beta''_U)\right], \tag{2.51}$$

$$\begin{aligned} K'_o =& \rho_o\frac{dK}{d\rho}\bigg|_{\rho=\rho_o,x=1/2} = K_o + 9\rho_o^2\left(\frac{d^3\mathcal{E}}{d\rho^3}\right)_{\rho=\rho_o,x=1/2} = \\ & T_o\left[4 - 9\alpha + \frac{100}{3}\beta''\right] = \frac{39}{5}T_o + 55B \simeq 1204 \text{ MeV}\,. \end{aligned} \tag{2.52}$$

In order to specify given values of S_v and S'_v, one can manipulate Eqs. (2.50) and (2.51):

$$\begin{aligned} \alpha_L =& \frac{7}{5} + \frac{5B + 3S'_v - 5S_v}{2T_o}, \qquad \alpha_U = \frac{2}{5} + \frac{5B + 5S_v - 3S'_v}{2T_o}, \\ \beta''_L =& \frac{3}{10} + \frac{10B + 9S'_v - 9S_v}{10T_o}, \qquad \beta''_U = \frac{3}{10} + \frac{20B + 9S_v - 9S'_v}{10T_o}. \end{aligned} \tag{2.53}$$

For values of $S_v = 31.63$ MeV and $S'_v = 17.93$ MeV established by Myers & Swiatecki for the truncated model, one finds $\alpha_L \simeq 1.112$, $\alpha_U \simeq 2.882$, $\beta''_L \simeq 0.417$, $\beta''_U \simeq 1.505$. Note that for zero temperature uniform matter, $\mathcal{E}, P$ and μ_t depend only on $\alpha_l, \alpha_U, \beta''_L$ and β''_U. To constrain other the parameters one has to consider the properties of non-uniform matter and finite-temperature matter.

The specific heat of degenerate nucleonic matter depends on the nucleon effective masses. The symmetric matter effective mass at saturation density is

$$\frac{\hbar^2}{2m^*} = \frac{\hbar^2}{2m_b} + T_o(\beta'_L + \beta'_U), \qquad \frac{m^*}{m_b} = \frac{1}{1+\beta}. \tag{2.54}$$

A reasonable value for m^*/m_b is 0.724 which implies $\beta \simeq 0.381$.

A related consideration is the optical model potential. The single particle potentials in standard uniform nuclear matter at zero temperature are obtained from Eq. (2.40). One obtains

$$V_n = V_p = -T_o\left[\alpha - \frac{3}{5}\beta - \frac{4}{3}\sigma\right] = -B - T_o(1+\beta), \tag{2.55}$$

where α and σ can be eliminated by using the saturation conditions Eqs. (2.45) and (2.46). Thus, the potential felt by a neutron with momentum p in standard nuclear matter is given by combining Eqs. (2.25) and (2.55):

$$U_n(p) = -B + T_o\left[-1 - \beta + \beta\Big(\frac{p}{P_o}\Big)^2\right]. \tag{2.56}$$

Setting $E_n = U_n + T_o(p/P_o)^2$ to be the total energy of the neutron, one can write

$$U_n(p) = -\frac{B}{1+\beta} - T_o + \frac{\beta}{1+\beta}E_n(p). \tag{2.57}$$

This results in a linear relation between U_n and E_n with a slope of $\beta/(1+\beta) = 1 - m^*/m_b$. The value $m^*/m_b = 0.724$ therefore implies a slope of 0.276, a result supported by experiment [24] . In addition, the value of the potential for a zero-momentum neutron is $-(T_o(1+\beta) + B) \simeq -68.59$ MeV which is also supported by experiment. For $\beta \simeq 0.381$, one obtains $\sigma = \beta'' - (6/5)\beta \simeq 1.460$.

The truncated model predicts the neutron and proton effective masses in pure neutron matter to be

$$\frac{m^*_{n0}}{m_b} = \frac{1}{1+\beta_L}, \qquad \frac{m^*_{p0}}{m_b} = \frac{1}{1+\beta_U}, \tag{2.58}$$

but these cannot be established without further input. In the original Myers & Swiatecki model [26], the β and σ parameters are not independent, but are related by

$$\sigma_L - \sigma_U = (\beta_L - \beta_U)\frac{\sigma}{\beta} = (\beta''_L - \beta''_U)\frac{\sigma}{\beta''} \simeq -0.833, \tag{2.59}$$

using the above values. While it is not necessary to constrain this parameter this way, in the absence of additional observables for fitting we follow the method of Myers & Swiatecki.

a	α_L	α_U	β_L	β_U	σ	
0.5882	1.1124	2.8823	0.08182	0.2991	1.4597	
ρ_0	B	m^*/m_b	ω_0	S_v	S'_v	
0.16545	16.539	0.7241	1.250	31.633	17.931	
T_o	K_o	K'_o	$t_{90-10,o}$	ω_δ	t_o	T_{co}
37.6794	315.91	1203.54	1.910	3.640	1.391	17.4

Table 2.1: Truncated parameter set. The first row contains parameters of the force model. The second row contains the assumed saturation properties of matter. The third row contains implied bulk matter and surface properties. Units are expressed in MeV and fm.

We therefore have

$$\sigma_{L,U} = \frac{\sigma}{2}\left(1 + \frac{\beta''_{L,U} - \beta''_{U,L}}{\beta''}\right), \tag{2.60}$$

or $\sigma_L \simeq 0.313$ and $\sigma_U \simeq 1.146$. Also,

$$\beta_{L,U} = \frac{5}{6}(\beta''_{L,U} - \sigma_{L,U}), \tag{2.61}$$

$\beta_L \simeq 0.0818$ and $\beta_U \simeq 0.299$. These lead to

$$\frac{m^*_{n0}}{m_b} \simeq 0.924, \qquad \frac{m^*_{p0}}{m_b} \simeq 0.770, \tag{2.62}$$

The parameters and the implied physical properties of matter and interfaces at saturation are contained in Table 2.1

In summary, the binding energy, saturation density, symmetry energy, symmetry energy derivative and effective mass can constrain 5 of the 6 independent parameters of the truncated model, namely $\alpha_{(L,U)}, \beta_{(L,U)}, \sigma$ and a. The parameter a can be determined by the symmetric matter surface energy or the surface diffuseness. In the truncated model, these choices determine the incompressibility parameter and its derivative as well as the surface symmetry energy parameter. Adjusting the incompressibility, its derivative, and surface symmetry energy parameters requires additional density-dependent terms in the interaction energy. This will be explored in the succeeding sections.

2.4 Two-Phase Equilibrium of Bulk Matter

In the general case of asymmetric matter and finite temperature, for two phases to be in bulk equilibrium, one minimizes the total free energy density for a given temperature, density and average proton fraction. We assume the electrons remain uniformly distributed so they need not be considered for this minimization. We also ignore the fact that protons are charged, an omission that will be included when we consider finite nuclei. We label the denser phase

as inside or I and the other phase as outside or II. The total free energy density is

$$\mathcal{F} = v\rho_I \mathcal{F}_I + (1-v)\rho_{II}\mathcal{F}_{II} \tag{2.63}$$

where the average density ρ and proton fraction x satisfy

$$\rho = v\rho_I + (1-v)\rho_{II}, \qquad \rho x = v\rho_I x_I + (1-v)\rho_{II}x_{II}, \tag{2.64}$$

where v is the volume fraction occupied by the dense phase. Minimizing $\mathcal{F}$ for a given ρ and x results in three bulk equilibrium conditions:

$$p_I = p_{II} \equiv p_o, \qquad \mu_{nI} = \mu_{nII} \equiv \mu_n, \qquad \mu_{pI} = \mu_{pII} \equiv \mu_p \tag{2.65}$$

Note that these conditions do not involve ρ, x or v. For a given value of $x_I = \rho_{pI}/\rho_I$, the bulk equilibrium conditions therefore determine ρ_{nI}, ρ_{nII} and ρ_{pII}. Phase equilibrium is possible for a given values of ρ, T and x if the resulting value of $v \in (0,1)$.

The phase equilibrium of dense matter using a Skyrme interaction at finite temperature was studied by Küpper, Wegmann & Hilf [14] for symmetric matter, and by Lattimer & Ravenhall [21], Buchler, J. R. & Barranco [1], Barranco & Buchler [6] , and by Lamb, Lattimer, Pethick & Ravenhall [16] for the general case. The phase equilibrium of dense matter using a relativistic field-theoretical interaction has been studied by Glendenning, Csernai & Kapusta [9] for symmetric matter and Müller and Serot [23] for asymmetric matter. Phase equilibrium with the finite-range force has heretofore not been previously studied for the general case of asymmetric hot matter.

2.4.1 Zero-Temperature Two-Phase Equilibrium

In the case of zero-temperature, $\mu_{pI} \simeq -16$ MeV < 0 and $\mu_{nI} \simeq -16$ MeV < 0 for $x_I \sim 0.5$, so $\rho_{pII} = \rho_{nII} = 0$. Two-phase equilibrium at zero temperature is then determined by ignoring the $\mu_{nI} = \mu_{nII}$ and $\mu_{pI} = \mu_{pII}$ conditions. However, for $x_I \lesssim 0.34$, $\mu_{nI} > 0$ so $\rho_{nII} > 0$ and neutron drip occurs. In this regime, equilibrium is determined by ignoring the $\mu_{pI} = \mu_{pII}$ condition. Note from Eq. (2.41) that as long as $\rho_{pII} = 0$, the proton chemical potential in the uniform light phase is determined by the local neutron density, *i.e.*,

$$\mu_{pII}(\rho_{pII} = 0) \equiv \mu_c = T_o\left(\frac{\beta_U''}{2}\left(\frac{2\rho_{nII}}{\rho_0}\right)^{5/3} - 2\alpha_U\frac{\rho_{nII}}{\rho_0}\right). \tag{2.66}$$

This critical chemical potential (μ_c) represents the threshold for proton drip[†]. When $\mu_{p_I} \geq \mu_c$, it becomes energetically favorable for protons to drip. This occurs near $x_I \simeq 0.09$. The behavior of the chemical potentials, densities and pressure in bulk equilibrium are shown in Fig. 2.2 as a function of the proton fraction in the dense phase.

Note that for very small values of x_I, the densities in the two uniform phases approach each other. For $x_I < 0.035$, in this model, bulk equilibrium becomes impossible and matter exists in a single uniform phase.

[†]At zero temperature, proton drip does not happen in neutron star crust but free protons exist in case of uniform nuclear matter if the phase transition happens in the outer core of neutron stars.

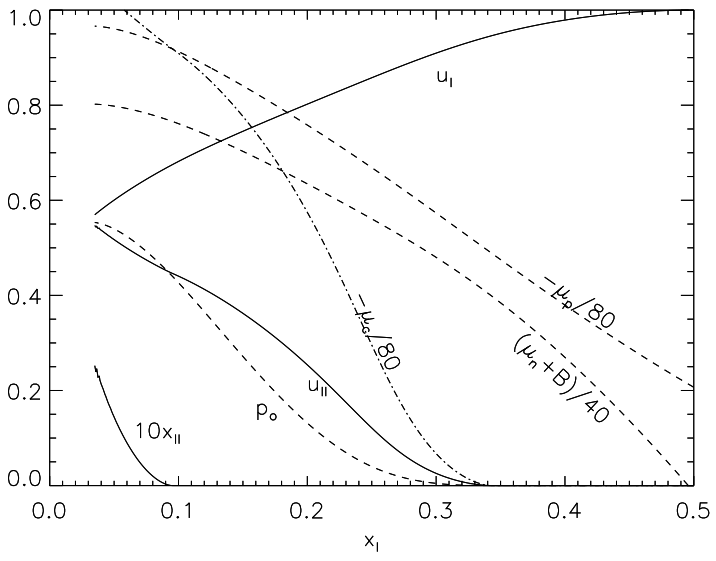

Figure 2.2: Bulk equilibrium of $T = 0$ asymmetric nuclear matter. The solid curves $u_I = \rho_I/\rho_0$ and $u_{II} = \rho_{II}/\rho_0$ show the densities at $T = 0$ for two phases in bulk equilibrium for various values of x_I, the proton fraction in the dense phase. The dashed curves show μ_n and μ_p; neutron drip [†] occurs when $\mu_n > 0$, or $x_I \simeq 0.34$ for the truncated finite-range model. Proton drip occurs when $\mu_p > \mu_c$, shown by the dashed-dot curve. Another solid curve shows the value of x_{II}, the proton fraction in the low-density phase. A dashed curve shows the pressure in bulk equilibrium. All units are in MeV and fm.

2.4.2 Finite-Temperature Symmetric Matter, the Critical Temperature, and the Coexistence Curve

Pressure isotherms are shown in Fig. 2.3 for the case of symmetric matter. For each temperature displayed, bold dots represent the two densities u_i and u_o, found from the solution of Eq. (2.65), that coexist in bulk equilibrium. Both phases have equal proton fractions. Matter with an average density u that satisfies $u_o < u < u_i$ lies within the coexistence region; the pressure of this matter is constant as the density is varied as indicated by the dotted lines connecting the bold dots. Coexistence is only possible up to the critical point, indicated by the open circle. It is clear from this figure that the critical point is defined by

$$\frac{\partial p}{\partial \rho}\Big|_T = \frac{\partial^2 p}{\partial \rho^2}\Big|_T = 0, \tag{2.67}$$

which is located at $T_{co} \simeq 17.3$ MeV and $u_{co} \simeq 0.350$. The critical pressure is $p_{co} \simeq 0.315$ MeV fm^{-3} for the truncated interaction. The coexistence region in the temperature-density plane is illustrated in the upper panel of Fig. 2.3. Dotted lines connect the two panels by indicating the two densities that coexist at each temperature or pressure below the critical values.

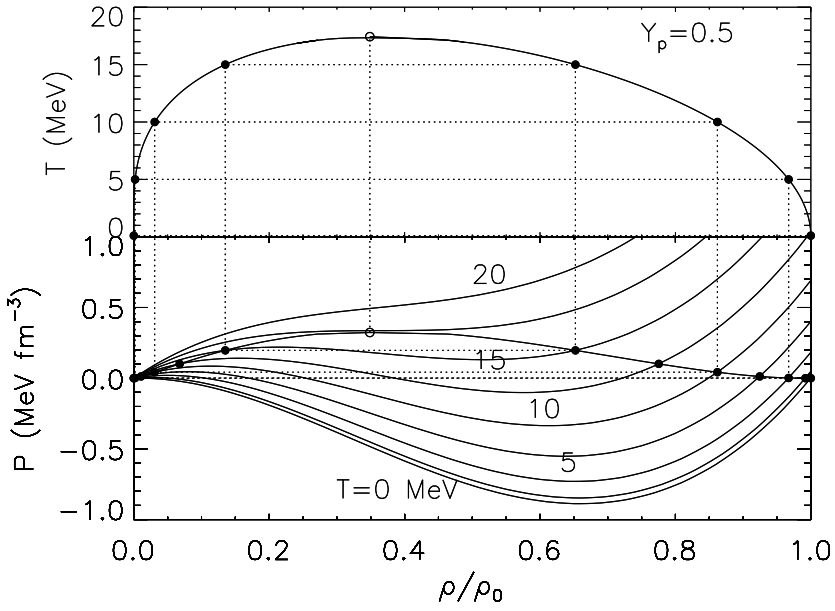

Figure 2.3: Pressure isotherms are shown in the lower panel. Bold dots indicate the boundary densities of the two-phase coexistence region. The upper panel shows the coexistence region in a density-temperature plot. The critical point is illustrated in each panel with an open circle.

2.4.3 Finite-Temperature Asymmetric Matter and Coexistence Curves

At finite temperature and arbitrary average proton fraction, the phase coexistence is determined by the conditions Eq. (2.65). The coexistence curves are the boundaries of the two-phase region determined by the conditions $v = 0$ or $v = 1$. In contrast to the symmetric matter case, the densities in each phase vary with the filling factor v at fixed T and Y_p. The coexistence curves are shown in Fig. 2.4. Along the phase boundary, the density of one phase is shown by the solid (coexistence) curve and the density of the other phase is shown by the corresponding dotted curve. Along the coexistence curve for each Y_p there is a critical point where the two phases have equal densities, $\rho_i = \rho_o$. As shown in Lattimer & Ravenhall [21], the critical point for asymmetric matter is determined from

$$\left.\frac{d\mu_n}{dx}\right|_{p,T} = \left.\frac{d^2\mu_n}{dx^2}\right|_{p,T} = 0. \tag{2.68}$$

The critical temperature as a function of dense-phase proton fraction x_I is shown in Fig. 2.5.

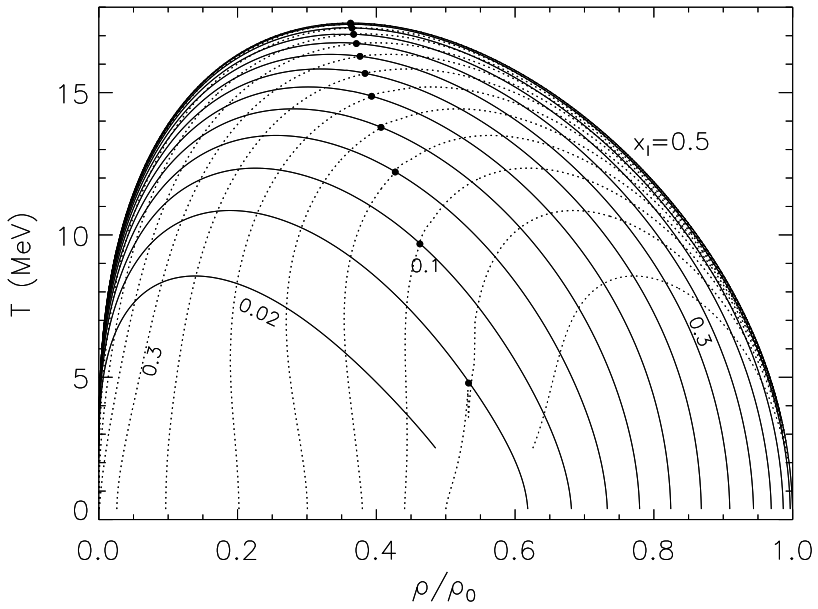

Figure 2.4: Coexistence curves for asymmetric matter for the truncated model at finite temperature. Solid curves show the boundary of the two-phase region for dense phase proton fractions ranging from $x_I = 0.5$ (upper-most curve) to $x_I = 0.02$ (lower-most curve) in increments of 0.04. At each density along a solid curve, matter with the indicated x_I is in bulk equilibrium with a less dense phase (which has a different proton fraction x_{II}) whose densities are indicated by the dotted curves. The densities of the two phases are equal at the critical points, indicated by solid dots.

2.5 The Nuclear Surface in the Semi-Infinite Approximation

A useful approximation for the nuclear surface is to treat the interface between two phases in bulk equilibrium in the limit that the curvature vanishes and Coulomb interactions are neglected. The surface is thus treated in a one-dimensional semi-infinite planar geometry, and the density profiles in the surface region are found by minimization of the total free energy.

2.5.1 The Euler Equations

The equilibrium matter distributions, $\rho_n(r), \rho_p(r)$, for a given temperature T are obtained by demanding that the total free energy F is stationary with respect to variations $\delta\rho_n$ and $\delta\rho_p$ subject to the constraints that the total neutron and proton numbers,

$$N = \int d^3r \rho_n, \qquad Z = \int d^3r \rho_p, \tag{2.69}$$

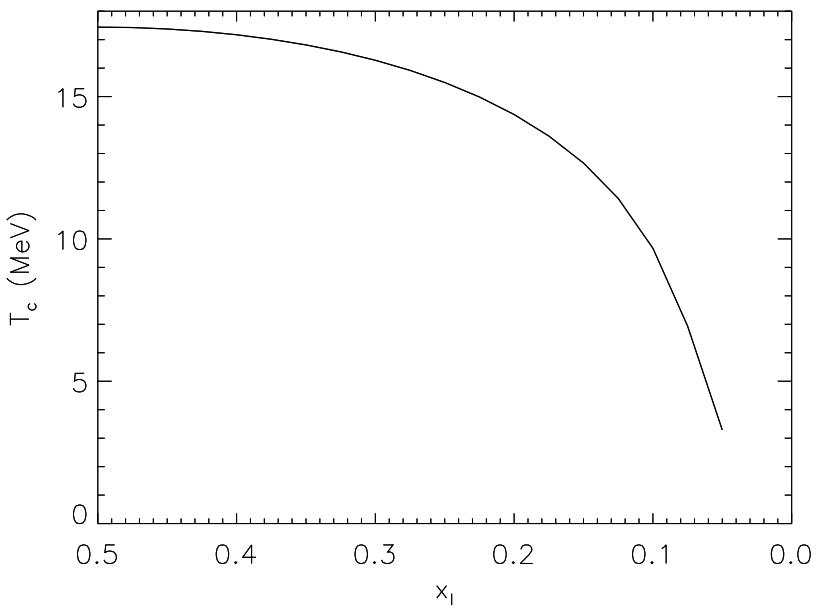

Figure 2.5: Critical temperature as a function of dense-phase proton fraction for the truncated model.

remain fixed. Note that, formally, F, N and Z diverge in the semi-infinite case since the integrals extend to $\pm\infty$. This divergence is irrelevant, however, as is discussed below.

Free energy stationarity is equivalent to demanding that the neutron and proton chemical potentials, $\mu_t = \partial\mathcal{E}/\partial\rho_t$, given by Eq. (2.28), are spatially constant. For a specific temperature and proton fraction in the dense phase far from the surface, x_I, the chemical potentials are therefore equal to their corresponding values for bulk equilibrium, as in Eq. (2.65). Thus, for the appropriate values for μ_n and μ_p, Eq. (2.28) becomes the Euler equations which determine ρ_n and ρ_p at every point.

The surface thermodynamic potential for a semi-infinite interface is the difference between the total thermodynamic potentials of the semi-infinite system in which two uniform phases in bulk equilibrium exist with a discontinuous density jump at the interface and the system in which the density varies according to free energy stationarity. Since μ_n and μ_p are spatially constant, this is equivalent to Ravenhall, Pethick & Lattimer [29] and Kolehmainen, Prakash & Lattimer [13]

$$\omega = \int_{-\infty}^{\infty} [\mathcal{E} - T(S_n + S_p) - \mu_n\rho_n - \mu_p\rho_p + p_o]dz = -\int_{-\infty}^{\infty} [p(z) - p_o]dz. \tag{2.70}$$

The last equality is not generally true for a non-relativistic potential and relativistic field-theoretical nuclear forces, but is true for the finite-range nucleon interaction. In general, a thermodynamic potential is a function of temperature and chemical potentials, but in the semi-infinite case one can write $\omega = \omega(T, x_I)$ since μ_n and μ_p are themselves functions only of T and x_I in bulk equilibrium. In other words, the values of the average density ρ and

proton fraction x are irrelevant for this calculation.

In practice, the integrals in Eqs. (2.69) and (2.70) are taken to extend from z_{II} to z_I which are located far to the right and left of the interface, respectively. The integrand of Eq. (2.70) must vanish far from the interface, according to Eq. (2.65), so these cutoffs do not affect the value of ω.

Surface Profiles and Tension for Zero-Temperature Symmetric Matter

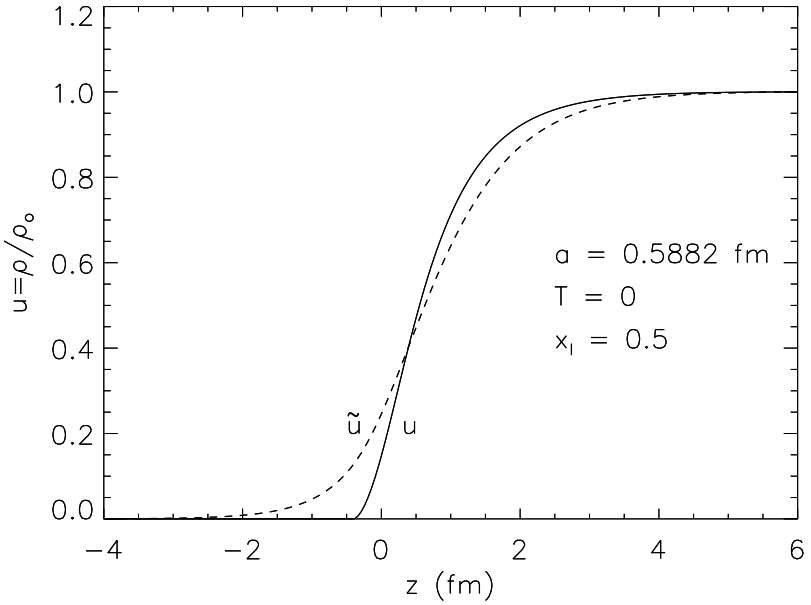

Figure 2.6: The density as a function of position for zero temperature symmetric matter is shown by the solid curve. The zero point of the $z-$axis is arbitrary. The function $\tilde{u}$ is shown by the dashed curve.

In the case of zero temperature symmetric matter, the energy density and Euler equations are

$$\mathcal{E} = T_o\rho_o\Big[\frac{3}{5}u^{5/3} - \frac{\alpha}{2}u\tilde{u} + \frac{\beta''}{4}u(\widetilde{u^{5/3}} + u^{2/3}\tilde{u})\Big], \tag{2.71}$$

$$\mu = -B = T_o\Big[u^{2/3} - \alpha\tilde{u} + \frac{\beta''}{2}(\widetilde{u^{5/3}} + \frac{5}{3}u^{2/3}\tilde{u})\Big]. \tag{2.72}$$

The density as a function of position is shown in Fig. 2.6. The integrand of Eq. (2.70) is

$$\begin{aligned} p_o - p =& T_o\rho_o\Big[-\frac{2}{5}u^{5/3} + \frac{\alpha}{2}u\tilde{u} - \frac{\beta''}{4}u(\widetilde{u^{5/3}} + \frac{7}{3}u^{2/3}\tilde{u})\Big] \\ =& \frac{\rho_o u}{2}\Big[\frac{T_o}{5}u^{2/3}(1-\tilde{u}) + B(1-u^{2/3}\tilde{u})\Big], \end{aligned} \tag{2.73}$$

where we used Eq. (2.72) to eliminate $\widetilde{u^{5/3}}$ and α, and Eq. (2.49) to eliminate β''. The

pressure, and also the integrand, must vanish at each extreme boundary, so that at one extremity, $u \to 1$ and at the other $u \to 0$, as is shown in Fig. 2.6. Obviously, in the limit $z \to \infty$, one has $u = \tilde{u} = 1$ since $du/dz \to 0$. From Eq. (2.72) one has $\mu = -B = T_o(1 - \alpha + (4/3)\beta'')$, which also follows from Eq. (2.49). At the point where $u = 0$, however, $du/dx \neq 0$ so $\tilde{u} \neq 0$. In this case one has

$$\mu = -B = T_o\Big(- \alpha\tilde{u} + \frac{\beta''}{2}\widetilde{u^{5/3}}\Big) \tag{2.74}$$

for which one finds $\tilde{u} \simeq 0.126$. The surface profile is shown in Fig. 2.6, found by solving Eq. (2.72) at each point in space. The function $\tilde{u}$ also is displayed in Fig. 2.6. It is obvious that since $\tilde{u}$ and u are both less than unity, the integrand Eq. (2.73) is always greater than or equal to zero.

The surface thermodynamic potential or surface tension depends only on the parameters α, β'' and a, so that given values for B and ρ_o, the surface tension depends only upon a in the absence of additional terms in the energy density. Myers & Swiatecki (1969) have noted that the surface tension at zero temperature for symmetric matter depends almost linearly on a and this is illustrated in Fig. 2.7. For the truncated model parameters, including $a = 0.5882$ fm, one obtains the physically reasonable value for the zero-temperature symmetric matter surface tension, $\omega(x = 1/2, T = 0) \equiv \omega_o \simeq 1.25$ MeV fm^{-2}. However, the calculated surface thickness is too small by about 20%, as will be shown below.

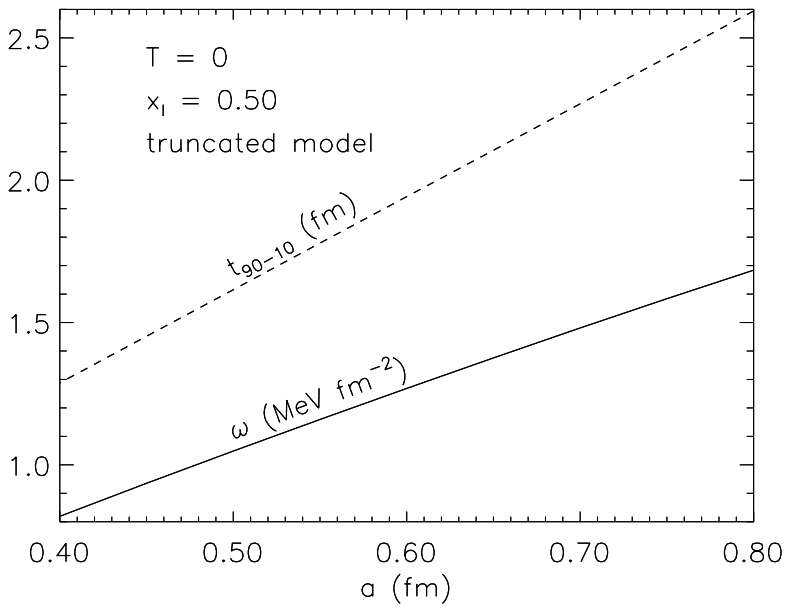

Figure 2.7: Surface tension (solid curve) and 90-10 surface thickness (dashed curve) for symmetric matter at zero temperature in the truncated finite-range Thomas Fermi model as functions of the diffuseness parameter a. The slopes of each are nearly linear.

It is instructive to compare these results for the surface with those established from a

potential model analogue for the Hamiltonian density of cold symmetric matter in which the free energy density is assumed to be composed of a bulk matter part $F_B(\rho)$ and a gradient term:

$$F = F_B + \frac{Q}{2}\rho'^2. \tag{2.75}$$

In the above, Q is a constant and $\rho' = d\rho/dz$. Minimizing the total free energy for a fixed number of particles introduces the Lagrangian parameter μ_o, which is equivalent to the chemical potential $-B$ for symmetric matter,

$$F_B - \mu_o\rho = \frac{Q}{2}\rho'^2. \tag{2.76}$$

Therefore the density gradient can be determined as a function of density:

$$\rho' = -\sqrt{\frac{2}{Q}}\sqrt{F_B - \mu_o\rho}. \tag{2.77}$$

The 90-10 surface thickness, t_{90-10} is defined as

$$t_{90-10} = z(\rho = 0.9\rho_i) - z(\rho = 0.1\rho_i) \tag{2.78}$$

in the case that $\rho_o = 0$. For F_B we substitute the free energy density of the truncated model for uniform symmetric matter at zero temperature, for which $\rho_i = \rho_o$:

$$\frac{F_B - \mu_o\rho}{T_o\rho_o} \equiv f_B = u\Big(1 - u^{1/3}\Big)^2\bigg[\frac{B}{T_o}\Big(1 + 2u^{1/3}\Big) + \Big(\frac{3B}{T_o} + \frac{3}{5}\Big)u^{2/3}\Big(1 + \frac{1}{2}u^{1/3}\Big)\bigg], \tag{2.79}$$

which defines the dimensionless function $f_B(u)$. This leads to

$$t_{90-10,o} = \int_{0.1\rho_o}^{0.9\rho_o} d\rho/\rho' = \sqrt{\frac{Q\rho_o}{T_o}}I_t, \tag{2.80}$$

where

$$I_t = \int_{0.1}^{0.9}\frac{du}{\sqrt{2f_B}} \simeq 3.042; \tag{2.81}$$

the numerical value is obtained using the truncated model with $B = 16.539$ MeV and $T_o = 37.679$ MeV. The symmetric matter surface tension is

$$\omega_o = \int_{-\infty}^{\infty}[F - \mu_o\rho]dz = 2\int_{-\infty}^{\infty}[F_B - \mu_o\rho]dz = \sqrt{QT_o\rho_o^3}I_\omega, \tag{2.82}$$

where

$$I_\omega = \int_0^1\sqrt{2f_B}du \simeq 0.2612, \tag{2.83}$$

where the numerical value is obtained with the same assumptions as previously. The quantity

Q can be eliminated by combining Eqs. (2.80) and (2.82),

$$\omega_o = \rho_o T_o t_{90-10,o} I_\omega / I_t \simeq 0.5353\ t_{90-10,o}\ \text{MeV fm}^{-3} = 1.231\ \text{MeV fm}^{-2}, \tag{2.84}$$

where the truncated model and a realistic value of the surface thickness
($t_{90-10,o} = 2.30$ fm) is used. This value of ω_o agrees well with that obtained from the numerical results for the truncated model (1.24 MeV fm^{-2}). However, as noted before, the calculated value of $t_{90-10,o}$ is 20% smaller than the realistic value. This discrepancy can be traced to the unrealistically large value of the incompressibility parameter K_o in the truncated model.

Surface Profiles and Tension for Zero-Temperature Asymmetric Matter

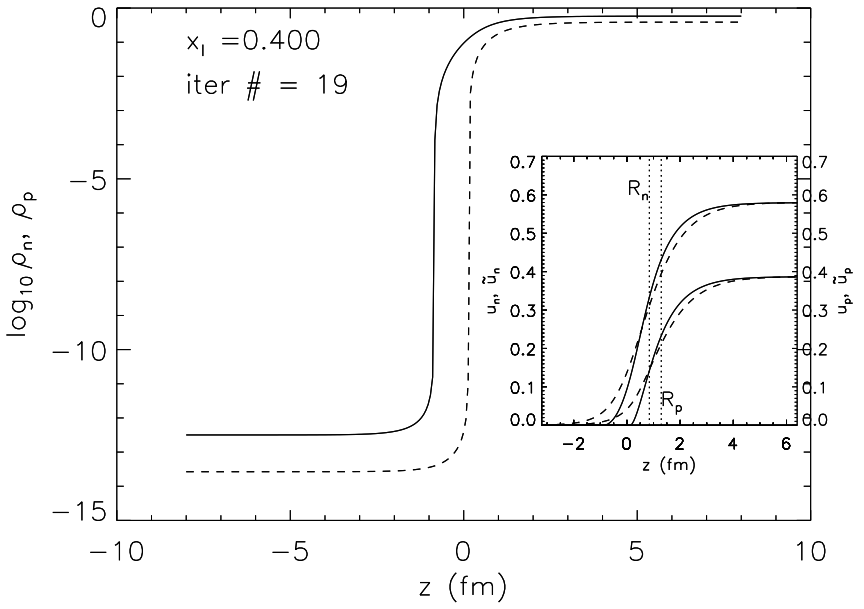

Figure 2.8: Neutron (solid line) and proton (dashed line) density profiles for the case $x_I = 0.4$ and $T = 0$ for a semi-infinite interface for the truncated interaction are indicated in the main panel in logarithmic units. The inset shows normalized profiles $u_n = \rho_n/\rho_o, u_p = \rho_p/\rho_o$ as solid curves on a linear scale, and the quantities $\tilde{u}_n = \widetilde{\rho_n}/\rho_o$ and $\tilde{u}_p = \widetilde{\rho_p}/\rho_o$ are displayed by dashed curves. The dotted lines indicate the positions of the squared-off neutron and proton radii, R_n and R_p respectively.

The density profiles for neutrons and protons for cold asymmetric matter are displayed in Fig. 2.8 for the case $x_I = 0.4$. Both the densities ρ_t and the quantities $\tilde{\rho}_t$ are shown. The squared-off radii R_n and R_p are also shown; these are defined by

$$\int_{z_I}^{z_{II}} \rho_t dz = \rho_{tI}(R_t - z_I) + \rho_{tII}(z_{II} - R_t) \tag{2.85}$$

with the convention that z_{II} is the boundary in the dilute phase and z_I is the boundary in the dense phase. Clearly we must take $z_I << 0$ and $z_{II} >> 0$, and in the calculation shown in Fig. 2.8 these were respectively chosen to be -8 fm and +8 fm.

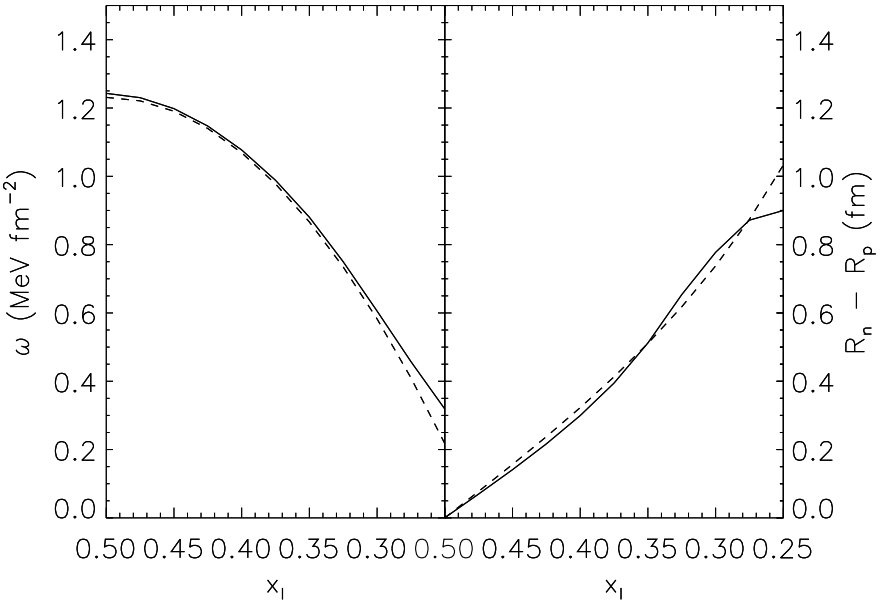

Figure 2.9: Surface tension (left panel) and neutron skin thickness (right panel) as functions of dense phase proton fraction for zero-temperature semi-infinite surfaces are shown as solid curves. In each case, dashed lines represent analytic estimates based on a simplified potential model as described in the text.

The surface thermodynamic potential for asymmetric matter at zero temperature is shown in Fig. 2.9. Analytic estimates of the symmetric matter surface thermodynamic potential ω_o and its dependence on proton fraction can be obtained from the potential approach discussed in section 2.5.1. In particular, specification of the symmetric matter surface thickness parameter $t_{90-10,o}$, determines ω_o via Eq. (2.84). The leading order dependence of the surface tension on proton fraction is quadratic with a coefficient ω_δ such that

$$\omega \simeq \omega_o - \omega_\delta \delta^2, \qquad \delta \equiv 1 - 2x_I. \tag{2.86}$$

In the potential approach, it can be shown in Steiner et al.[32] that the parameter ω_δ is, to lowest order,

$$\omega_\delta = S_v \sqrt{\frac{Q}{2}} \int_0^{\rho_o} \rho \Big(\frac{S_v}{E_{sym}} - 1 \Big) (F_B - \mu_o \rho)^{-1/2} d\rho, \tag{2.87}$$

where E_{sym} is the density dependent symmetry energy. In the truncated model E_{sym} is

$$S_v - E_{sym} = S_v\Big(1-u^{1/3}\Big)\times \\ \times\left[1+u^{1/3}+u^{2/3}-\frac{3(S_v-S_v')}{2S_v}u^{1/3}\Big(1+u^{1/3}\Big)-\frac{T_o}{3S_v}\Big(1-u^{1/3}\Big)\Big(1+\frac{1}{2}u^{1/3}\Big)\right]. \tag{2.88}$$

Eliminating Q using Eq. (2.82) and expressing the free energy density in terms of the truncated model energy density, one finds

$$\omega_\delta = \omega_o \frac{S_v}{T_o}\frac{I_\delta}{I_\omega}, \tag{2.89}$$

where

$$I_\delta = \int_0^1 \frac{u}{\sqrt{2f_B}}\left(\frac{S_v}{E_{sym}}-1\right)du \simeq 1.024. \tag{2.90}$$

The numerical value is obtained for the truncated model with the previously determined parameters and leads to the ratio $\omega_\delta/\omega_o \simeq 3.293$ and $\omega_\delta \simeq 4.054$ MeV fm^{-2}. It is also easy to show from Eq. (2.85) that the neutron skin thickness t can be written, to lowest order when $\rho_{II}=0$, as

$$t = R_n - R_p = \int_{-\infty}^{\infty}\left[\frac{\rho_n}{\rho_{nI}}-\frac{\rho_p}{\rho_{pI}}\right]dz \simeq \frac{2\omega_\delta\delta}{S_v\rho_o(1-\delta^2)}. \tag{2.91}$$

From this, we infer a normalized neutron skin thickness $t_o = t(1-\delta^2)/\delta$ which is predicted to be insensitive to asymmetry. The analytic approximations for surface properties using Eqs. (2.86), (2.89) and Eq. (2.91) are displayed in Fig. 2.9. The agreement between the analytic and numerical results is excellent. As an example, the difference between the numerical and analytic values for t_o is about $2\cdot 10^{-5}$ fm for small asymmetries. In addition, the dependence of t on asymmetry is in good agreement with the analytical prediction of Eq. (2.91).

Surface Tension for Finite-Temperature Matter

For the truncated model, the surface tension (thermodynamic potential density, ω) and surface thickness parameter (t_{90-10}) for finite-temperature symmetric matter are shown in Fig. 2.10. The truncated parameter set was employed. Both quantities vary as T^2 for small temperatures. The surface tension for symmetric matter can be well approximated for all temperatures by the expression

$$\omega(x=1/2,T) \simeq \omega_o\Big[1-(T/T_c)^2\Big]^{5/3}, \tag{2.92}$$

where $T_c \simeq 17.4$ MeV is the critical temperature for two-phase coexistence of symmetric matter and $\omega_o = \omega(x=1/2, T=0)$. This expression indicates the effective level density

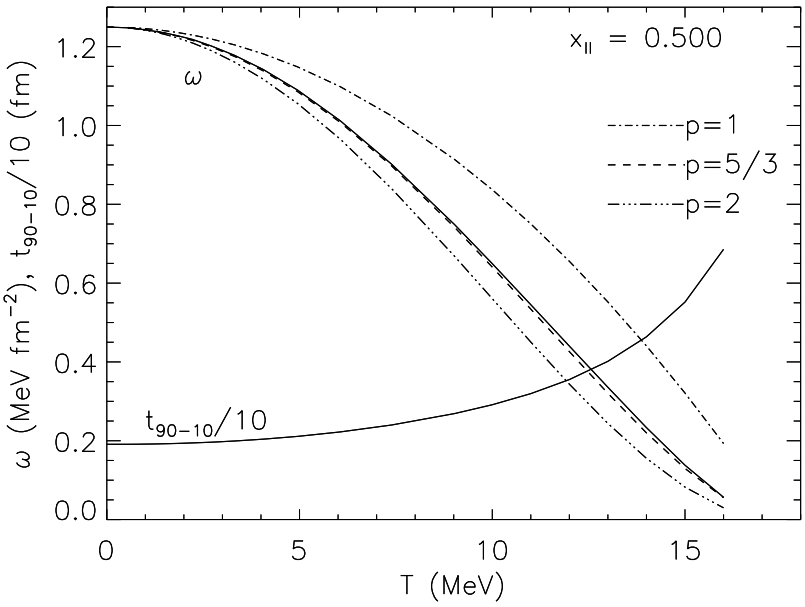

Figure 2.10: The surface tension of symmetric matter as a function of temperature is shown by the solid curve for the truncated model. The three accompanying dashed/dotted curves, labelled by the parameter p, show the temperature dependence $\omega_o[1-(T/T_{co})^2]^p$ where $T_{co} \simeq 17.4$ MeV is the critical temperature for two-phase coexistence of symmetric matter. In addition, the surface thickness parameter t_{90-10}, scaled by a factor 10, is displayed. At T_{co}, it tends to infinity.

parameter for nuclei has the approximate volume and surface contributions

$$\begin{aligned} a_{eff} = & \frac{2m^*}{\hbar^2}\Big(\frac{\pi}{3\rho_o}\Big)^{1/3} A + \Big(\frac{4\pi}{3\rho_o^2}\Big)^{1/3} \frac{10\omega_o}{T_{co}^2} A^{2/3} \\ \simeq & \ 0.059A \quad + \quad 0.226A^{2/3} \ \mathrm{MeV}^{-1}. \end{aligned} \tag{2.93}$$

Note that for $A \approx 64$ the surface and volume contributions to the nuclear specific heat are approximately equal.

For asymmetric matter, the temperature dependence of the surface tension is similar to that of symmetric matter. As shown in Fig. 2.11, the temperature dependence can be well-approximated by the relation Eq. (2.92) as long as T_c is reduced to the value (approximately 16.1 MeV) appropriate for $x_{II} = 0.3$. This figure also shows the surface thickness parameter t_{90-10} and the neutron skin thickness $R_n - R_p$.

Fig. 2.12 shows the surface tension and the neutron skin thickness as functions of x_{II} and T for the truncated model.

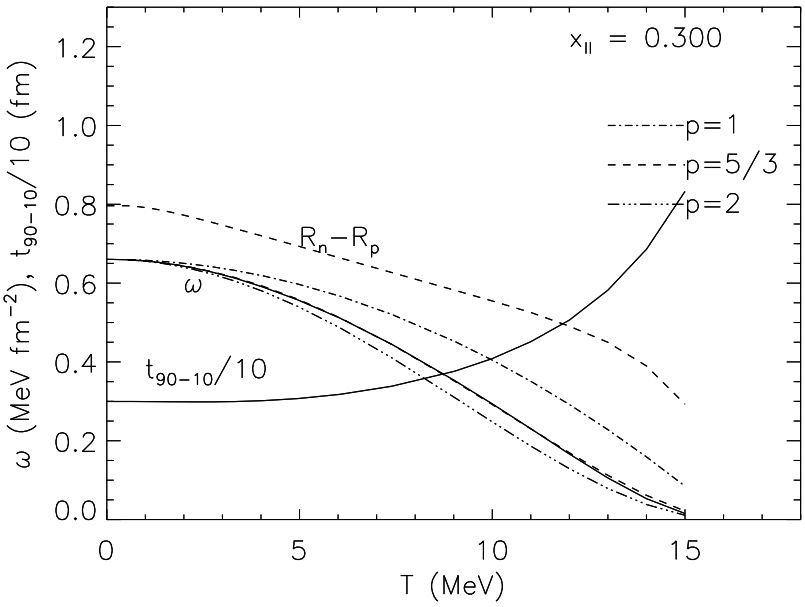

Figure 2.11: The same as Fig. 2.10 except for an asymmetric case with a dense phase proton fraction $x_I = 0.3$. In this case, the critical temperature is $T_c \simeq 16.1$ MeV. The dashed line shows the neutron skin thickness $R_n - R_p$ in fm.

2.6 Isolated Nuclei and Nuclei in Dense Matter

For the computation of finite nuclei, spherical symmetry and zero temperature are assumed in this model. These restrictions will be relaxed in a future publication. The main point of this model is to demonstrate the feasibility of efficiently computing the thermodynamic properties of nuclei in a consistent Thomas-Fermi approximation without the simplifications associated with the liquid droplet model. In contrast to the case of a semi-infinite interface, it is preferable in the finite nucleus case to choose values for N and Z, together with the temperature. The additional two constraints in Eq. (2.65) then determine the chemical potentials of the isolated nucleus, *i.e.*, a nucleus in a zero density environment.

2.6.1 Isolated Nuclei

The total energy of a nucleus must include the electrostatic Coulomb energy

$$E_{Coul} = \frac{e^2}{2} \int_V d^3r \int_V d^3r' \frac{[\rho_p(r) - \rho_e(r)][\rho_p(r') - \rho_e(r')]}{|r - r'|} \,, \tag{2.94}$$

where the spatial integrals are over the entire volume. In the case of an isolated nucleus, $\rho_e = 0$, and the integrand is finite only within the nucleus. The contribution of the Coulomb energy to the proton chemical potential can be found from a variation of E_{Coul} with respect

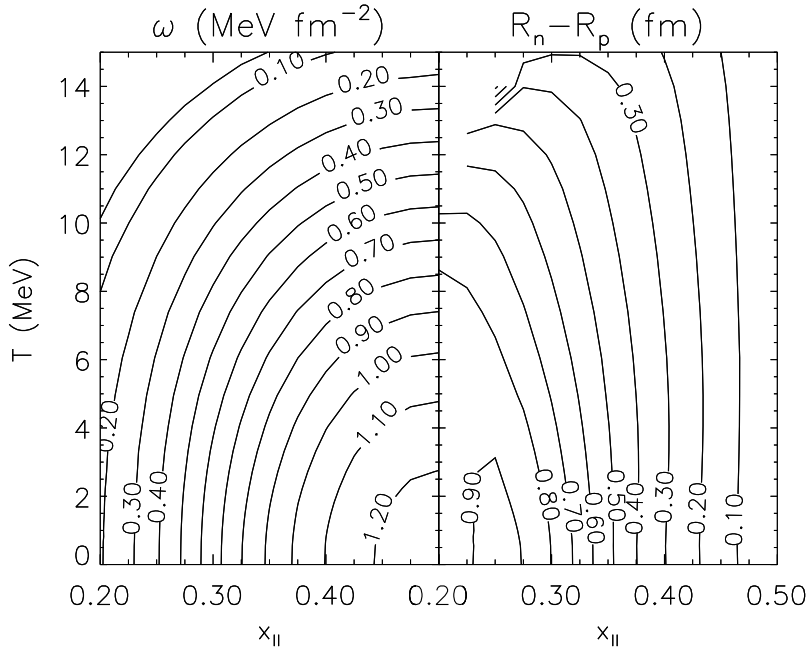

Figure 2.12: Contour plots of surface tesion and $R_n - R_p$
Finite temperature asymmetric matter: (Left panel) A contour plot of the surface tension (ω, MeV-fm^{-2}); (Right panel) A contour plot of the neutron skin thickness ($R_n - R_p$, fm).

to the proton density: $\Delta\mu_p = \delta E_{Coul}/\delta\rho_p$. One obtains

$$\delta E_{Coul} = \frac{e^2}{2}\int_V d^3r \int_V \frac{d^3r'}{|r-r'|}(\delta\rho_p(r)[\rho_p(r') - \rho_e(r')] + \delta\rho_p(r')[\rho_p(r) - \rho_e(r)]). \tag{2.95}$$

One can reverse the variables r and r' in the second term of the double integral, yielding

$$\begin{aligned}\Delta\mu_p(r) =& e^2\int_V \frac{d^3r'}{|r-r'|}[\rho_p(r') - \rho_e(r')] \\ =& 4\pi e^2\left[\frac{1}{r}\int_0^r r'^2[\rho_p(r') - \rho_e(r')]dr' + \int_r^{R_c} r'[\rho_p(r') - \rho_e(r')]dr'\right],\end{aligned} \tag{2.96}$$

where we assumed spherical symmetry in the second line and R_c is taken to have a value much larger than that of the nucleus. In the limit $r \to 0$, the first integral vanishes. In the limit $r \to R_c$, one has $\Delta\mu_p(R_c) = 0$ because of charge neutrality. The quantity $\Delta\mu_p(r)$ must be added to the nucleonic part of $\mu_p(r)$.

The total Coulomb energy can be written

$$E_{Coul} = \frac{1}{2}\int_V [\rho_p(r) - \rho_e(r)]\Delta\mu_p(r)d^3r, \tag{2.97}$$

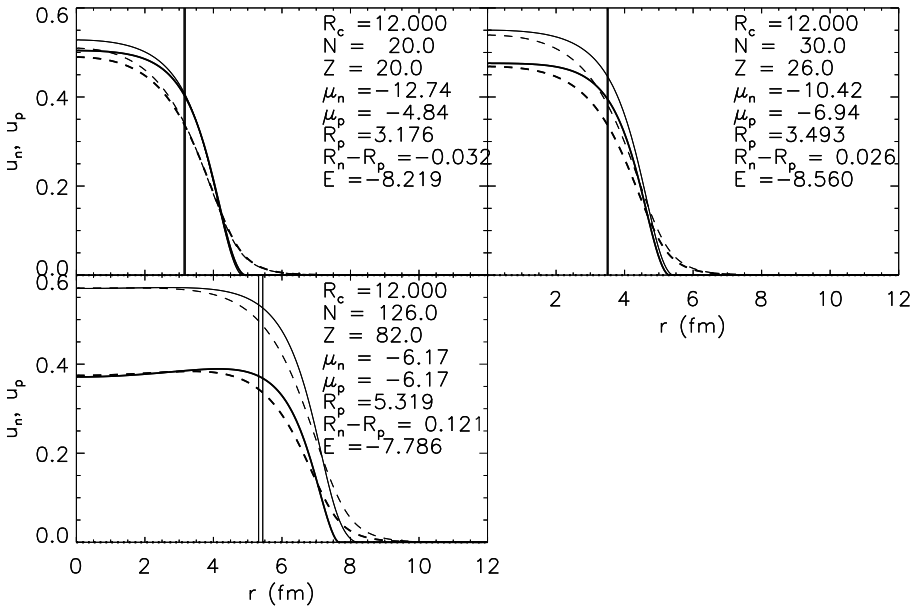

Figure 2.13: Neutron and proton density profiles for the nuclei ^{40}Ca, ^{56}Fe and ^{208}Pb in the truncated model are shown as solid curves. The densities u_t are scaled by the saturation density ρ_s. Dashed curves show the corresponding functions $\widetilde{u}_t$. The chemical potentials, the charge radius R_p, the neutron skin thickness $\delta R = R_n - R_p$, and the ground state energy E are included in each subfigure. The vertical lines show R_n and R_p.

so that the Coulomb contribution to the energy density is just

$$\mathcal{E}_{Coul} = \frac{1}{2}(\rho_p - \rho_e)\Delta\mu_p. \tag{2.98}$$

Density profiles for the isolated nuclei ^{40}Ca, ^{56}Fe and for ^{238}U are displayed in Fig. 2.13 for the truncated interaction model and assuming $T = 0$. The specific ground state energies, charge radii and neutron skin thicknesses for these nuclei are included in the figure. The charge radius is R_p and the skin thickness is $R_n - R_p$ and are defined by

$$R_p = \left(\frac{\int \rho_p r^2 d^3r}{\int \rho_p d^3r}\right)^{1/2}, \qquad R_n = \left(\frac{\int \rho_n r^2 d^3r}{\int \rho_n d^3r}\right)^{1/2}. \tag{2.99}$$

The ground state energy is measured relative to A free neutrons, and hence includes the energy $-(m_n - m_p)c^2(Z/A)$ from the neutron-proton mass difference.

2.6.2 Dense Matter and the Wigner-Seitz Approximation

In the case of nuclei at finite density, such as those in a neutron star crust, it is convenient to employ the Wigner-Seitz approximation in which a cell of radius R_c contains a single nucleus and sufficient electrons to neutralize the cell. In this paper, we will assume that the Wigner-Seitz cell has a spherical geometry, but this assumption can be relaxed. In the case of finite density, therefore, the density of electrons is finite and their distribution must be considered in addition to those of the nucleons. The average density of the cell is $\rho = 3(N+Z)/(4\pi R_c^3)$. In a neutron star crust, it is logical to specify the density ρ, and optimize the beta-equilibrium energy per particle with respect to the density profiles and N and Z, which determines R_c, μ_n and μ_p. The two additional equations needed, in addition to the Euler equations Eq. (2.28), are equivalent to the beta equilibrium condition

$$\mu_n - \mu_p + (m_n - m_p)c^2 = \mu_e \tag{2.100}$$

and the energy minimization

$$\left(\frac{\partial E}{\partial R_c}\right)_\beta = 0 \tag{2.101}$$

where beta equilibrium is assumed.

In a neutron star crust, where the density $\rho >> 10^6$ g cm^{-3} and $T < 1$ MeV, the electrons are relativistic and degenerate. In this case, the electron density, which is modified by the Coulomb potential, is given in terms of the electron chemical potential μ_e at the cell boundary by

$$\rho_e(r) = \frac{1}{3\pi^2}\left(\frac{\mu_e + \Delta\mu_p(r)}{\hbar c}\right)^3. \tag{2.102}$$

Eqs. (2.96) and (2.102) must be solved by iteration. In beta equilibrium, one has $\mu_e = \mu_n(R_c) - \mu_p(R_c) + (m_n - m_p)c^2$ since $\Delta\mu_p(R_c) = 0$.

Nuclei for several different locations in a neutron star crust at $T = 0$ are displayed in Fig. 2.14. For densities $\rho \geq 0.00028$ fm^{-3} the neutron chemical potential is positive and dripped neutrons appear. In this case, the number of neutrons in the nucleus is estimated from

$$N_{nuc} = \rho_{n0}\frac{N - 4\pi\rho_{nR_c}R_c^3/3}{\rho_{n0} - \rho_{nR_c}}, \tag{2.103}$$

where ρ_{n0} is the neutron density at the nucleus center and ρ_{nR_c} is the neutron density at the cell boundary. Note that when neutron drip does not occur, N_{nuc} is not exactly equal to N. In addition, in the case of dripped neutrons, the mean-square neutron radius is redefined to be

$$R_n = \left(\frac{\int(\rho_n - \rho_{nR_c})r^2 d^3r}{\int(\rho_n - \rho_{nR_c})d^3r}\right)^{1/2}. \tag{2.104}$$

The trend is for proton number Z to decrease with increasing density, as is shown in Fig. 2.15. The energy minimum is very sensitive to the neutron and proton numbers which

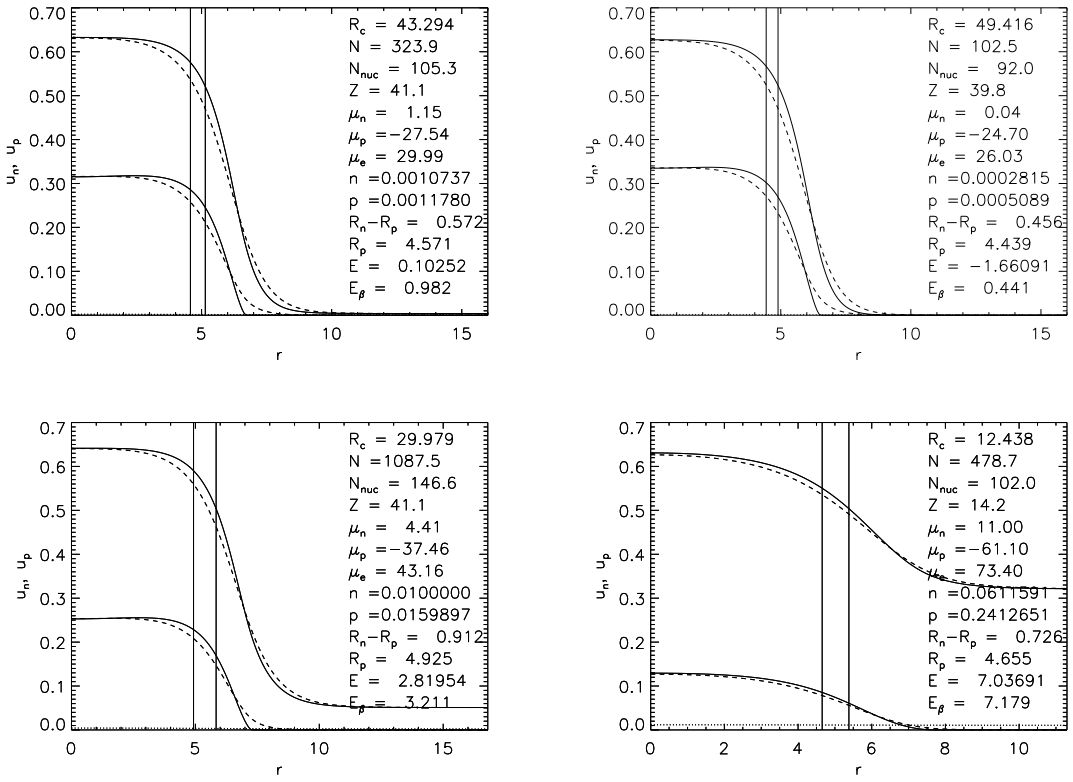

Figure 2.14: Neutron and proton density profiles for nuclei in the cold crust of a neutron star. The optimum nucleus for each density ρ (fm^{-3}) is shown, together with the pressure p (MeV fm^{-3}), the total internal energy per baryon E (MeV), the charge radius R_p (fm), the neutron skin thickness $R_n - R_p$, and the chemical potentials μ_n, μ_p and μ_e (MeV). N, Z and N_{nuc} are defined in the text. R_c is the Wigner-Seitz cell size and E_β is the energy of uniform nuclear matter in beta equilibrium.

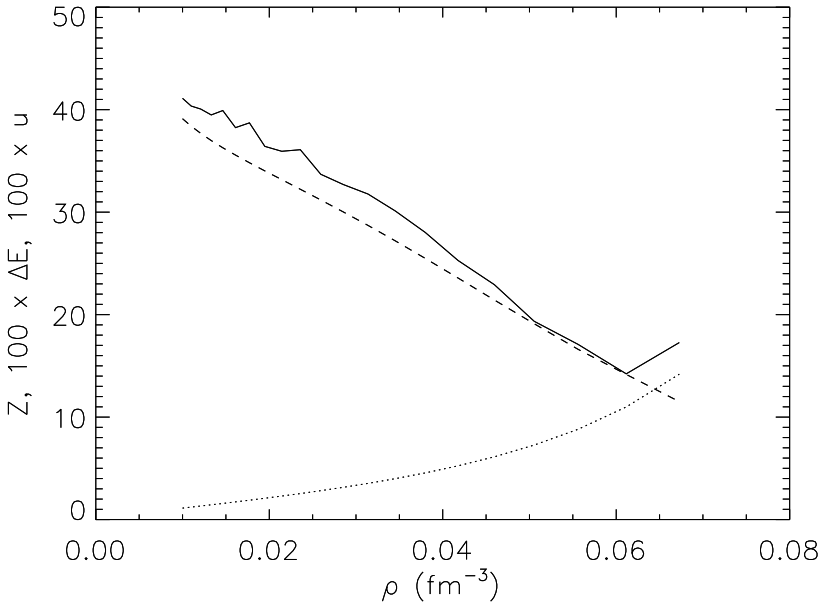

Figure 2.15: Proton number per unit Wigner-Seitz cell for dense matter for the truncated model is shown by the solid curve. The energy advantage (MeV/baryon, multiplied by 100) relative to uniform matter in beta equilibrium is shown by the dashed curve. The filling factor u, defined in Eq. (2.105) and multiplied by 100, is shown by the dotted curve.

accounts for the wiggles shown in this figure. This figure also shows the filling factor

$$u = \frac{\rho - \rho_0}{\rho_0 - \rho_{R_c}}, \tag{2.105}$$

which increases with density, and the energy advantage of nuclei over that of uniform nuclear matter (both considered in beta equilibrium), $\Delta E = E - E_\beta$, which decreases with density. ΔE decreases to zero before the filling factor approaches the value 1/2 for which matter might expect to be turned inside out (Lamb et al.[15]).

In general, the Wigner-Seitz cell size R_c decreases with increasing density and the nuclear filling factor in the absence of dripped nucleons, $(R/R_c)^3$, where $R \approx (R_n + R_p)/2$, therefore increases. However, the nuclear mass fraction decreases with density because of dripped neutrons and, as a result, the filling factor u increases less rapidly than it would otherwise. The Coulomb energy decreases with density, and eventually nuclei become unstable to deformations. In the simple analysis of Ravenhall et al.[58], significant deformations from sphericity occur when the filling factor is larger than about 1/8. From the results displayed here, this occurs when $\rho \simeq 0.06$ fm^{-3}. At this point, the energy difference between nuclei and uniform matter is small, being only about 0.13 MeV per baryon, and the energy difference even disappears by densities near $\rho = 0.09$ fm^{-3}. Thus the density domain in which significantly deformed nuclei appear is probably relatively small in this case. Lamb et al.[16] demonstrated that the nuclei will tend to turn "inside-out" when a filling factor larger than

1/2 obtains, but this appears to be unlikely to ever occur for this model. To explore these questions further requires one to consider non-spherical geometries for nuclei.

2.7 Conclusions

This chapter demonstrates the feasibility of employing a finite-range nuclear interaction to efficiently compute nuclear properties in the Thomas-Fermi approximation, and it extends these calculations to the computation of the properties of hot, dense matter using unit Wigner-Seitz cells. The method is efficient enough to allow the computation of full tables that are densely-enough spaced in density, temperature, and electron fraction for astrophysical applications. Before such a table can be generated, however, there are a few details of the model that may have to be modified.

The model described in this model does not adequately describe realistic nuclear incompressibilities or the properties of nuclear surfaces. However, these items can be straightforwardly corrected by the addition of density-dependent terms to the nuclear interactions. In addition, better fits to nuclear effective masses and the optical model potential can be accommodated by additional momentum-dependent terms. Future work will explore possible modifications and will undertake a detailed comparison to the properties of nuclei.

In addition, Danielewicz [7] pointed out an apparent inconsistency with the liquid droplet treatment developed by Myers & Swiatecki [24] and by Lattimer et al.[17]. with respect to its incorporation of the symmetry and Coulomb properties of nuclei. Danielewicz proposed an alternate formulation of the liquid droplet model. However, Steiner et al.[32] pointed out discrepancies between the predictions of the two approaches concerning the symmetry properties of extremely neutron-rich nuclei and neutron skin thickness. The present model should be immune to any discrepancy involved with the liquid droplet model and, furthermore, should provide a suitable platform with which to resolve this controversy. This point will be addressed in a future publication.

Following the resolution of these points, we intend to generate a series of three-dimensional tables suitable for astrophysical simulations, and we will compare their properties to the Lattimer-Swesty [22] and Shen et al.[61] equations of state.

Chapter 3

Modified model

† The truncated model is quite successful in representing isolated nuclei and dense matter. However, the truncated model has a too large nuclear incompressibility and nuclear surface tension. We added new density dependent interactions so that we can resolve them.

3.1 Original Modification to Myers & Swiatecki Model

We considered an alternative density dependent interaction term which has an energy density contribution that is proportional to $\rho^{1+\epsilon}$:

$$\begin{aligned} C_{\eta L} &= -\frac{h^3}{4} T_o \rho_o \left(\frac{3}{4\pi P_o^3}\right)^2 \eta_L \left(\frac{2}{\rho_o}\right)^\epsilon \left(\frac{\rho_{t1}^\epsilon + \rho_{t2}^\epsilon}{2}\right) \\ C_{\eta U} &= -\frac{h^3}{4} T_o \rho_o \left(\frac{3}{4\pi P_o^3}\right)^2 \eta_U \left(\frac{2}{\rho_o}\right)^\epsilon \left(\frac{\rho_{t1}^\epsilon + \rho_{t'2}^\epsilon}{2}\right) \end{aligned} \tag{3.1}$$

where η_L, η_U, and ϵ are parameters. The total energy is altered by the amount

$$\begin{aligned} \Delta E =& \frac{1}{2}\frac{T_o}{\rho_o}\left(\frac{2}{\rho_o}\right)^\epsilon \int d^3r_1 d^3r_2 \, f(r_{12}/a) \times \\ & \sum_t [\eta_L \rho_{t1}\rho_{t2}(\rho_{t1}^\epsilon + \rho_{t2}^\epsilon)\eta_U \rho_{t1}\rho_{t'2}(\rho_{t1}^\epsilon + \rho_{t2'}^\epsilon) \, . \end{aligned} \tag{3.2}$$

The contribution to the potential is

$$\Delta V_t = \frac{T_o}{\rho_o}\left(\frac{2}{\rho_o}\right)^\epsilon \left(\eta_L \left[(1+\epsilon)\rho_t^\epsilon \tilde{\rho}_t + \widetilde{\rho_t^{1+\epsilon}}\right] + \eta_U \left[(1+\epsilon)\rho_t^\epsilon \tilde{\rho}_{t'} + \widetilde{\rho_{t'}^{1+\epsilon}}\right]\right) , \tag{3.3}$$

while the energy density contribution is

$$\Delta \mathcal{E} = \frac{1}{2}\frac{T_o}{\rho_o}\left(\frac{2}{\rho_o}\right)^\epsilon \sum_t \rho_t \left[\eta_L \left(\rho_t^\epsilon \tilde{\rho}_t + \widetilde{\rho_t^{1+\epsilon}}\right) + \eta_U \left(\rho_t^\epsilon \tilde{\rho}_{t'} + \widetilde{\rho_{t'}^{1+\epsilon}}\right)\right] . \tag{3.4}$$

†This chapter is an improved version of the truncated model in Chapter 2. This work will be submitted to the journal soon.

In the case of uniform matter, the additional contribution to the energy density is

$$\Delta\mathcal{E} = \frac{T_o}{\rho_o}\left(\frac{2}{\rho_o}\right)^{\epsilon}\sum_t \rho_t^{1+\epsilon}\left[\eta_L\rho_t + \eta_U\rho_t'\right]. \tag{3.5}$$

For standard nuclear matter ($u = 1$, $x = 1/2$, T=0 MeV), one finds, after defining $\eta = \eta_L + \eta_U$,

$$\begin{aligned}
\frac{\epsilon_o}{\rho_o} &= -B = T_o\left[\frac{3}{5} - \frac{\alpha}{2} + \frac{\beta''}{2} + \frac{\eta}{2}\right], \\
p_o &= 0 = \rho_o T_o\left[\frac{2}{5} - \frac{\alpha}{2} + \frac{5}{6}\beta'' + \frac{\eta}{2}(1+\epsilon)\right], \\
K_o &= T_o\left[6 - 9\alpha + 20\beta'' + \frac{9\eta}{2}(1+\epsilon)(2+\epsilon)\right], \\
K_o' &= T_o\left[4 - 9\alpha + \frac{100}{3}\beta'' + \frac{9\eta}{2}(1+\epsilon)^2(2+\epsilon)\right], \\
S_v &= T_o\Bigg[\frac{1}{3} + \frac{\alpha_U - \alpha_L}{2} + \frac{5}{9}(2\beta_L'' - \beta_U'') \\
&\qquad + \frac{1+\epsilon}{4}([2+\epsilon]\eta_L - 2[2-\epsilon]\eta_U)\Bigg], \\
S_v' &= T_o\Bigg[\frac{2}{9} + \frac{\alpha_U - \alpha_L}{2} + \frac{25}{27}(2\beta_L'' - \beta_U'') \\
&\qquad + \frac{(1+\epsilon)^2}{4}([2+\epsilon]\eta_L - 2[2-\epsilon]\eta_U)\Bigg].
\end{aligned} \tag{3.6}$$

Practical considerations[†] limit the value of ϵ to the range $0 < \epsilon < 2/3$. For a given value of K_o, a solution of Eq. (3.6) yields the consequence that K_o' is nearly independent of ϵ.

[†]To determine the range of ϵ, we check the pressure behavior of pure neutron matter.

We choose the value $\epsilon = 1/3$. One may show in this case that

$$\begin{aligned}
\alpha &= \frac{9}{5} + \frac{5B}{T_o} + \frac{1}{\epsilon}\left(\frac{3}{5} + \frac{5B}{T_o} - \frac{K_o}{3T_o}\right) = \frac{18}{5} + \frac{20B}{T_o} - \frac{K_o}{T_o}\,, \\
\beta'' &= \left(1 - \frac{3\epsilon}{2}\right)^{-1}\left[\frac{K_o}{2T_o} - \frac{3}{10} - \frac{9B}{2T_o} - \epsilon\left(\frac{9B}{2T_o} - \frac{9}{10}\right)\right] \\
&= \frac{K_o}{T_o} - \frac{6}{5} - \frac{12B}{T_o}\,, \\
\eta &= \frac{1}{\epsilon}\left(1 - \frac{3\epsilon}{2}\right)^{-1}\left(\frac{3}{5} + \frac{5B}{T_o} - \frac{K_o}{3T_o}\right) = 6\left(\frac{3}{5} + \frac{5B}{T_o} - \frac{K_o}{3T_o}\right)\,, \\
K_o' &= \frac{14}{3}K_o - 15B - \frac{3}{5}T_o + \epsilon\left(K_o - 15B - \frac{9}{5}T_o\right) \\
&= 5K_o - 20B - \frac{6}{5}T_o\,.
\end{aligned} \tag{3.7}$$

Therefore, to reduce K_o from the truncated model value of 316 MeV to the experimental value, e.g. 230 MeV, requires a value $\eta \simeq 172/T_o \simeq 4.3$, and α and β'' are respectively changed by $+\eta/2$ and $-\eta/2$. In this case, $K_o' \simeq 780$ MeV.

For $\epsilon = 1/3$, we find

$$\begin{aligned}
S_v &= T_o\left[\frac{1}{3} + \frac{\alpha}{2} - \alpha_L + \frac{5}{3}\beta_L'' - \frac{5}{9}\beta'' + \frac{4}{3}\eta_L - \frac{5}{9}\eta\right], \\
S_v' &= T_o\left[\frac{2}{9} + \frac{\alpha}{2} - \alpha_L + \frac{25}{9}\beta_L'' - \frac{25}{27}\beta'' + \frac{16}{9}\eta_L - \frac{20}{27}\eta\right].
\end{aligned} \tag{3.8}$$

In practice, for $K_o \simeq 230$ MeV, $\beta'' \simeq 0$ and both $\alpha \simeq 6$ and $\eta \simeq 4$ are positive. Symmetric matter therefore has positive pressure for $u > 1$. Pure neutron matter, on the other hand, has pressure

$$p_N = T_o\rho_o u\left[\frac{2}{5}(2u)^{2/3} - \alpha_L u + \frac{5}{3}2^{2/3}\beta_L'' u^{5/3} + \frac{4}{3}2^{1/3}\eta_L u^{4/3}\right]. \tag{3.9}$$

At ρ_o, p_N has a value about half of the non-interacting Fermi pressure, Combining this result with reasonable values $S_v = 30$ MeV and $S_v' = 15$ MeV, one finds $\alpha_L \simeq 7.2$, $\beta_L'' \simeq -3.4$ and $\eta_L \simeq 9.4$. In the case $S_v' = 30$ MeV, one finds $\alpha_L \simeq 13.3$, $\beta_L'' \simeq -6.3$ and $\eta_L \simeq 17.5$. In both cases, p_N turns negative at low densities $u < 2.5$ because $\beta_L'' < 0$.

The problem can be more clearly observed if one forms the combination $Q = e_N - e_s - S_v$, where e_N is the neutron energy per baryon and $e_s = \mathcal{E}/\rho$ is the symmetric matter energy per baryon. Nominally, the magnitude of Q evaluated at the saturation density, $Q_1 \equiv Q(u = 1)$,

is expected to be small, $|Q_1| \leq 1$ MeV. In our case,

$$Q = T_o\left[\frac{3}{5}u^{2/3}\left(2^{2/3}-\frac{14}{9}\right)+\left[\frac{\beta''}{18}+\left(2^{2/3}-\frac{5}{3}\right)\beta''_L\right]u^{5/3} + \left[\frac{\eta}{18}+\left(2^{1/3}-\frac{4}{3}\right)\eta_L\right]u^{1+\epsilon}\right] \tag{3.10}$$

Thus, for $S_v = 30$ MeV and $S'_v = 15$ MeV, $Q_1 \simeq -6.5$ MeV. Therefore, in general, the non-quadratic terms involving β''_L and η_L lead to neutron matter energy and pressure that are not well-behaved at higher densities in comparison to symmetric energies and pressures.

Another possibility is to require that $Q_1 \approx 0$, specifically

$$\frac{\beta''}{18}+\left(2^{2/3}-\frac{5}{3}\right)\beta''_L+\frac{\eta}{18}+\left(2^{1/3}-\frac{4}{3}\right)\eta_L = 0\,. \tag{3.11}$$

Using Eqs.(3.8) and (3.11), we can evaluate $\alpha_L = -4.0$, $\beta''_L = -1.4$, and $\eta_L = 4.6$ using $\epsilon = 1/3$, $S_v = 30$ MeV, and $S'_v = 15$ MeV. Once again, the negative value of β''_L renders neutron matter unstable at high densities.

3.2 Alternate Modification

Most Skyrme forces explicitly incorporate the η terms with a quadratic x dependence so that they, unlike the α terms, vanish in Eq. (3.10), and the surviving β''_L term can be made small. It will be necessary for us to formulate a force with similar properties. One way to do this is to make the extra terms in $C_{L,U}$ functionals of ρ_1 only (or ρ_2). For example,

$$\begin{aligned} C_{\eta L} &= -\frac{h^3}{4}T_o\rho_o\left(\frac{3}{4\pi P_o^3}\right)^2\eta_L\left(\frac{2}{\rho_o}\right)^\epsilon\left(\frac{\rho_1^\epsilon+\rho_2^\epsilon}{2}\right) \\ C_{\eta U} &= -\frac{h^3}{4}T_o\rho_o\left(\frac{3}{4\pi P_o^3}\right)^2\eta_U\left(\frac{2}{\rho_o}\right)^\epsilon\left(\frac{\rho_1^\epsilon+\rho_2^\epsilon}{2}\right) \end{aligned} \tag{3.12}$$

Then,

$$\begin{aligned} \Delta E =& \frac{1}{2}\frac{T_o}{\rho_o}\int d^3r_1 d^3r_2\, f(r_{12}/a)\times \\ & \left[\left(\frac{\rho_1}{\rho_o}\right)^\epsilon+\left(\frac{\rho_2}{\rho_o}\right)^\epsilon\right]\sum_t \rho_{t1}\Big[\eta_L\rho_{t2}+\eta_U\rho_{t'2}\Big] \\ =& \frac{T_o}{\rho_o}\int d^3r\left(\frac{\rho}{\rho_o}\right)^\epsilon\sum_t\rho_t\Big[\eta_L\tilde{\rho}_t+\eta_U\tilde{\rho}_{t'}\Big]\,. \end{aligned} \tag{3.13}$$

We find

$$\Delta\mathcal{E} = \frac{T_o}{\rho_o}\left(\frac{\rho}{\rho_o}\right)^\epsilon\sum_t\rho_t\Big[\eta_L\tilde{\rho}_t+\eta_U\tilde{\rho}_{t'}\Big]\,, \tag{3.14}$$

$$\Delta V_t = \frac{T_o}{\rho_o}\left[\left(\frac{\rho}{\rho_o}\right)^\epsilon \left[\frac{\epsilon}{\rho}\sum_t \rho_t(\eta_L\tilde{\rho}_t + \eta_U\tilde{\rho}_{t'}) + \eta_L\tilde{\rho}_t + \eta_U\tilde{\rho}_{t'}\right] + \eta_L\hat{\rho}_t + \eta_U\hat{\rho}_{t'}\right], \tag{3.15}$$

where

$$\hat{\rho}_t(r_1) = \int d^3r_2 f(r_{12}/a)\left(\frac{\rho_2}{\rho_o}\right)^\epsilon \rho_{t2}\,. \tag{3.16}$$

In uniform matter, one finds

$$\begin{aligned}
\Delta\mathcal{E} &= \frac{T_o}{\rho_o}\left(\frac{\rho}{\rho_o}\right)^\epsilon \left[\eta_L(\rho_n^2+\rho_p^2) + 2\eta_U\rho_n\rho_p\right], \\
\Delta V_t &= \frac{T_o}{\rho_o}\left(\frac{\rho}{\rho_o}\right)^\epsilon \left[\epsilon\left(\eta_L\frac{\rho_n^2+\rho_p^2}{\rho} + 2\eta_U\frac{\rho_n\rho_p}{\rho}\right) + 2\eta_L\rho_t + 2\eta_u\rho_{t'}\right], \\
\Delta p &= \frac{T_o}{\rho_o}\left(\frac{\rho}{\rho_o}\right)^\epsilon (1+\epsilon)\left[\eta_L(\rho_n^2+\rho_p^2) + 2\eta_U\rho_n\rho_p\right].
\end{aligned} \tag{3.17}$$

In terms of the proton fraction,

$$\begin{aligned}
\frac{\Delta\mathcal{E}}{\rho_o} &= T_o u^{1+\epsilon}\left(\eta_L\left[x^2+(1-x)^2\right] + 2\eta_U x(1-x)\right), \\
\Delta p &= T_o\rho_o u^{2+\epsilon}\left(\eta_L\left[x^2+(1-x)^2\right] + 2\eta_U x(1-x)\right).
\end{aligned} \tag{3.18}$$

For standard nuclear matter, we now obtain

$$\begin{aligned}
\frac{\epsilon_o}{\rho_o} &= -B = T_o\left[\frac{3}{5} - \frac{\alpha}{2} + \frac{\beta''}{2} + \frac{\eta}{2}\right] \\
p_o &= 0 = \rho_o T_o\left[\frac{2}{5} - \frac{\alpha}{2} + \frac{5}{6}\beta'' + \frac{\eta}{2}(1+\epsilon)\right] \\
K_o &= T_o\left[6 - 9\alpha + 20\beta'' + \frac{9\eta}{2}(1+\epsilon)(2+\epsilon)\right] \\
K'_o &= T_o\left[4 - 9\alpha + \frac{100}{3}\beta'' + \frac{9\eta}{2}(1+\epsilon)^2(2+\epsilon)\right] \\
S_v &= T_o\left[\frac{1}{3} + \frac{\alpha}{2} - \frac{5}{9}\beta'' - \frac{\eta}{2} - \alpha_L + \frac{5}{3}\beta''_L + \eta_L\right], \\
S'_v &= T_o\left[\frac{2}{9} + \frac{\alpha}{2} - \frac{25}{27}\beta'' - (1+\epsilon)\frac{\eta}{2} - \alpha_L + \frac{25}{9}\beta''_L + (1+\epsilon)\eta_L\right]
\end{aligned} \tag{3.19}$$

Solving, we have

$$\begin{aligned}
\alpha &= \frac{9}{5} + \frac{5B}{T_o} + \frac{1}{\epsilon}\left(\frac{3}{5} + \frac{5B}{T_o} - \frac{K_o}{3T_o}\right) = \frac{18}{5} + \frac{20B}{T_o} - \frac{K_o}{T_o}\,, \\
\beta'' &= \frac{5K/T_o - 3 - 9\epsilon - 45(1+\epsilon)B/T_o}{10 - 15\epsilon} = \frac{K_o}{T_o} - \frac{6}{5} - \frac{12B}{T_o}\,, \\
\eta &= \frac{18 - 10K/T_o + 150B/T_o}{15\epsilon(2-3\epsilon)} = \frac{18}{5} + \frac{30B}{T_o} - \frac{2K}{T_o}\,, \\
K'_o &= \frac{14}{3}K_o - 15B - \frac{3}{5}T_o + \epsilon\left(K_o - 15B - \frac{9}{5}T_o\right) \\
&= 5K_o - 20B - \frac{6}{5}T_o\,.
\end{aligned} \tag{3.20}$$

The last expressions are obtained with $\epsilon = 1/3$. We also find, for $\epsilon = 1/3$,

$$\begin{aligned}
S_v &= T_o\left[\frac{1}{3} + \frac{\alpha}{2} - \alpha_L + \frac{5}{3}\beta''_L - \frac{5}{9}\beta'' + \eta_L - \frac{\eta}{2}\right], \\
S'_v &= T_o\left[\frac{2}{9} + \frac{\alpha}{2} - \alpha_L + \frac{25}{9}\beta''_L - \frac{25}{27}\beta'' + \frac{4}{3}\eta_L - \frac{2}{3}\eta\right].
\end{aligned} \tag{3.21}$$

Pure neutron matter has pressure

$$p_N = T_o\rho_o u\left[\frac{2}{5}(2u)^{2/3} - \alpha_L u + \frac{5}{3}2^{2/3}\beta''_L u^{5/3} + (1+\epsilon)\eta_L u^{4/3}\right] \tag{3.22}$$

(3.23)

At ρ_o, p_N has a value about half of the non-interacting Fermi pressure. Combining this result with reasonable values $S_v = 30$ MeV and $S'_v = 15$ MeV, and assuming $\epsilon = 1/3$, one finds $\alpha_L \simeq -4.4$, $\beta''_L \simeq 3.6$, and $\eta_L \simeq -10.7$. In the case $S'_v = 30$ MeV, one finds $\alpha_L \simeq -8.4$, $\beta''_L \simeq 6.7$, and $\eta_L \simeq -19.9$. In both cases, since $\beta''_L > 0$, the neutron matter pressure will continuously rise with u.
However, we now observe that

$$Q = T_o\left[\frac{3}{5}u^{2/3}\left(2^{2/3} - \frac{14}{9}\right) + \left[\frac{\beta''}{18} + \left(2^{2/3} - \frac{5}{3}\right)\beta''_L\right]u^{5/3}\right], \tag{3.24}$$

evaluated at the saturation density and using $\epsilon = 1/3$, $S_v = 30$ MeV and $S'_v = 15$ MeV, is $Q_1 \simeq -10.3$ MeV. Obviously, the neutron matter properties and the symmetry properties cannot be separately adjusted.

Most Skyrme forces have the properties that both Q_1 and $Q'_1 \equiv (dQ(u)/d\ln u)_1 = [p_n - p_s - S'_v]$ have small magnitudes: if they don't, their neutron matter has problems. Setting

Q_1 to a small number also results in small values for Q'_1. since for $\epsilon = 1/3$, the value of β'' is nearly zero, setting $\beta''_L = 0$ will ensure that Q_1 is small. The coupled set of equations to determine α_L and η_L in this case are

$$\begin{aligned} \frac{S_v}{T_o} &= \frac{1}{3} + \frac{\alpha}{2} - \frac{\eta}{2} - \alpha_L + \eta_L \,, \\ \frac{S'_v}{T_o} &= \frac{2}{9} + \frac{\alpha}{2} - \frac{2}{3}\eta - \alpha_L + \frac{4}{3}\eta_L \,. \end{aligned} \tag{3.25}$$

These result in

$$\begin{aligned} \alpha_L &= \frac{2}{3} + \frac{\alpha}{2} - \frac{\eta}{2} - \frac{4S_v - 3S'_v}{T_o} \simeq 1.6 \,, \\ \eta_L &= \frac{1}{3} + \frac{\eta}{2} - 3\frac{S_v - S'_v}{T_o} \simeq 1.1 \,. \end{aligned} \tag{3.26}$$

The neutron matter energy and pressure are now implicitly closely coupled to S_v and S'_v such that $e_{N,1} \simeq S_v - B$ and $p_{N,1}/\rho_o \simeq S'_v$. For Hebler & Schwen [63] estimates of $e_{N,1} \simeq 14$ MeV and $p_{N,1}/\rho_o \simeq 2$ MeV, we find $S_v \simeq 30$ MeV and $S'_v \simeq 10$ MeV. In this case, $\alpha_L \simeq 1.2$ and $\eta_L \simeq 0.7$.

Alternatively, one could use a value of $\epsilon < 1/3$, resulting in $\beta'' > 0$. To ensure $Q_1 \equiv 0$, a positive value for β''_L is also obtained. This results in different values for α_L and η_L and a different relation between S_v, S'_v and $e_{N,1}$, $p_{N,1}$.
Thus, it would be interesting to fit nuclei to determine the correlation between S_v and S'_v for a couple different values of ϵ, such as 1/3 or 1/6. One could then also add the correlations for S_v and S'_v obtained from the relations reduced from theoretical studies of neutron matter energy and pressure at the saturation density.

3.3 Optimized Parameter Set

Adding new density dependent interactions solves nuclear incompressibility, optical potential, and pure neutron matter properties. To find an optimized parameter set, $\alpha_{L,U}$, $\beta_{L,U}$, and, $\eta_{L,U}$, we may compare the experimental binding energy of single nucleus with theoretical calculation from the modified model. For this set, we fix $\beta'' = 0$, which gives proper nuclear incompressibility ($K \simeq 235$ MeV) and varies S_v and $S'_v (= L/3)$. Since the experimental error in the binding energy is extremely small, so that it is meaningless if we define χ^2 in conventional way, instead we define the χ^2 as

$$\chi^2 = \frac{1}{N} \sum \left(\frac{B_{ex,i} - B_{th,i}}{\sigma} \right)^2 \tag{3.27}$$

where $N(= 2336)$ is the total number of nuclei in the calculation and σ is a mean error (arbitrary). The $B_{ex,i}$ is the data [45] and $B_{th,i}$ is the numerical calculation.
The $\chi\sigma$ has a unit of MeV so we can estimate the mean difference between B_{ex} and B_{th} in each calculation. Even though our code is fast to calculate single nucleus's properties, the number of calculation for this contour plot is $2336 \times 41 \times 41 \sim 4 \cdot 10^6$ so we wrote a simple

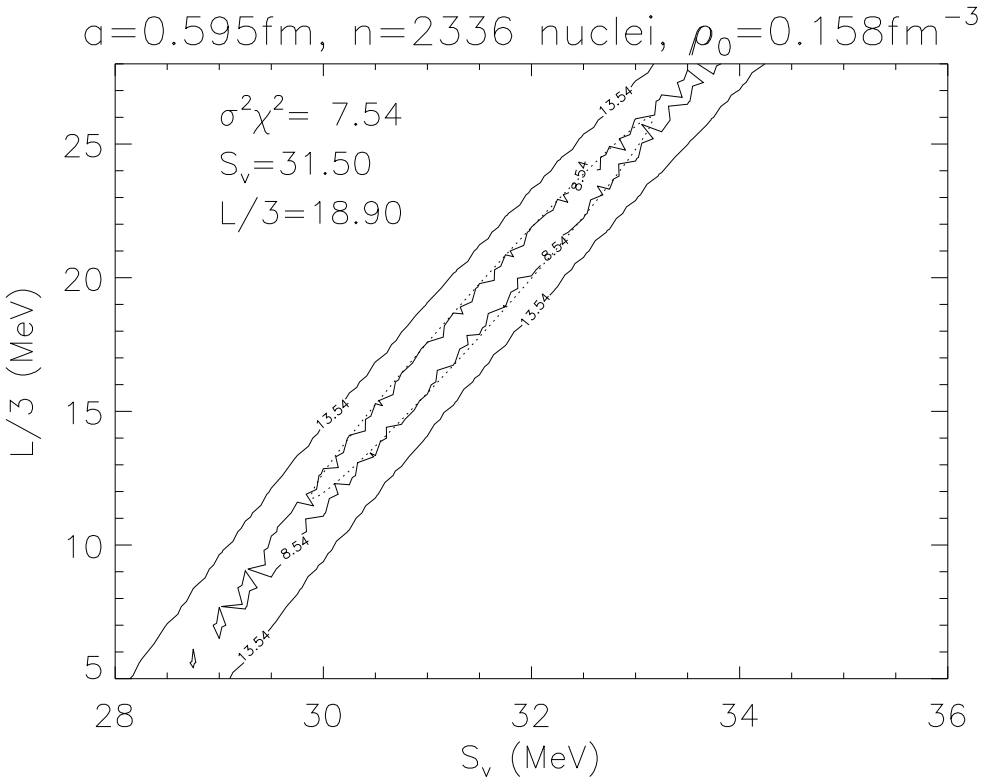

Figure 3.1: Solid line shows the contour plot of S_v and L from FRTF II model. There is a strong correlation between S_v and L. The dotted ellipse at the center represent statistical calculation from Eq. (3.28) (3.29), which makes $\chi^2 = 8.54$.

parallel code for it. Fig. 3.1 shows the contour plot of S_v and L using FRTF II. The dotted ellipse at the center is a statistical calculation from Eq. (3.28) and (3.29), which makes $\chi^2 = 8.5$ to compare with the contour plot from numerical calculation. This contour plot implies strong correlation between S_v and L. This strong correlation also implies the strong correlation between S_s and S_v in liquid droplet model when we extract the information of S_s from semi-infinite nuclear matter using FRTF model.
The $\chi^2\sigma^2 = 7.54$ MeV^2 gives mean error $\sqrt{7.54}/100 \sim 0.027$ MeV per nucleon. This $\chi^2\sigma^2$ can be reduced upto 4.72 MeV^2 if we add semi-empirical formula for pairing $12/\sqrt{A}$ and shell effects. We used the Taylor expansion for $\chi^2\sigma^2$ to find σ_{S_v} and σ_L which are

$$\sigma^2\left[\chi^2(\mathbf{p}) - \chi_0^2\right] = \sum_{i,j=1}^{2} \delta p_{ij} \mathcal{M}_{ij} \delta p_{ij} \tag{3.28}$$

where $\mathbf{p} = (S_v, L)$ and $\mathcal{M}_{ij} = \frac{1}{2}\partial_{p_i}\partial_{p_j}|_{\mathbf{p}}$. Then the definition of σ_{S_v}, σ_L, and $R_{S_v,L}$ are given by

$$\begin{aligned}
\sigma_{S_v}^2 &= \frac{2\partial_L^2\chi^2}{\partial_{S_v}^2\chi^2\,\partial_L^2\chi^2 - (\partial_{S_v}\partial_L\chi^2)^2}\sigma^2 \\
\sigma_L^2 &= \frac{2\partial_{S_v}^2\chi^2}{\partial_{S_v}^2\chi^2\,\partial_L^2\chi^2 - (\partial_{S_v}\partial_L\chi^2)^2}\sigma^2 \\
R_{S_v,L} &= -\frac{\partial_{S_v}\partial_L\chi^2}{\sqrt{\partial_{S_v}^2\chi^2\,\partial_L^2\chi^2}}
\end{aligned} \tag{3.29}$$

Fig. 3.2 shows the 95% confidence interval of S_v and L from FRTF II and Kortelainen et al. [46] Our result has a simliar mean points of S_v and L with Kortelainen et al. but strong correlation since Kortelainen et al. chose several parameters such as ρ_s, R_{np}, K at the same time. The S_v and L are on the same line and very close to each other.

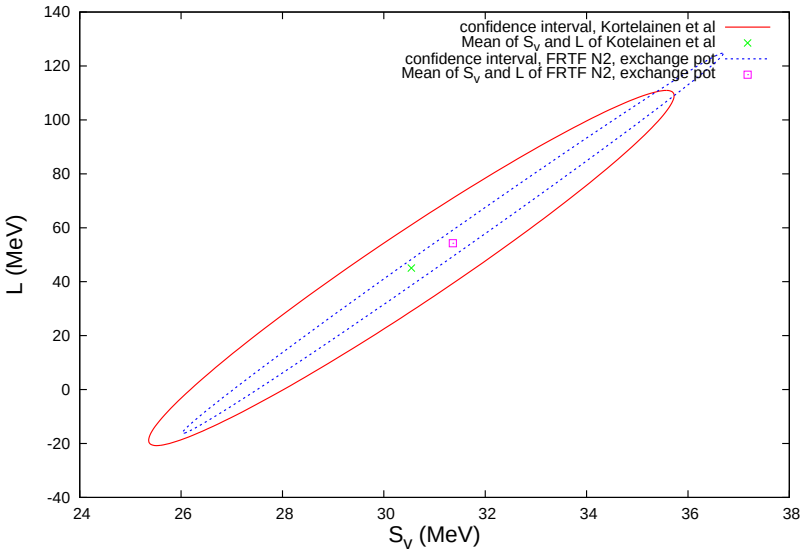

Figure 3.2: This figure shows 95% confidence interval from FRTF II and Kortelainen et al. [46]. The red (blue) ellipse is the result from Kortelainen et al. (FRTF II). Our result has the similar slope with Kortelaine et al. but a stronger correlation. Kortelainen et al. assumed $\sigma = 2$ MeV, for FRTF II we used $\sigma = 1.6$ MeV.

Recently Lattimer and Lim [47] summarized the allowed region of S_v and L and compared those result with liquid droplet model. Our optimized values of S_v and L are also inside the overlapped region of S_v and L from several experimentally allowed region.
Fig. 3.3 shows S_v and L allowed region. The blue sky region is the result from Sn neutron skin [48]. GDR comes from giant dipole resonance [49]. There is a restriction from ^{208}Pb dipole polarizability [52]. HIC represents the result from heavy ion collision [51]. Nuclear masses is the result from Korelainen et al. [46]. The hatched region comes from neutron

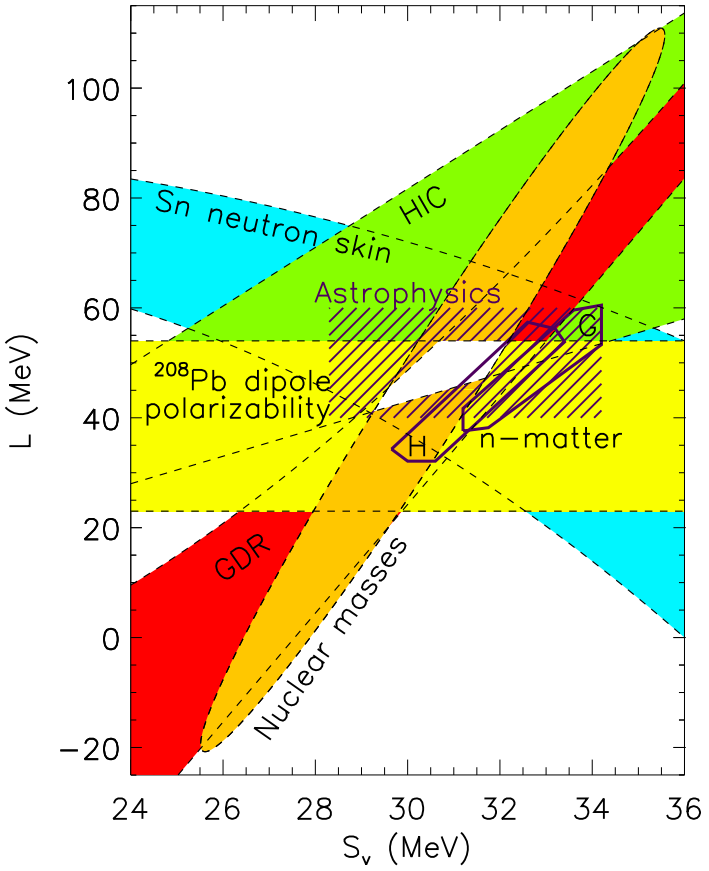

Figure 3.3: Several experimental result can restrict the S_v and L. Our optimized S_v and L are in the white overlapped region in the middle of the figure [47].

star observations [53]. There are also pure neutron matter calculations with purple polygons [54, 55]. This allowed region of S_v and L will give important constraints to develop new nuclear force model in the future.

3.4 Nuclear Surface Tension

Compared with the truncated model, the modified model has a lower critical temperature and surface tension. These properties will be used to construct E.O.S table using liquid droplet approach. In the liquid droplet approach (chapter 6), the surface tension as a function of T and proton fraction x is required.

The critical temperature for asymmetric nuclear matter occurs when the dilute and dense matter have the same density and proton fraction. In general, the proton fractions in both dense and dilute matter is different each other except for symmetric nuclear matter. The surface tension can be obtained only numerically using Eq. (2.70).
The surface tension for nuclear matter at finite temperature and given proton fraction can be approximated [17] by

$$\omega(x_i, T) = \omega_0(x_i)\left[1 - \left(\frac{T}{T_c(x_i)}\right)^2\right]^p . \tag{3.30}$$

For both the truncated model and the new model, $p = 5/3$ explains the numerical behaviors very well.
The critical temperature at which both the dilute and dense phase have the same density and proton fraction, is approximated by

$$T_c(x_i) = T_c(x_i = 0.5)(1 + a(1 - 2x_i)^2 + b(1 - 2x_i)^4 + c(1 - 2x_i)^6) . \tag{3.31}$$

The a, b, and c can be obtained by χ^2 minimization between the numerical result and fitting

Table 3.1: The critical temperature analytic fitting function

Model	$T_{c,0}$	a	b	c
Truncated	17.354	-0.5006	0.66126	-1.33316
New	14.626	-0.4296	0.34216	-1.00298

function. Fig. 3.4 shows the plot of critical temperature of numerical and fitting function. This fitting function is used to calculate finite temperature surface tension in Eq. (3.30).
The surface tension at $T = 0$ MeV and $Y_p = 0.5$ is also a function of proton factions. ω_0 can be approximated with fractional function as in LS model,

$$\omega_0(x_i) = \omega_0(x_i = 0.5)\frac{2 \cdot 2^\alpha + q}{x_i^{-\alpha} + q + (1 - x_i)^{-\alpha}} \tag{3.32}$$

The parameter α is left free so that we can choose from 2 to 4.0 and q is obtained from χ^2 minimization. For both models, the best α's are 3.6 and 3.7.

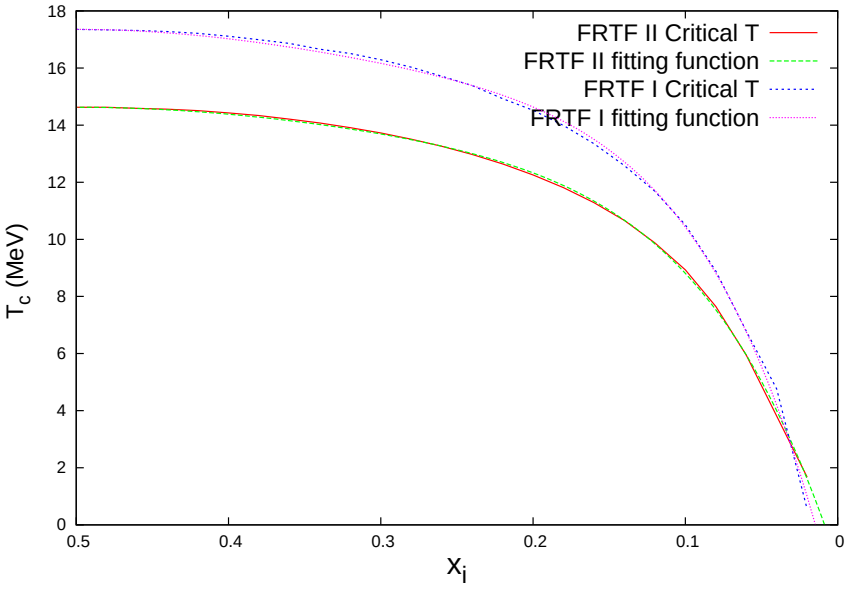

Figure 3.4: The critical temperature as a given proton fraction: Numerical result and analytic fitting function.

Table 3.2: Surface tension analytic fitting function for finite range model

Model	$\omega_0(x_i = 0.5)$	α	q
Truncated	1.25728	3.6	39.0552
New	1.02824	3.7	56.0479

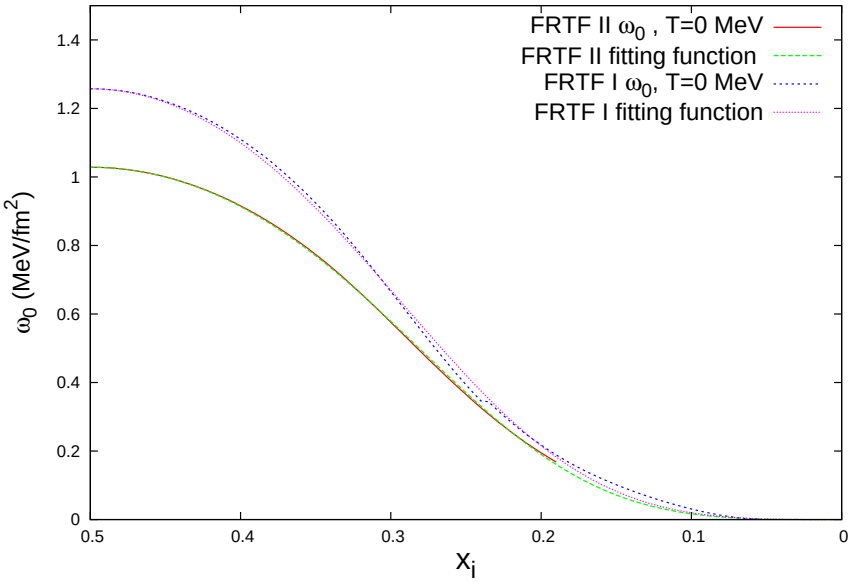

Figure 3.5: Surface tension at $T = 0$ MeV as a given proton fraction: Numerical result and analytic fitting function.

Chapter 4

Gaussian Type Finite Range model

† The finite range force can be managed with Gaussian distance ($f(r) \sim e^{-(r/r_0)^2}$) dependence. This distance dependence does not represent the repulsion when the distance between nucleons so close (< 0.1fm) but it can be justified since the total interaction energy is obtained from phase space integration. It also give a better representation of radii of nuclei and neutron skin than the Yukawa type finite range model.

4.1 Nuclear Density Functional Theory

4.1.1 Energy density functional

The energy of nuclear matter is given by

$$E = T_{kin} + E_{FR} + E_{ZR} + E_C + E_{S,L} \tag{4.1}$$

where T_{kin}, E_{FR}, E_{ZR}, E_C, and $E_{S,L}$ are the kinetic energy, nuclear finite-range interaction, zero-range interaction, Coulomb interaction, and spin-orbit coupling respectively. The kinetic energy contribution from nucleons is simply obtained by

$$T_{kin} = \int d^3r \sum_t \frac{\hbar^2}{2m}\tau_t \,, \tag{4.2}$$

where t is the type of nucleons.
In this Gaussian nuclear density functional (GNDF) theory, the number and kinetic densities are

$$\rho_t = \frac{1}{4\pi^3\hbar^3}\int_0^\infty f_t \, d^3p \,; \quad \tau_t = \frac{1}{4\pi^3\hbar^5}\int_0^\infty f_t p^2 \, d^3p \,, \tag{4.3}$$

where f_t is the Fermi-Dirac density function,

$$f_t = \frac{1}{1 + e^{(\epsilon_t - \mu_t)/T}} \,. \tag{4.4}$$

†This chapter is based on Y. Lim's work, arXiv:1101.1194. This work will be modified and resubmitted.

For the finite-range term, we use a Gaussian phenomenological model for the nuclear potential,

$$\begin{aligned} E_{FR} = & \sum_t \frac{1}{\pi^{3/2} r_0^3} \int d^3r_1 d^3r_2 e^{-r_{12}^2/r_0^2} \left[V_{1L} \rho_t(\boldsymbol{r}_1)\rho_t(\boldsymbol{r}_2) + V_{1U}\rho_t(\boldsymbol{r}_1)\rho_{t'}(\boldsymbol{r}_2) \right] \\ & + \sum_t \frac{1}{\pi^{3/2} r_0^3} \int d^3r_1 d^3r_2 e^{-r_{12}^2/r_0^2} \left[V_{2L} \rho_t^{1+\epsilon}(\boldsymbol{r}_1)\rho_t^{1+\epsilon}(\boldsymbol{r}_2) + V_{2U}\rho_t^{1+\epsilon}(\boldsymbol{r}_1)\rho_{t'}^{1+\epsilon}(\boldsymbol{r}_2) \right] \\ & + \sum_t \frac{1}{\pi^{3/2} r_0^3} \int d^3r_1 d^3r_2 e^{-r_{12}^2/r_0^2} \times \\ & \qquad \left[\int d^3p_{t1} d^3p_{t2} f_{t1} f_{t2} V_{3L} p_{12}^2 + \int d^3p_{t1} d^3p_{t'2} f_{t1} f_{t'2} V_{3U} p_{12}^2 \right], \end{aligned} \tag{4.5}$$

where $p_{12} = |\boldsymbol{p}_1 - \boldsymbol{p}_2|$, $r_{12} = |\boldsymbol{r}_1 - \boldsymbol{r}_2|$, r_0 is the length of interaction, and V_{1L}, V_{1U}, V_{2L}, V_{2U}, V_{3L}, and V_{3U} are interaction parameters to be determined. The last term is added to explain the effective mass of nucleons in dense matter.

The zero-range term in the nuclear force can be regarded as the energy contribution from three-body nuclear forces. The three-body force is quite important if the baryon density increases beyond two or three times the saturation density. One possible form of the three-body force is [34]

$$E_{ZR} = \frac{1}{4} t_3 \int d^3r \rho_n(r)\rho_p(r)\rho(r)\,, \tag{4.6}$$

where t_3 is the interaction strength for a three-body force, ρ_n (ρ_p) is neutron (proton) density, and the ρ is total density.

The energy functional for the Coulomb interaction has an exchange term which is absent in classical physics,

$$\begin{aligned} E_C &= E_C^{pp} + E_C^{ex} \\ &= \frac{e^2}{2} \int\int d^3r_1 d^3r_2 \frac{\rho_p(r_1)\rho_p(r_2)}{r_{12}} - \frac{3}{4\pi}(3\pi^2)^{1/3} e^2 \int d^3r \rho_p^{4/3}(r)\,. \end{aligned} \tag{4.7}$$

In bulk nuclear matter, the spin-orbit and Coulomb interactions constitute a small portion of the total energy, so we neglect these two terms. Then the bulk density functional would be

$$\begin{aligned} E_B &= T_{kin} + E_{FR} + E_{ZR} \\ &= \int d^3r \mathcal{E}_B(r)\,, \end{aligned} \tag{4.8}$$

where $\mathcal{E}_B$ is the energy density for bulk matter. Using Eq.(4.2), (4.5), and (4.6), we find

$$\begin{aligned}\mathcal{E}_B = &\frac{\hbar^2\tau_n}{2m} + \frac{\hbar^2\tau_p}{2m} \\ &+ V_{1L}(\rho_n\langle\rho_n\rangle + \rho_p\langle\rho_p\rangle) + V_{1U}(\rho_n\langle\rho_p\rangle + \rho_p\langle\rho_n\rangle) \\ &+ V_{2L}(\rho_n^{1+\epsilon}\langle\rho_n^{1+\epsilon}\rangle + \rho_p^{1+\epsilon}\langle\rho_p^{1+\epsilon}\rangle) + V_{2U}(\rho_n^{1+\epsilon}\langle\rho_p^{1+\epsilon}\rangle + \rho_p^{1+\epsilon}\langle\rho_n^{1+\epsilon}\rangle) \\ &+ V_{3L}(\rho_n\langle\tau_n\rangle + \tau_n\langle\rho_n\rangle + \rho_p\langle\tau_p\rangle + \tau_p\langle\rho_p\rangle) \\ &+ V_{3U}(\rho_n\langle\tau_p\rangle + \tau_n\langle\rho_p\rangle + \rho_p\langle\tau_n\rangle + \tau_p\langle\rho_n\rangle) \\ &+ \frac{1}{4}t_3\rho\rho_n\rho_p\end{aligned} \tag{4.9}$$

where we defined the Gaussian-type integral using '$\langle ... \rangle$':

$$\langle u(r_1)\rangle = \frac{1}{\pi^{3/2}r_0^3}\int d^3r_2 e^{-r_{12}^2/r_0^2}u(r_2)\,. \tag{4.10}$$

4.1.2 Effective mass, Potential, and Thermodynamic properties

The effective mass of the nucleons at the nuclear saturation density is about $0.7m_B$. Some nuclear density functionals use the effective mass $m^* = m_B$. However, we introduce the momentum dependent interaction which describes the effective mass of nucleons. The functional derivative δE_B gives us the effective masses and potentials in the nuclear density functional,

$$\delta E_B = \int d^3r\left(V_n\delta\rho_n + \frac{\hbar^2}{2m_n^*}\delta\tau_n + V_p\delta\rho_p + \frac{\hbar^2}{2m_p^*}\delta\tau_p\right). \tag{4.11}$$

Now we get the effective mass for neutrons and protons,

$$m_t^* = \frac{m}{1 + 4m(V_{3L}\langle\rho_t\rangle + V_{3U}\langle\rho_{t'}\rangle)/\hbar^2} \tag{4.12}$$

and the potentials

$$\begin{aligned}V_t = &2\Big[V_{1L}\langle\rho_t\rangle + V_{1U}\langle\rho_{t'}\rangle + (1+\epsilon)\rho_t^{\epsilon}(V_{2L}\langle\rho_t^{1+\epsilon}\rangle + V_{2U}\langle\rho_{t'}^{1+\epsilon}\rangle) \\ &+ V_{3L}\langle\tau_t\rangle + V_{3U}\langle\tau_{t'}\rangle\Big] + \frac{1}{4}t_3(2\rho_t + \rho_{t'})\rho_{t'}\,.\end{aligned} \tag{4.13}$$

The thermodynamic properties are extremely important to properly describe the hot dense matter. The degeneracy parameter, which is in the Fermi-Dirac distribution function is the key, to open the thermodynamic properties. Using the Fermi-integral, we get the baryon number density and kinetic density with degeneracy parameter $\phi_t = (\mu_t - V_t)/T$,

$$\rho_t = \frac{1}{2\pi^2}\left(\frac{2m_t^*T}{\hbar^2}\right)^{3/2}F_{1/2}(\phi_t), \quad \tau_t = \frac{1}{2\pi^2}\left(\frac{2m_t^*T}{\hbar^2}\right)^{5/2}F_{3/2}(\phi_t)\,. \tag{4.14}$$

Landau's quasi-particle formula gives us the entropy density S_t, which tell us how to find the pressure in this density functional,

$$S_t = -\frac{2}{\hbar^3}\int d^3p\big[f_t \ln f_t + (1-f_t)\ln(1-f_t)\big] = \frac{5\hbar^2}{6m_t^* T}\tau_t - \frac{\mu_t - V_t}{T}\rho_t\,. \tag{4.15}$$

From the thermodynamic identity and entropy density given above, we can get pressure,

$$\begin{aligned}
p &= \mu_n\rho_n + \mu_p\rho_p + TS_n + TS_p - \mathcal{E} \\
&= \sum_t\left(\frac{5\hbar^2}{6m_t^*}\tau_t + V_t\rho_t\right) - \mathcal{E} \\
&= \frac{\hbar^2\tau_n}{3m} + \frac{\hbar^2\tau_p}{3m} + V_{1L}(\rho_n\langle\rho_n\rangle + \rho_p\langle\rho_p\rangle) + V_{1U}(\rho_n\langle\rho_p\rangle + \rho_p\langle\rho_n\rangle) \\
&\quad + V_{2L}(1+2\epsilon)(\rho_n^{1+\epsilon}\langle\rho_n^{1+\epsilon}\rangle + \rho_p^{1+\epsilon}\langle\rho_p^{1+\epsilon}\rangle) \\
&\quad + V_{2U}(1+2\epsilon)(\rho_n^{1+\epsilon}\langle\rho_p^{1+\epsilon}\rangle + \rho_p^{1+\epsilon}\langle\rho_n^{1+\epsilon}\rangle) \\
&\quad + V_{3L}(\rho_n\langle\tau_n\rangle + \frac{7}{3}\tau_n\langle\rho_n\rangle + \rho_p\langle\tau_p\rangle + \frac{7}{3}\tau_p\langle\rho_p\rangle) \\
&\quad + V_{3U}(\rho_n\langle\tau_p\rangle + \frac{7}{3}\tau_n\langle\rho_p\rangle + \rho_p\langle\tau_n\rangle + \frac{7}{3}\tau_p\langle\rho_n\rangle) \\
&\quad + \frac{1}{2}t_3\rho\rho_n\rho_p\,.
\end{aligned} \tag{4.16}$$

At zero temperature non uniform matter, the chemical potential of the proton and neutron are given by,

$$\begin{aligned}
\mu_t &= \frac{\hbar^2}{2m_t^*}(3\pi^2\rho_t)^{2/3} + V_t \\
&= \frac{\hbar^2}{2m}(3\pi^2\rho_t)^{2/3} + 2(V_{3L}\langle\rho_t\rangle + V_{3U}\langle\rho_{t'}\rangle)(3\pi^2\rho_t)^{2/3} \\
&\quad + 2\Big[V_{1L}\langle\rho_t\rangle + V_{1U}\langle\rho_{t'}\rangle + (1+\epsilon)\rho_t^{\epsilon}(V_{2L}\langle\rho_t^{1+\epsilon}\rangle + V_{2U}\langle\rho_{t'}^{1+\epsilon}\rangle) + V_{3L}\langle\tau_t\rangle + V_{3U}\langle\tau_{t'}\rangle\Big] \\
&\quad + \frac{1}{4}t_3(2\rho_t + \rho_{t'})\rho_{t'}\,.
\end{aligned} \tag{4.17}$$

4.2 Parameters for the Gaussian nuclear density functional

Every nuclear model should reproduce five nuclear matter properties: binging energy, pressure, nuclear incompressibility, symmetry energy and effective mass, m^*. We use the saturation properties of nuclear matter to determine the parameters of the density functional. For zero-temperature uniform nuclear matter, we have the energy density as a function of

$u = \rho/\rho_0$ and $x = \rho_p/\rho$,

$$\begin{aligned}\frac{\mathcal{E}_B}{T_0\rho_0} &= \frac{3}{5}2^{2/3}u^{5/3}\big[(1-x)^{5/3}+x^{5/3}\big] + u^2\big[v_{1L}(x^2+(1-x)^2)+2v_{1U}x(1-x)\big] \\ &\quad + 2^{1+2\epsilon}u^{2+2\epsilon}\big[v_{2L}(x^{2+2\epsilon}+(1-x)^{2+2\epsilon})+2v_{2U}x^{1+\epsilon}(1-x)^{1+\epsilon}\big] \\ &\quad + 2^{2/3}u^{8/3}\big[v_{3L}(x^{8/3}+(1-x)^{8/3})+v_{3U}(x(1-x)^{5/3}+x^{5/3}(1-x))\big] \\ &\quad + \frac{1}{4}t_3'u^3x(1-x)\,,\end{aligned} \tag{4.18}$$

where we define the parameters

$$\begin{aligned}&T_0 = \frac{\hbar^2}{2m}(3\pi^2\rho_0/2)^{3/2}\,, \quad v_{1L,U} = \frac{\rho_0}{T_0}V_{1L,U}\,, \quad v_{2L,U} = \frac{1}{T_0}\Big(\frac{\rho_0}{2}\Big)^{1+2\epsilon}V_{2L,U} \\ &v_{3L,U} = \frac{4\cdot 3^{5/3}\pi^{4/3}}{5T_0}\Big(\frac{\rho_0}{2}\Big)^{5/3}V_{3L,U}\,, \quad t_3' = \frac{\rho_0^2}{T_0}t_3\,.\end{aligned} \tag{4.19}$$

Now we assume that the momentum-dependent interaction is blind to the type of nucleon, so $V_{3L} = V_{3U}(v_3 = v_{3L} + v_{3U})$. The binding energy of symmetric nuclear matter ($u = 1$, $x = 1/2$) is then given by

$$\frac{\mathcal{E}_0}{\rho_0} = -B_0 = T_0\left[\frac{3}{5} + \frac{v_{1L}+v_{1U}}{2} + v_{2L} + v_{2U} + \frac{v_3}{2} + \frac{t_3'}{16}\right], \tag{4.20}$$

where $B_0 = 16$MeV is the binding energy per baryon at the nuclear saturation density. The pressure at the saturation density vanishes, which means that the energy per baryon has its minimum at the saturation density,

$$p_0 = \rho_0 T_0\left[\frac{2}{5} + \frac{v_{1L}+v_{1U}}{2} + (1+2\epsilon)(v_{2L}+v_{2U}) + \frac{5}{6}v_3 + \frac{1}{8}t_3'\right] = 0\,. \tag{4.21}$$

The incompressibility parameter at the saturation density is given by

$$\begin{aligned}K_0 &= 9\frac{dp}{d\rho}\Big|_{\rho=\rho_0} \\ &= T_0\big[6 + 9(v_{1L}+v_{1U}) + 9(1+2\epsilon)(2+2\epsilon)(v_{2L}+v_{2U}) + 20v_3 + \frac{27}{8}t_3'\big] \\ &= 265\ \text{MeV}\,.\end{aligned} \tag{4.22}$$

The symmetry energy in nuclear matter is defined as

$$\begin{aligned} S_v &= \frac{1}{8}\frac{d^2(\mathcal{E}/\rho)}{dx^2}\bigg|_{\rho=\rho_0,x=1/2} \\ &= T_0\left[\frac{1}{3}+\frac{v_{1L}-v_{1U}}{2}+(1+\epsilon)((1+2\epsilon)v_{2L}-v_{2U})+\frac{5}{18}v_3-\frac{1}{16}t_3'\right] \\ &= 28\ \text{MeV}\,. \end{aligned} \tag{4.23}$$

Another parameter, which is related to symmetry energy, is given by

$$\begin{aligned} L &= \frac{3\rho_0}{8}\frac{d^3(\mathcal{E}/\rho)}{d\rho dx^2}\bigg|_{\rho=\rho_0,x=1/2} \\ &= T_0\left[\frac{2}{3}+\frac{3}{2}(v_{1L}-v_{1U})+3(1+2\epsilon)(1+\epsilon)((1+2\epsilon)v_{2L}-v_{2U})+\frac{25}{18}v_3-\frac{3}{8}t_3'\right] \\ &= 54\ \text{MeV}\,. \end{aligned} \tag{4.24}$$

We choose the effective mass at the saturation density as $0.78m_b$ and use this number in the Eq. (4.12),

$$m^* = \frac{m}{1+2m\rho_0 V_3/\hbar^2} = 0.78m_b\,. \tag{4.25}$$

Thus we can easily recover v_3 from Eq. (4.19). From Eqs. (4.20), (4.21), and (4.22), we can have $v_1 = v_{1L}+v_{2L}$, $v_2 = v_{2L}+v_{2U}$ and t_3' :

$$\begin{aligned} v_1 &= \frac{5K_0/T_0+5v_3(1-3\epsilon)-72\epsilon-90B_0/T_0(1+2\epsilon)-12}{45\epsilon} \\ v_2 &= \frac{12+90B_0/T_0-5K_0/T_0-5v_3}{90\epsilon(1-2\epsilon)} \\ t_3' &= -8v_1-16v_2-8v_3-\frac{16B_0}{T_0}-\frac{48}{5}\,. \end{aligned} \tag{4.26}$$

Then we can manipulate Eq. (4.23), and (4.24) to get v_{1L} and v_{2L},

$$\begin{aligned} v_{1L} &= \frac{1}{2}v_1+\frac{1}{2\epsilon}\left[\frac{5(1-3\epsilon)}{27}v_3+\frac{2\epsilon-1}{16}t_3'+\frac{(1+2\epsilon)S_v}{T_0}-\frac{L}{3T_0}-\frac{1+6\epsilon}{9}\right] \\ v_{2L} &= \frac{1}{2(1+\epsilon)}v_2-\frac{1}{4\epsilon(1+\epsilon)^2}\left[\frac{5}{27}v_3-\frac{t_3'}{16}+\frac{S_v}{T_0}-\frac{L}{3T_0}-\frac{1}{9}\right], \end{aligned} \tag{4.27}$$

and we can have $v_{1U} = v_1 - v_{1L}$ and $v_{2U} = v_2 - v_{2L}$.

Table 4.1: Interaction parameters when $\epsilon = 1/6$, $K = 265$ MeV, $S_v = 28$MeV, $L = 54$MeV.

v_{1L}	v_{1U}	v_{2L}	v_{2U}	$v_{3L,U}$	t_3'	r_0 (fm)
-1.766	-3.472	0.410	0.931	0.169	1.177	1.205

4.2.1 Determination of the $1+\epsilon$ power

We added in Eq. (4.5) the auxiliary density interaction with the $1+\epsilon$ power. We might regard $1+\epsilon$ as the many-body effect—for example, a three-body force if $\epsilon > \frac{1}{2}$. It is known, however, that interactions among more than three-bodies are unimportant in dense matter [34]. Thus we can restrict the ϵ to be less than $\frac{1}{2}$. As ϵ changes, the t_3 parameter changes sign, which means that the three-body force can be attractive or repulsive. In the general Skyrme model with the three-body force, the t_3 parameter is positive. We choose $\epsilon = 1/6$ so that the interaction has the form of $\rho_{t_1}^{7/6}\rho_{t_2}^{7/6}$. In zero-temperature, uniform matter, we have $u^{7/3}$ terms in the energy density. From Eq. (4.18), the energy density has $u^{5/3}$, u^2, $u^{7/3}$, $u^{8/3}$, and u^3 terms if we have $\epsilon = 1/6$ so we can use a statistical approach in uniform matter. Fig 4.1 shows the energy per baryon from GNDF and APR [35] EOS. We can see that as the density increases, the pressure from the two models agrees very well.

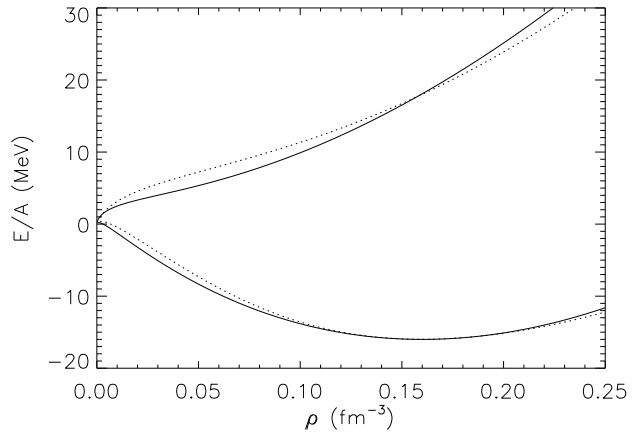

Figure 4.1: The solid line represents the energy per baryon (uniform matter) using GNDF. The upper (lower) curve represents the energy per baryon of pure neutron matter (symmetric nuclear matter). The energy per baryon (dotted line) from the APR [35] EOS is added for comparison.

4.2.2 The effective range of the nuclear force : r_0

In the Gaussian-interaction model, we can see that the effective range of the force is given by r_0, which is approximately $\sim$ 1 to 2 fm. We do not have an analytic form of r_0, so we

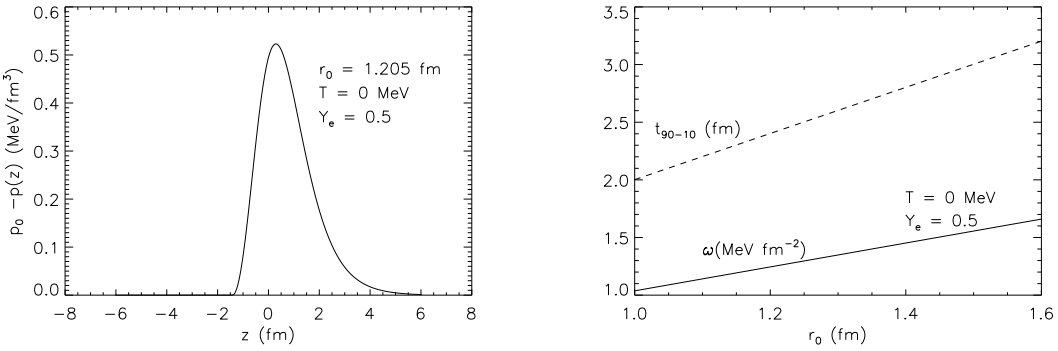

Figure 4.2: The left figure shows the quantity $p_0 - p(z)$ at the semi-infinite nuclear surface when $r_0 = 1.205$ fm and $Y_e = 0.5$. The surface tension from this configuration is $\omega = 1.250$ MeV fm^{-2}. The right figure shows the surface tension (solid line) and t_{90-10} thickness (dashed line) as a function of r_0. When $r_0 = 1.205$, $t_{90-10} = 2.412$ fm. The surface tension and t_{90-10} thickness are both linear functions of r_0.

need to rely on the numerical solution of the surface tension of semi-infinite nuclear matter:

$$\omega = \int_{-\infty}^{\infty} \big[\mathcal{E} - TS_n - TS_p - \mu_n\rho_n - \mu_p\rho_p + p_0\big]dz = -\int_{-\infty}^{\infty} \big[p(z) - p_0\big]dz\,, \tag{4.28}$$

where p_0 is the pressure at $z = -\infty$ or $z = +\infty$. In one-dimensional, semi-infinite nuclear matter, we assume that the nuclear density depends only on the z-axis. The Gaussian integral then becomes

$$\frac{1}{\pi^{3/2}r_0^3}\int d^3r\, u(r) = \frac{1}{\pi^{1/2}r_0}\int_{-\infty}^{+\infty} dz\, u(z)\,. \tag{4.29}$$

Experimental values for the surface tension and surface thickness are $\omega = 1.250$ MeV fm^{-2} and $t_{90-10} = 2.3$ fm. Fig. 4.2 shows the numerical calculation, which says that $r_0 = 1.205$ fm from the surface tension and $r_0 = 1.149$ from t_{90-10} thickness. There is a 5% discrepancy between the two results. Table 4.1 shows the interaction parameters which we use in this paper when $K = 265$ MeV, $S_v = 28$ MeV, $L = 54$ MeV, and $\epsilon = 1/6$. The simple density dependent interactions ($v_{1L,U}$) are attractive. On the other hand, the auxiliary density dependent interactions ($v_{2L,U}$), momentum dependent interactions ($v_{3L,U}$) three-body force (t_3) are repulsive in our model.

4.3 Nuclear matter and nuclei

4.3.1 Specific heat

The specific heat of uniform nuclear matter can be obtained by

$$C_V = T\frac{\partial S}{\partial T}\bigg|_\rho = \frac{\partial E}{\partial T}\bigg|_\rho . \tag{4.30}$$

For a non-interacting Fermi gas, the specific heat increases linearly with temperature. When the temperature is low enough, we expect that the specific heat of the nuclear matter tends to behave like a free Fermi gas. The specific heat formula for the degenerate gas is given by [36]

$$C_V = \frac{1}{3}m^* k_F k_B^2 T\,, \tag{4.31}$$

where m^* is the effective mass of a nucleon, k_F is the Fermi momentum, and k_B is the Boltzman constant.

However, as the temperature increases, non-linear behavior of the specific heat becomes apparent so that the degenerate gas formula is no longer valid, due to the excitation of nucleons deep inside the Fermi surface.

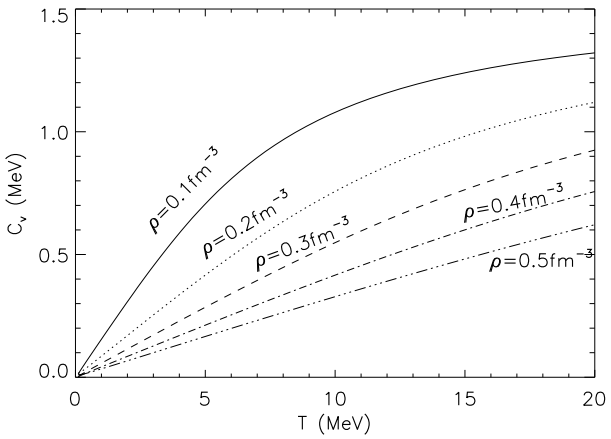

Figure 4.3: This figure shows the specific heat per nucleon of uniform matter for different densities. If the temperature is low enough, the specific heat behaves linearly with temperature.

To calculate the specific heat of uniform nuclear matter, we use the Johns, Ellis, and Lattimer (JEL) method [12], which enables us to get the pressure, energy density and entropy density for a given degeneracy parameter. Fig. 4.3 shows the specific heat per nucleon of uniform nuclear matter. It shows the linear relation between the specfic heat and temperature at low temperature region as in Eq. (4.31).

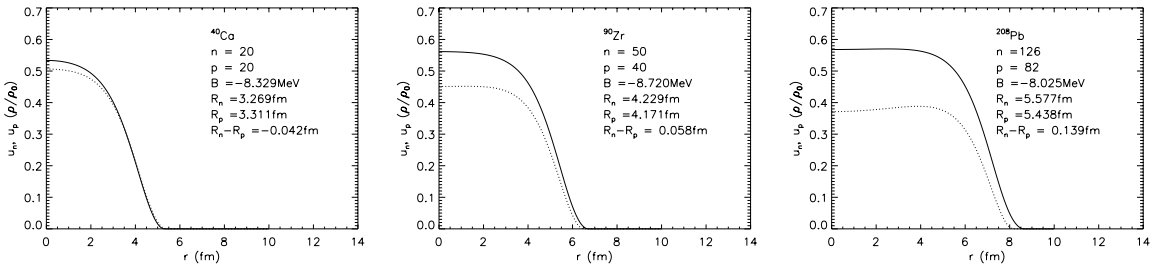

Figure 4.4: This figure shows the basic properties of the closed-shell nuclei which can be obtained from the GNDF. The solid (dotted) line indicates the neutron (proton) density as a function of radius. As the number of nucelons in the nuclei increase, the neutron skin thickness ($R_n - R_p$) increases.

A detailed calculation of the specific heat at sub-nuclear density in the neutron star needs to take into account the beta-equilibrium condition and heavy nuclei with a neutron gas. The specific heat plays an important role in the cooling process of neutron stars. In the neutron star crust, there are heavy nuclei and a free-neutron gas. The effective masses of protons and neutrons are different from the center of the heavy nuclei and dilute neutron gas, so we cannot use Eq. (4.31). In this case the specific heat at the neutron star crust can be calculated numerically by changing temperature and comparing the total energy change.

4.3.2 Nuclei at $T = 0$ MeV

We can use the GNDF theory and the Lagrange multiplier method to find the radius and binding energy per nucleon for a single nucleus using the Winger-Seitz cell method. In the Lagrange multiplier method, the chemical potentials of protons and neutrons are constant in the Wigner-Seitz cell to minimize the total free energy. Fig. 4.4 shows the radius and binding energy of the closed-shell nuclei obtained using this method. These results agree well with the experiment [32]. ^{40}Ca has a larger charge radius than the neutron radius because of the Coulomb repulsion between protons. The solid (dotted) line denotes the neutron (proton) density. As the atomic number increases, the central density of neutrons increases; on the other hand the central density of protons decreases. The difference between charge and neutron radii increases and the neutron skin becomes thicker as the atomic number increases. In ^{208}Pb nuclei, the central density of protons is lower than the proton density of the outer part of nuclei ($r = 4 - 5$ fm) because of proton Coulomb repulsion.

Table 4.2 shows the proton and neutron radii and binding energy per baryon of closed shell nuclei from various nuclear models. The calculation from GNDF theory agrees well with experimental results.

4.3.3 Heavy nuclei in the neutron star crust

In the neutron star crust, heavy nuclei are formed with a free-neutron gas. These heavy nuclei are suspected to form a body centered cubic (BCC) structure. In the static equilibrium state, we calculate the density profile of heavy nuclei with a neutron gas using the Wigner-Seitz

Table 4.2: Comparsion of the results from Steiner (Potential & Field Theoretical) et al.[32] , FRTF I(truncated), FRTF II(modified) and the GNDF

Nucleus	Property	Experiment	Potential	FT	FRTF I	FRTF II	GNDF
^{208}Pb	r_{ch} (fm)	5.50	5.41	5.41	5.38	5.45	5.44
	BE/A(MeV)	7.87	7.87	7.77	8.01	8.17	8.02
	δR(fm)	0.12 ± 0.05	0.19	0.20	0.15	0.13	0.14
		0.20 ± 0.04					
^{90}Zr	r_{ch} (fm)	4.27	4.18	4.17	4.10	4.15	4.17
	BE/A(MeV)	8.71	8.88	8.65	8.77	9.00	8.72
	δR(fm)	0.09 ± 0.07	0.075	0.093	0.064	0.054	0.057
^{40}Ca	r_{ch} (fm)	3.48	3.40	3.34	3.22	3.26	3.31
	BE/A(MeV)	8.45	8.89	8.61	8.47	8.77	8.33
	δR(fm)	-0.06 ± 0.05	-0.044	-0.046	-0.036	-0.039	-0.042
		-0.05 ± 0.04					

Cell method. The plot on the left side of Fig. 4.5 shows the proton (dotted line) and neutron density (solid line) profiles from the center (r=0 fm) of heavy nuclei when $\rho = 0.01\text{fm}^{-3}$. There are dripped neutrons outside of the heavy nuclei. The cell size (Rc), which is a rough estimate of the distance between neighboring heavy nuclei, is determined by nuclear density and beta equilibrium conditions ($\mu_n = \mu_p + \mu_e$). There is a wave function overlap at the boundary of the Wigner-Seitz cell. The actual distance between heavy nuclei is $(8\pi/3)^{1/3}$Rc. The right side of Fig. 4.5 shows the binding energy per baryon as a function of Wigner-Seitz cell size. As the density decreases, the cell size increases and the energy per baryon converges to -8.0 MeV.

Table 4.3: Nuclear properties in the neutron star crust

ρ (fm^3)	p (MeV/fm^3)	ϵ (MeV/fm^3)	N_{nuc}	Z	Rc (fm)
5.623×10^{-2}	0.181	53.06	271.6	89.51	25.12
5.012×10^{-2}	0.147	47.27	218.0	32.18	18.70
3.981×10^{-2}	9.332×10^{-2}	37.52	137.8	21.69	18.06
2.512×10^{-2}	3.965×10^{-2}	23.65	145.3	27.93	22.77
1.585×10^{-2}	1.976×10^{-2}	14.91	150.7	32.07	26.36
1×10^{-2}	1.081×10^{-2}	9.405	147.7	34.29	29.15
1×10^{-3}	7.988×10^{-4}	9.383×10^{-1}	116.3	38.50	40.71
1×10^{-4}	6.945×10^{-5}	9.352×10^{-2}	79.23	38.31	65.47
1×10^{-5}	1.480×10^{-6}	9.326×10^{-3}	58.02	36.98	131.4
1×10^{-6}	2.362×10^{-9}	9.311×10^{-4}	47.90	35.14	270.6
1×10^{-7}	1.714×10^{-9}	9.303×10^{-5}	43.37	34.10	569.7

Table 4.3 shows the thermodynamic properties and physical dimensions of nuclei in the neutron star crust. N_{nuc} and Z are the number of neutrons and protons of heavy nuclei in the Wigner-Seitz Cell respectively. The atomic number of heavy nuclei remains Z $\sim$ 35 for

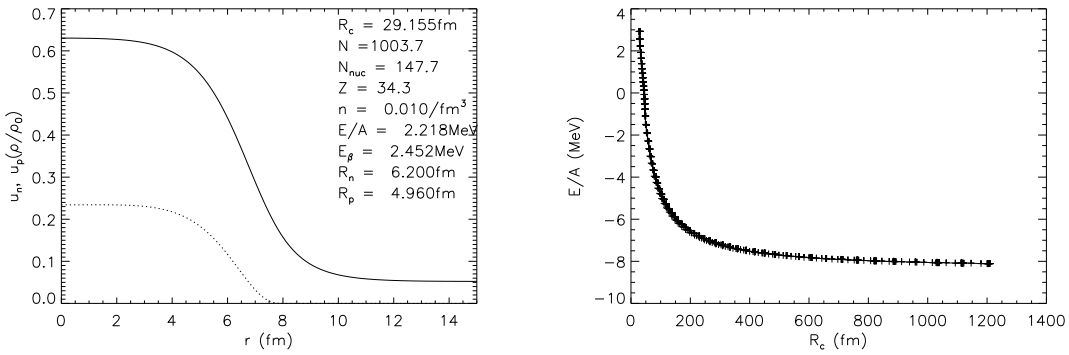

Figure 4.5: In a neutron star, heavy nuclei exist. The left figure shows the density profile of proton (dotted line) and neutron (solid line). $r = 0$ fm means the center of heavy nuclei. Outside the heavy nuclei, there are dripped neutrons. As density decreases, the cell size increases and the energy per baryon converges to -8.0 MeV.

a large range of densities before the phase transition to uniform matter. This means that the proton fraction decreases as the density increases. For a narrow range of densities, the atomic number suddenly increases and the heavy nuclei merge with free neutrons to form uniform nuclear matter.

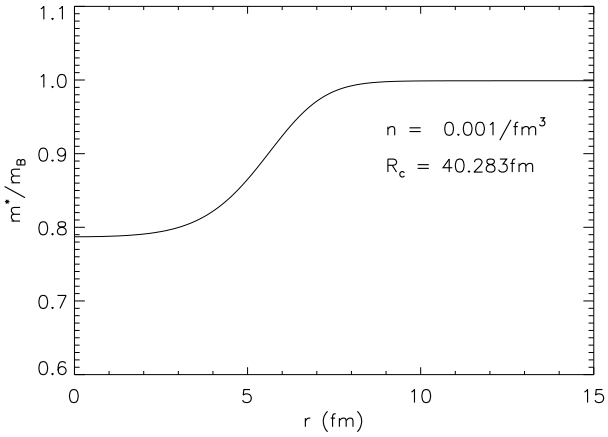

Figure 4.6: Effective mass of nucleons in the Wigner-Seitz cell as a function of radial distance from the center of heavy nuclei. Since the nuclear interaction is weak at the boundary of the cell, the effective mass of nucleon and the pure mass of a nucleon become equal.

Fig. 4.6 shows the effective mass of nucleons in the Wigner-Seitz cell. The effective mass of nucleons in the Wigner-Seitz cell is given by Eq. (4.12) and Eq. (4.19) combining to give,

$$m_t^* = \frac{m}{1 + \frac{5}{3}\left(v_{3L}\frac{\tilde{\rho_t}}{\rho_0} + v_{3U}\frac{\tilde{\rho_{t'}}}{\rho_0}\right)}\,. \tag{4.32}$$

Since we assume that the momentum interaction is blind with respect to isospin, the effective mass is identical for different isospin nucleons. The effective mass to pure mass ratio of nucleons is 0.78 at the center of the heavy nuclei and becomes 1 at the outer region of the Wigner-Seitz cells since the density of nuclear matter is low at the outside of the heavy nuclei, the interaction energy of nuclear matter is weak.

4.4 Phase transition

In the neutron star, we can see two types of phase transitions: one is the phase transition from nuclei with a neutron gas to uniform matter, and the other is the phase transition from uniform nuclear matter to quark matter. During the first phase transition, we can see the nuclear pasta phase [41] [†]. That is, spherical nuclei become ellipsoidal, then cylindrical, and finally slab phase before nuclear matter becomes uniform matter. However, the energy difference is quite small, so that the effects on the large scale physics are negligible. On the other hand, the second phase transition is quite dramatic. The energy and pressure change significantly from nuclear matter to quark matter.

4.4.1 Uniform matter

To check the phase transition points from heavy nuclei with a neutron gas to uniform nuclear matter, we can simply compare the energy per baryon of uniform nuclear matter with the energy per baryon of nuclei with a neutron gas since the nuclear matter exists in the lowest energy states. The energy per baryon in uniform matter can be easily obtained by changing the '$\langle \dots \rangle$' integrals to non integral form from Eq. (4.11) since the Gaussian integrations in uniform matter become unity. Typically there is a phase transition around $0.5\rho_0$.

We know that in the outer crust of the neutron star the nuclei have a BCC structure. If we assume that the pasta phase exists in the low-density region, we may use the density perturbation to see the phase transition from nuclei with a neutron gas to uniform nuclear matter. We use the wave number perturbation to see the energy exchange, which has contributions from the volume effects, gradient effects, and Coulomb energy can be approximated [20],

$$v(q) \simeq v_0 + \beta q^2 + \frac{4\pi e^2}{q^2 + k_{TF}^2}\,, \tag{4.33}$$

where q is the sinusoidal variation of the wave number in the spatially periodic density perturbation. The volume term is given by

$$v_0 = \frac{\partial \mu_p}{\partial \rho_p} - \frac{(\partial \mu_p/\partial \rho_n)^2}{(\partial \mu_n/\partial \rho_n)}\,. \tag{4.34}$$

[†]Around $1/2\rho_0$, spherical nuclei is deformed to be oblate nuclei, cylindrical phase, slab, cylindrical hole, and bubble phase to minimize the total free energy density. Since its shape resembles Italian pasta, it is called 'nuclear pasta' phase.

The energy exchange from the gradient has the form

$$\beta = D_{pp} + 2D_{np}\xi + D_{nn}\xi^2\,, \quad \xi = -\frac{\partial\mu_p/\partial\rho_n}{\partial\mu_n/\partial\rho_n} \tag{4.35}$$

where the coefficients of the gradient terms are given by $D_{pp} = D_{np} = D_{nn} = 132\text{MeV}\cdot\text{fm}^5$ [18]. The k_{TF} in the Coulomb interaction represents the inverse Thomas-Fermi screening length of the electrons. When we see the change in the sign of v, the uniform matter phase is more stable than the periodic structure of the nuclei. The v has a minimum at

$$v_{min} = v_0 + 2(4\pi e^2\beta)^{1/2} - \beta k_{TF}^2\,, \tag{4.36}$$

when $q_{min}^2 = (4\pi e^2/\beta)^{1/2} - k_{TF}^2$.

Another way to see the phase transition is to use the thermodynamic instability. The thermodynamic stability condition can be described using the inequalities [18, 19],

$$\begin{aligned} -\left(\frac{\partial P}{\partial v}\right)_\mu &> 0, \\ -\left(\frac{\partial \mu}{\partial q_c}\right)_v &> 0. \end{aligned} \tag{4.37}$$

where $P = P_b + P_e$ is the total pressure from electrons and baryons and $\mu = \mu_n - \mu_p$ is the difference between the neutron and proton chemical potentials, which is the electron chemical potential in beta-stable matter. q_c is defined as $q_c = x_p - \rho_e/\rho$. Mathematically, the inequalities in Eq. (4.37) show that the energy per baryon is convex. Eq. (4.37) can be verified to be [18, 19]

$$\begin{aligned} -\left(\frac{\partial P}{\partial v}\right)_\mu &= \rho^2\left[2\rho\frac{\partial E(\rho,x_p)}{\partial\rho} + \rho^2\frac{\partial^2 E(\rho,x_p)}{\partial\rho^2} - \left(\frac{\partial^2 E(\rho,x_p)}{\partial\rho\partial x_p}\rho\right)^2 \Big/ \frac{\partial^2 E(\rho,x_p)}{\partial x_p^2}\right] > 0, \\ -\left(\frac{\partial \mu}{\partial q_c}\right)_v &= \left(\frac{\partial^2 E(\rho,x_p)}{\partial x_p^2}\right)^{-1} + \frac{\mu_e^2}{\pi^2\hbar^3\rho} > 0\,. \end{aligned} \tag{4.38}$$

The second of Eq. (4.38) always holds, so the first will determine the phase transition in the neutron star crust. Xu et al.[18], use a simple equation to determine the instability using the thermodynamic relation,

$$\frac{2}{\rho}\frac{\partial E}{\partial\rho}\frac{\partial^2 E}{\partial x_p^2} + \frac{\partial^2 E}{\partial\rho^2}\frac{\partial^2 E}{\partial x_p^2} - \left(\frac{\partial^2 E}{\partial\rho\partial x_p}\right)^2 = \frac{\partial\mu_n}{\partial\rho_n}\frac{\partial\mu_p}{\partial\rho_p} - \left(\frac{\partial\mu_n}{\partial\rho_p}\right)^2. \tag{4.39}$$

Eq. (4.39) is equivalent to the volume part of the thermodynamic perturbation Eq. (4.34) method except that there is a $\partial\mu_n/\partial\rho_n$ difference. Comparing the two methods (pertubation and thermodynamic instability) shows the effects of the gradient and Coulomb terms in the perturbation method on the transition densities. Fig. 4.7 shows transition densities using

the perturbation method and thermodynamic instability. The perturbation method has a lower transition density ($0.355\rho_0$) than thermodynamic instability method ($0.406\rho_0$).

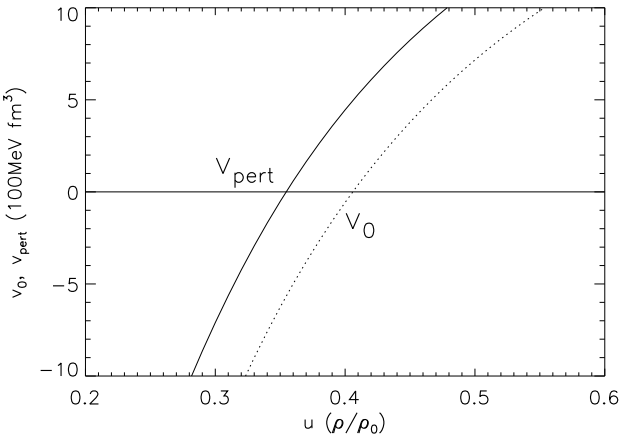

Figure 4.7: We can see the transition density from nuclei with a neutron gas to nuclear matter. The solid line denotes the curve from the perturbation method. The dotted line corresponds to the thermodynamic instability method, equivalent to v_0 in the perturbation method. The solid line has a transition density of $0.355\rho_0$ and the dotted line has a transition density of $0.406\rho_0$.

4.4.2 Quark matter

In this model, we do not consider the appearance of hyperons [37] since it is not clear how the hyperons and nucleons interact. Thus we simply consider the phase transition from uniform matter to quark matter. We use the MIT bag model [37] for the quark matter equation of state. At T=0 MeV, the pressure and energy density are given by [37]

$$\begin{aligned} p &= -B + \sum_f \frac{1}{4\pi^2(\hbar c)^3}\left[\mu_f(\mu_f^2 - m_f^2c^4)^{1/2}(\mu_f^2 - \frac{5}{2}m_f^2c^4)\right. \\ &\qquad \left. + \frac{3}{2}m_f^4c^8\ln\left(\frac{\mu_f + (\mu_f^2 - m_f^2c^4)^{1/2}}{m_fc^2}\right)\right] \\ \epsilon &= B + \sum_f \frac{3}{4\pi^2(\hbar c)^3}\left[\mu_f(\mu_f^2 - m_f^2c^4)^{1/2}(\mu_f^2 - \frac{5}{2}m_f^2c^4)\right. \\ &\qquad \left. - \frac{1}{2}m_f^4c^8\ln\left(\frac{\mu_f + (\mu_f^2 - m_f^2c^4)^{1/2}}{m_fc^2}\right)\right], \end{aligned} \tag{4.40}$$

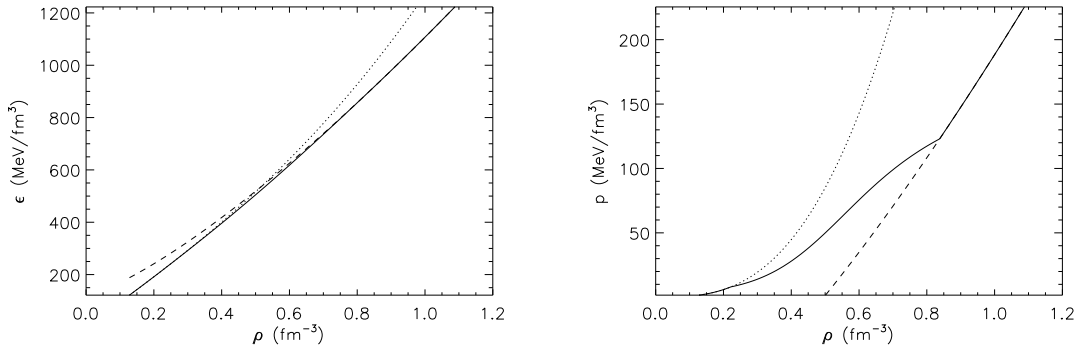

Figure 4.8: The left panel shows the energy density of nuclear matter (dotted line), quark matter (dashed) and mixed phase (solid). The right panel shows the pressure of nuclear matter (dotted lined), quark matter (dashed) and mixed phase (solid).

where the density for each quark flavor is given by

$$\rho_f = \frac{(\mu_f^2 - m_f^2)^{3/2}}{\pi^2(\hbar c)^3}\,. \tag{4.41}$$

For the pure-quark phase we use $m_u = m_d = 0$, $m_s = 150$ MeV and $B = 100$ MeV fm^{-3}[†]. In the mixed phase of uniform nuclear matter and quark matter, we apply Gibb's conditions to minimize the free-energy density with two constraints, which are related to total number density and charge neutrality,

$$\begin{aligned} \rho_b &= \chi\rho_N + (1-\chi)\rho_Q \\ Q &= \chi Q_N + (1-\chi)Q_Q = 0\,, \end{aligned} \tag{4.42}$$

where χ is the volume fraction of the uniform nuclear matter in the mixed phase and the subscript N (Q) represents nuclear (quark) matter. In the mixed phase, the total charge is globally neutral in contrast to pure nuclear matter and quark matter. From minimizing the free energy, we have

$$\begin{aligned} p_N &= p_Q \\ \mu_n &= \mu_u + 2\mu_d \\ \mu_p &= 2\mu_u + \mu_d\,, \end{aligned} \tag{4.43}$$

then we have the energy density of the mixed phase

$$\epsilon = \chi\epsilon_N + (1-\chi)\epsilon_Q\,. \tag{4.44}$$

[†]Here B is the bag constant for the MIT bag model not the binding energy per baryon for nuclear matter.

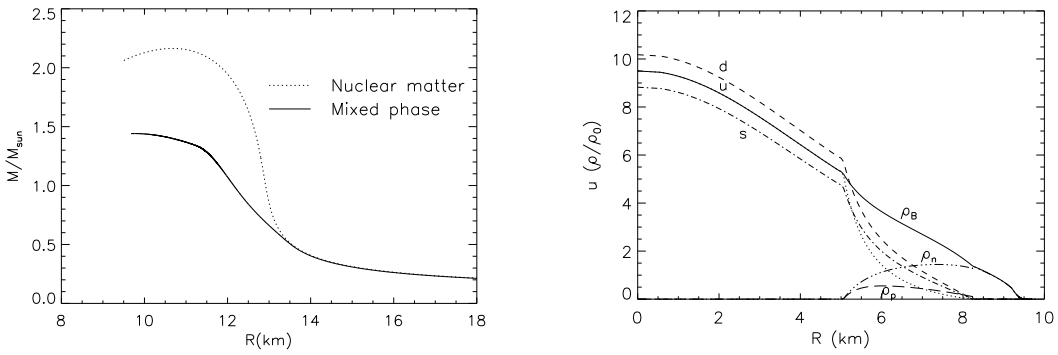

Figure 4.9: The left panel shows the mass-radius relation of the neutron stars (dotted line) from the GNDF and the hybrid stars (solid line). The right panel shows the number density profile of a hybrid star which have M= 1.44M$_\odot$. At $r \sim 5.0$ km, the phase transition to nuclear matter takes place, and protons and neutrons exit. When r=8.2 km, the phase transition to nuclear matter is completed and there is no more quark matter.

As in the case of uniform matter, we assume beta-stable matter so that the chemical potentials of the nuclear matter and quark matter have the relation

$$\begin{aligned} \mu_n &= \mu_p + \mu_e \\ \mu_d &= \mu_s = \mu_u + \mu_e \,. \end{aligned} \tag{4.45}$$

Fig. 4.8 shows the energy density and pressure as a function of number density. The dotted (dashed) line represents nuclear (quark) matter. The solid line denotes the mixed phase. The phase transition begins when the baryon density becomes $1.386\rho_0$ and all nucleons turn into quark matter when the baryon density becomes $5.236\rho_0$.
If there is a phase transition in the core of a cold neutron star, the mass and radius are quite different from the case of a pure-nuclear-matter neutron star. The left panel of Fig. 4.9 shows the mass-radius relation of the neutron stars (dotted line) and hybrid stars (solid line). The right panel shows the number density profiles of a quark matter and nuclear matter of 1.44M$_\odot$ hybrid star. The maximum mass of a cold neutron star with mixed phase (hybrid star) is 1.441M$_\odot$ and the central density of the neutron star is $9.585\rho_0$. The mass and radius curve with the mixed phase indicates where the mixed phase exists. As the distance from the center of the hybrid star increases, the phase transition to nuclear matter takes place so that neutrons and protons appear ($r \sim 5.0$km). Far from the center, the phase transition is completed ($r = 8.2$km); pure nuclear matter exists only for larger radii. The existence of quark matter in the hybrid star can be explained by angular momentum loss of the proto-neutron star. That is, a fast-rotating neutron stars loses angular momentum because of magnetic dipole radiation; the central density of the neutron star increases due to the decrease in centripetal force, then quark matter appears. Since quark matter has a lower energy density than pure nuclear matter, we might expect heating of the neutron star from latent heat from quark matter.

4.5 Astrophysical application

4.5.1 Mass-radius relation of a cold neutron star

We know that the typical radius of a neutron star is ~ 10km and the mass is $\sim 1.4M_{\odot}$. In this system, the degeneracy pressure of the neutrons provides support against gravitational collapse. We can apply our model to calculate the mass and radius of neutron stars for a given central density. We use the Tolman-Oppenheimer-Volkov (TOV) equations which describe general relativistic hydrostatic equilibrium:

$$\begin{aligned} \frac{dp}{dr} &= -\frac{G(M(r)+4\pi r^3 p/c^2)(\epsilon+p)}{r(r-2GM(r)/c^2)c^2} \\ \frac{dM}{dr} &= 4\pi\frac{\epsilon}{c^2}r^2\,. \end{aligned} \tag{4.46}$$

Fig. 4.10 shows the mass-radius relation for a cold neutron star. In the GNDF model, the maximum mass of a cold neutron star is $2.163\mathrm{M}_{\odot}$, and the corresponding radius is 10.673km. The maximum mass from the GNDF model is in between the FRTF truncated model (FRTF I) and the modified model of the FRTF (FRTF II)

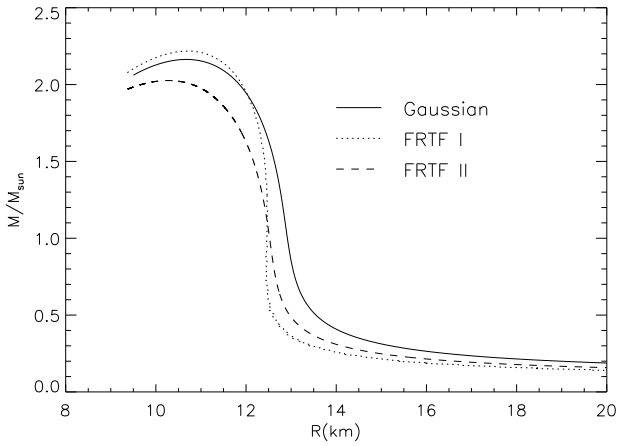

Figure 4.10: Mass-radius relation for a cold neutron star. The mass of a cold neutron star from the Gaussian density functional model has a maximum mass of $(2.163M_{\odot})$ when the central density is $6.74\rho_0$.

4.5.2 Moment of inertia of the neutron star

In the slow-motion approximation, the moment of inertia is given by [39]

$$I = \frac{8\pi}{3}\int_0^R r^4(\rho+p)e^{(\lambda-\nu)/2}\omega\,dr\,, \tag{4.47}$$

where $\lambda = -\ln(1-2m/r)$ and ν are the metric coefficients and ω is the rotational drag function. In terms of the function $j = e^{-(\lambda+\nu)/2}$, the rotational drag satisfies

$$\frac{d}{dr}\left(r^4 j \frac{d\omega}{dr}\right) = -4r^3\omega\frac{dj}{dr}\,, \tag{4.48}$$

with the boundary conditions

$$\omega_R = 1 - \frac{2I}{R^3}\,, \qquad \left(\frac{d\omega}{dr}\right)_0 = 0\,. \tag{4.49}$$

Therefore, the moment of inertia can be written as

$$I = -\frac{2}{3}\int_0^R r^3\omega\frac{dj}{dr}dr = \frac{1}{6}\int_0^R d\left(r^4\omega\frac{dj}{dr}\right) = \frac{R^4}{6}\frac{d\omega}{dr}\bigg|_R\,. \tag{4.50}$$

We note that the second-order differential equation that ω satisfies, Eq. (4.48), can be instead written as a first order differential equation in terms of the function $\phi = d\ln\omega/d\ln r$,

$$\frac{d\phi}{dr} = -\frac{\phi}{r}(\phi+3) - (4+\phi)\frac{d\ln j}{dr}\,, \tag{4.51}$$

where

$$\frac{d\ln j}{dr} = -\frac{4\pi r^2}{r-2m}(\rho+p)\,, \tag{4.52}$$

with the boundary condition $\phi(0) = 0$. The moment of inertia becomes

$$I = \frac{R^3}{6}\phi_R\omega_R = \frac{\phi_R}{6}(R^3 - 2I)\,, \tag{4.53}$$

using the boundary condition for ω. This simplifies to

$$I = \frac{R^3\phi_R}{6+2\phi_R}\,. \tag{4.54}$$

Lattimer and Schutz proposed an empirical approximation for the moment of inertia [43],

$$I \simeq (0.237 \pm 0.008)MR^2\left[1 + 4.2\frac{M\mathrm{km}}{\mathrm{M}_\odot R} + 90\left(\frac{M\mathrm{km}}{\mathrm{M}_\odot R}\right)\right]. \tag{4.55}$$

Fig. 4.11 shows the moment of inertia of a cold neutron star. The color band represents upper and lower boundaries of the empirical approximation. FRTF I, II and GNDF agree quite well with this empirical approximation.

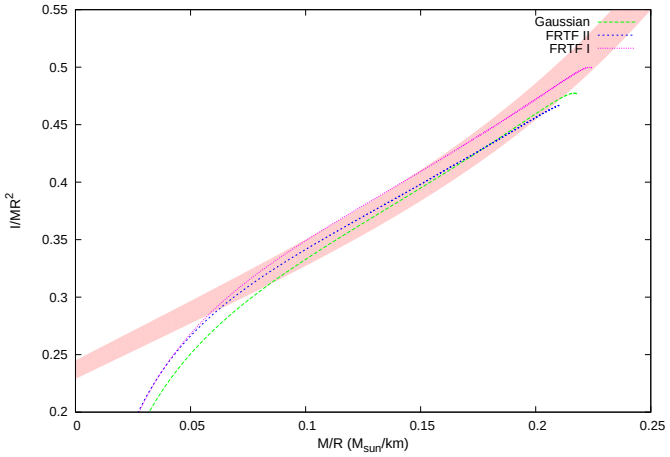

Figure 4.11: Moment of inertia of a cold neutron star. The color band represents the upper and lower boundaries of the empirical approximation eq (4.55). Three different models show different curves; however, they represent the empirical results quite well.

4.6 Conclusions

In the GNDF model, the total energy consists of the kinetic energy, the finite-range effect, the zero-range effect, and the Coulomb energy. Using the Lagrange multiplier method, we find the potential energy, pressure, chemical potential and thermodynamic properties. The interaction parameters are obtained from the properties of infinite nuclear matter. We are able to obtain the charge radius and binding energy per baryon of the closed-shell nuclei. The Wigner-Seitz cell size increases as the density decreases and the binding energy per baryon approaches -8.0MeV. The effective mass becomes $0.78m_B$ at the center of the heavy nuclei and becomes m outside of heavy nuclei. We are also able to find the pressure of uniform symmetric nuclear matter and neutron matter. For finite temperature, we can see the specific heat of nuclear matter follows the general trend of the free fermions. Thus the GNDF model is a good nuclear matter model to study for both low and high nuclear densities. We can improve the current model if we have more exact experimental results and we add additional interaction terms to explain the experimental results. The phase transition was studied using the GNDF model. The density perturbation suggested that the phase transition from non-uniform nuclear matter to uniform matter takes place at densities less than $0.5\rho_0$. When we take into account the phase transition from uniform nuclear matter to quark matter, we see that there is a drastic change in the maximum mass of a neutron star, since the pressure and energy density of quark matter are significantly different from nuclear matter. The maximum mass of the hybrid star is less than $1.5\mathrm{M}_\odot$. Since the bag constant is fixed in this study, we need to investigate the mass of hybrid star by varying the bag constant.

Chapter 5

Nuclear Energy Density Functional and Neutron Stars

In this chapter, we study single nucleus, heavy nuclei in dense matter and mass-radius of neutron stars using an energy density functional with parametrized density profile. Three different models are used and each model shows similar nuclear properties in the subnuclear density regions ($\rho < 0.07$ fm^{-3}). Analytic formulae for the Wigner-Seitz cell size, number of neutrons, and number of protons in the cell is given using least χ^2 fitting between numerical calculation and fitting function. The maximum mass of a neutron star is investigated, revealing differences among the models.

5.1 Nuclear energy density functional

In the nuclear energy density functional, the interaction energy comes from the contact force so the Hamiltonian density is a functional of number density and momentum density. For comparison with a finite range force, we used three energy density functional models. The first model is from Ref. [41] (EKO), the second one is the Skyme-type Potential Model (SPM) [32], and the last one is the Skyrme-Lyon force (SLy4).

In EKO, the Hamiltonian density is composed of homogeneous and inhomogeneous terms,

$$\mathcal{H} = \mathcal{H}_B(\rho_n, \rho_p) + \mathcal{H}_g(\rho_n, \rho_p, \nabla\rho_n, \nabla\rho_p) + \mathcal{H}_c\,. \tag{5.1}$$

The homogeneous term has the form

$$\mathcal{H}_0 = \frac{\hbar^2}{2m_n}\tau_n + \frac{\hbar^2}{2m_p}\tau_p + (1-\delta^2)v_s(\rho) + \delta^2 v_n(\rho), \tag{5.2}$$

where $\rho = \rho_n + \rho_p$ and $\delta = (\rho_n - \rho_p)/\rho$. The quantities $v_s(\rho)$ and $v_n(\rho)$ are potential energy density, which represents the potential contribution from symmetric nuclear matter and pure

neutron matter respectively. Those contribution are given by

$$\begin{aligned} v_s(\rho) &= a_1\rho^2 + \frac{a_2\rho^3}{1+a_3\rho} \\ v_n(\rho) &= b_1\rho^2 + \frac{b_2\rho^3}{1+b_3\rho}\,. \end{aligned} \tag{5.3}$$

The inhomogeneity (gradient) term $\mathcal{H}_g$ which is responsible for the surface tension of nuclei is being used as

$$\mathcal{H}_g = F_0|\nabla\rho|^2\,. \tag{5.4}$$

The Coulomb energy density is given by

$$E_c = \frac{e^2}{2}\int d^3r d^3r' \frac{1}{|\boldsymbol{r}-\boldsymbol{r'}|}(\rho_p(r)-\rho_e)(\rho_p(r')-\rho_e)\,, \tag{5.5}$$

In SPM and SLy4, the Hamiltonian density is given in Eq. (2.3, 2.4,2.5 2.6,2.7)
For all three models, we use a parametrized density profile (PDP) † for protons and neutrons before a phase transition to uniform nuclear matter takes place.
In PDP, we assume that nuclear density follows [41],

$$\rho_i(r) = \begin{cases} (\rho_i^{\rm in}-\rho_i^{\rm out})\left[1-\left(\frac{r}{R_i}\right)^{t_i}\right]^3 + \rho_i^{\rm out}\,, & r < R_i \\ \rho_i^{out}\,, & r \geq R_i. \end{cases} \tag{5.6}$$

The momentum density is simplified to

$$\tau_{n,p} = \frac{3}{5}(3\pi^2)^{2/3}(\rho_{n,p})^{5/3} \tag{5.7}$$

in the Thomas-Fermi approximation.

Table 5.1: Parameters in EKO

a_1	a_2	a_3	b_1	b_2	b_3	F_0
-458.384	2072.775	3.1668	-227.049	1058.942	2.608	61.917

Table 5.1, 5.2 show the parameters of models which we used in this study.
To find the parameters in EKO, we used standard nuclear matter properties such as $E/A = -16$ MeV, $K = 235$ MeV, $p(\rho = \rho_0, x = 1/2) = 0$ MeV/fm^3, $S_v = 33.21$ MeV, $L = 68$ MeV. For b_3, we used least χ^2 fitting to FPS pure neutron matters. F_0 is also found from least χ^2 fitting of 2336 nuclei binding energy data.

†The parametrized density profile is not the actual solution of the Thomas Fermi approximation. The PDP is used to avoid the numerical difficulties of $\nabla\rho$.

Table 5.2: Parameters in SPM & SLy4

Parameters	SPM	SLy4
t_0	-2719.7	-2488.91
t_1	417.64	486.82
t_2	-66.687	-545.39
t_3	15042	13777.0
ϵ	0.14416	1/6
$x0$	0.16154	0.834
$x1$	-0.047986	-0.344
$x2$	0.027170	-1.000
$x3$	0.13611	1.354

5.2 Binding energy of single nucleus

We calculate the binding energy of a single nucleus such as ^{40}Ca, ^{90}Zr, and ^{208}Pb. These nuclei have closed shells so we can neglect shell effects.
In a single nucleus, $\rho_{n,p}^{\rm out} = 0$ since there are no dripped nucleons.

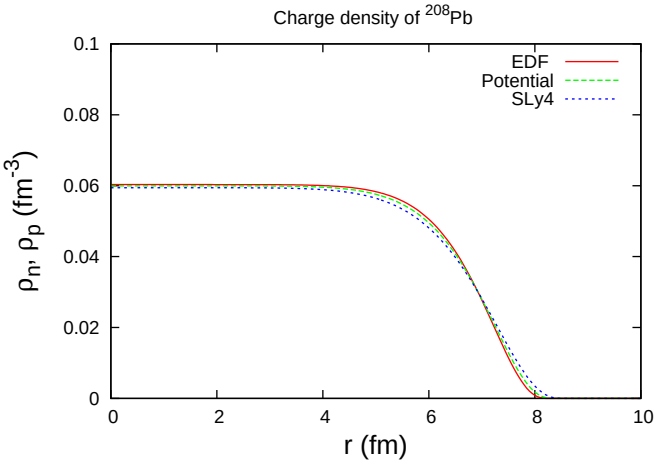

Figure 5.1: Proton density profile of ^{208}Pb.

Table 5.3 shows the properties of a single nucleus from both experimental results and a model calculation. In table 5.3, r_{ch} is the charge radius, BE/A is the binding energy per baryon, and δR is defined as $r_n - r_p$, where $r_{n,p}$ is the root-mean-square radius of neutron and proton. The density profiles for the single nucleus are given in Fig 5.1. Each model agrees well with the experimental result. The PDP shows the maximum baryon density at the center of the nucleus because of its mathematical expression. However, many of heavy nuclei with large number of protons (e.g. ^{208}Pb) have maximum baryon density off the center because of Coulomb repulsion. Thus PDP cannot show the exact density profile of a single

Table 5.3: Nuclear properties of single nucleus

Nucleus	Exp	EKO	SPM	Sly4
^{40}Ca r_{ch} (fm)	3.48	3.36	3.37	3.42
BE/A (MeV)	8.45	8.51	8.51	8.14
δR	-0.06 ± 0.05, -0.05 ± 0.04	-0.03	-0.04	-0.04
^{90}Zr r_{ch} (fm)	4.27	4.23	4.23	4.28
BE/A (MeV)	8.71	8.74	8.68	8.42
δR	0.09 ± 0.07	0.05	0.06	0.05
^{208}Pb r_{ch} (fm)	5.50	5.51	5.50	5.55
BE/A (MeV)	7.87	7.85	7.74	7.56
δR (fm)	0.12 ± 0.05, 0.20 ± 0.04	0.11	0.14	0.12

nucleus. Except for the density profile, PDP can be used as an approximated density profile to find the charge radius, binding energy per baryon, and δR.

5.3 Neutron Star Crust

In a neutron star, as the density increases, the pressure from degenerate electrons reaches a point where the electrons can no longer support the gravitational collapse and the neutrons replace the role of electrons soon after the neutron drip. The neutron drip divides the outer crust and inner crust of the neutron star. There is a phase transition around 0.5 ρ_0 [41] between inner crust and liquid core since the nuclear system favors the lowest energy state. Even though there might be sequential phase transition from spherical nuclei with a free of neutron gas, cylindrical phase, slab, cylindrical hole, bubble to uniform matter, the difference in the energy density and press is negligible. Thus we consider the phase transition from spherical nuclei phase to uniform nuclear matter. We can simply compare the energy density of uniform nuclear matter with heavy nuclei with a free of neutron gas.

5.3.1 Neutron drip

The neutron drips from heavy nuclei as their density increases. The drip point can be searched from a lower baryon density region. As the density increases, the neutron chemical potential increases, becomes positive, and neutrons start to drip. In case of protons, the chemical potential remains negative so there are never any dripped protons at T=0 MeV. Table 5.4 shows the neutron drip density for different models. In case of EKO, the neutrons start to drip when $\rho = 2.26 \times 10^{-4}$ fm^{-3}.

Before the neutron drip, the total pressure comes from only electron contribution and soon after the neutron drip, the pressure from dripped neutrons overwhelm the electron contribution.

Table 5.4: Neutron drip densities for all 3 models

	EKO	SPM	SLy4
ρ (fm^{-3})	2.2594×10^{-4}	2.4491×10^{-4}	2.0749×10^{-4}

5.3.2 Phase transition to uniform nuclear matter

To see the phase transition from lattice nuclei with a gas of free neutrons, we compare the energy per baryon for each model. Since it is believed that the energy differences arise between various pasta phases, we simply compare the energy per baryon from lattice nuclei with neutron gas with one from uniform nuclear matter. We may use the Maxwell construction to find the phase transition points between two phases. The total energy density of two phases in Ref. [22] can be written as

$$E = vE_h + (1-v)E_l\,, \tag{5.8}$$

where $\rho = v\rho_h + (1-v)\rho_l$. The high and low density of the boundary can be found from solving $p_h = p_l$ and $\mu_{nh} = \mu_{nl}$ at the same time. A numerical calculation does not yield an exact intersection for the solution.

Table 5.5: Phase transition points to uniform nuclear matter

	EKO	Potential	SLy4
ρ (fm^{-3})	0.0759	0.0670	0.0742

5.3.3 Statistical formulae for heavy nuclei in the neutron star crust

We compare the model calculation with a statistical formula for number of protons and neutrons in heavy nuclei and Wigner-Seitz cell size. Fitting formulae for the number of protons and neutrons can be used in neutron star cooling process. That is, neutrinos are emitted through $e-Z$ bremsstahlung [62] in the crust,

$$\epsilon_{e-Z} = 2.1\times10^{20}\frac{Z^2}{A}\left(\frac{\rho}{\rho_0}\right)T_9^6\,\mathrm{erg/cm^3/s}\,, \tag{5.9}$$

where $T_9 = T/10^9$ K. For this, we present two formulae before and after the neutron drip for each curve (Z_{nuc}, N_{nuc}, and R_c vs ρ) since the derivative of each curve w.r.t ρ_B is not continuous. After the neutron drip, we suggest different types of formulae† for each curve

†Fitting functions in this study are introduced to reflect the numerical result correctly. Since the number of protons increases suddenly before the uniform matter phase transition, c_6 is added.

which are

$$\begin{aligned} f_{R_c} &= a_0 + a_1 x + a_2 x^2 + a_3 x^3 + a_4 x^4 + a_5 x^5 \\ f_{N_{nuc}} &= b_0 + b_1 z + b_2 z^2 + b_3 z^3 + b_4 z^4 + b_5 x^5 \\ f_{Z_{nuc}} &= c_0 + c_1 z + c_2 z^2 + c_3 z^3 + c_4 z^4 + c_5 z^5 + \frac{c_6}{\sqrt{z}} \,. \end{aligned} \tag{5.10}$$

where $x = \ln(\rho\,\mathrm{fm}^3)$ and $z = 100\rho$ fm^3.
All a's, b's, and c's parameters can be found from the least χ^2 square fitting, in which χ^2 is given by

$$\chi^2 = \frac{1}{N}\sum_i^N (f_i - f_{model})^2 \,. \tag{5.11}$$

Table 5.6: Fitting formulae for Wigner-Seitz cell size after the neutron drip

	a_0	a_1	a_2	a_3	a_4	a_5
EKO	-30.812	-30.344	-8.004	-1.428	-0.131	-4.561×10^{-3}
SPM	-39.193	-30.239	-5.414	0.631	-4.313×10^{-3}	-1.334×10^{-3}
SLy4	20.120	13.383	6.504	0.918	5.748×10^{-2}	1.367×10^{-3}

Table 5.7: Fitting formulae for number of neutrons in the heavy nuclei after the neutron drip

	b_0	b_1	b_2	b_3	b_4	b_5
EKO	77.737	93.069	-52.346	20.942	-3.740	0.251
SPM	76.989	75.456	-49.337	21.835	-4.239	0.311
SLy4	87.680	86.728	-12.821	3.396	-0.560	6.366×10^{-2}

Table 5.8: Statistical formulae for number of protons in the heavy nuclei after the neutron drip

c	EKO	SPM	SLy4
c_0	36.947	34.619	40.389
c_1	1.877	-2.306	5.447
c_2	-2.921	5.854×10^{-2}	-4.265
c_3	0.942	-4.286×10^{-2}	1.362
c_4	-0.143	5.375×10^{-3}	-0.214
c_5	8.195×10^{-3}	-	1.301×10^{-2}
c_6	-0.171	-0.131	-0.203

Before the neutron drip, another type of formula fits the numerical calculations since the behavior of Winger-Seitz cell size, number of neutrons, and number of protons in the cell is relatively simple.

$$\begin{aligned} f_{R_c} &= \exp(a_0 + a_1 x + a_2 x^2) \\ f_{N_{nuc}} &= b_0 + b_1 (x - x_0)^7 + b_2 (x - x_0)^9 \\ f_{Z_{nuc}} &= c_0 + c_1 (x - x_0)^7 + c_2 (x - x_0)^9 \,. \end{aligned} \tag{5.12}$$

where $x = \ln(\rho\,\mathrm{fm}^3)$ and $x_0 = \ln(10^{-14})$.

Table 5.9: Fitting formulae before the neutron drip

	EKO	SPM	SLy4
a_0	1.2571	1.2489	1.2909
a_1	-0.3028	-0.3027	-0.3020
a_2	6.2495×10^{-4}	6.2487×10^{-4}	6.3943×10^{-4}
b_0	34.1418	33.2440	36.8709
b_1	3.2976×10^{-9}	4.1044×10^{-9}	3.6671×10^{-9}
b_2	1.1095×10^{-11}	9.3710×10^{-12}	1.2652×10^{-11}
c_0	27.8058	26.9215	29.7386
c_1	2.9168×10^{-9}	3.2463×10^{-9}	3.1409×10^{-9}
c_2	-1.8428×10^{-12}	-2.8772×10^{-12}	-1.6480×10^{-12}

Fig. 5.2 shows the atomic number in neutron star crust after the neutron drip happens. The fitting function works very well for EKO, SPM, and SLy4. The full Thomas Fermi approximation is added in case of truncated FRTF model. In the general case, a full Thomas Fermi numerical calculation has such a wiggle because of multiple minima [‡].

5.4 Mass-Radius of a cold neutron star

The uniform nuclear matter exists in the core of a neutron star as a result of a nuclear phase transition. The matter in the core is in the beta equilibrium state to minimize the total energy density. Mathematically, the beta equilibrium state equation can be obtained from a Lagrange multiplier method, which says

$$\mu_n = \mu_p + \mu_e \tag{5.13}$$

where $\mu_{n,p,e}$ are chemical potentials of the neutron, proton, and electron respectively.
Nuclear matter beyond the nuclear saturation densities exists in the core of neutron stars. This means that the mass-radius relation of neutron stars can be a good barometer of nuclear models. TOV equation (Eq. 4.46) is used to construct the neutron star's mass and radius.

[‡]Since the Wigner-Seitz cell size is unknown and to be found numerically, R_c does not smooth near the phase transition density.

parametrized[ht]

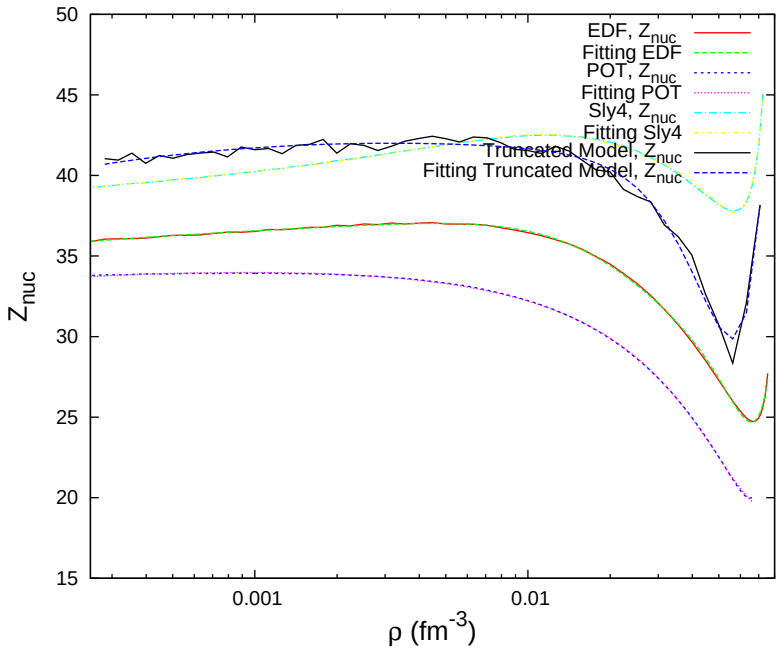

Figure 5.2: This figure shows the number of protons in neutron star crust from numerical calculation and fitting function. Truncated model calculation is added for comparison.

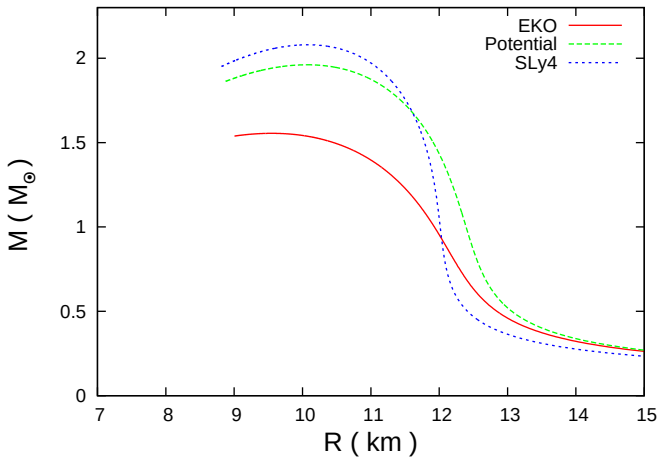

Figure 5.3: Mass and radius relation of cold neutron star from energy density functional

The simple EKO does not satisfy the $2.0M_{\odot}$ neutron star. Other models show that the maximum mass of neutron stars is greater than $2.0M_{\odot}$. Nuclear matter at high densities cannot be described by simple mathematical density functional but we need to consider more complex nuclear force arising from many body effects or QCD (quantum chromodynamics) effects.

5.5 Conclusion

PDP can be used to study a single nucleus and nuclei in dense matter. Even though PDP is not a true solution of density profiles, it can give enough accuracy in the total energy and continuous properties in Wigner-Seitz cell calculation like liquid droplet approach. Therefore, PDP is an alternative method to construct a nuclear equation of state for hot dense matter. Even though all three models show similar properties of nuclear matter such as binding energy of single nucleus, phase transition points, proton fractions, and Wigner-Seitz cell size, each model shows the different maximum mass of neutron star. For example, the simple EKO model cannot describe 2.0 $M_{\odot}$ neutron star. That means that the potential energy in EKO should be replaced with a more realistic force model.
The simple division of symmetric potential and pure neutron potential does not work, such that the δ term in the potential should have more than δ^2 interaction. This also means that the extrapolation beyond the nuclear saturation density is still an open problem which needs to be checked by mass and radius relation of neutron stars.

Chapter 6

Nuclear Equation of State for Hot Dense Matter

† There are many demands for a nuclear equation of state for hot dense matter. Core collapsing supernova explosions, neutron star binary mergers, and proto-neutron star simulation need a highly thermodynamically consistent EOS table. The recent development of technology enables us to develop full 3D simulations of the above phenomenon. However, only a few EOS tables are available. Furthermore, except for LS220 [22], no EOS tables can satisfy the mass and radius relation of neutron stars and nuclear experiments at the same time.
Our EOS follows the methodology of LPRL [17] and Lattimer & Swesty [22]. We employ FRTF and SLy4 as a nuclear force model and the Liquid Droplet approach as a numerical technique.

6.1 Construction of EOS

To construct the EOS table, we need two basic tools. One is the nuclear force model. Another is a numerical technique.
For a nuclear force model, we can use (see chapter 1, 2, & 3) the following,

- Non-relativistic potential model
- Relativistic mean field model
- Finite-Range Thomas Fermi model .

As a numerical technique, we might choose,

- Liquid Droplet Approach
- Thomas Fermi Approximation
- Hartree (Fock) Approximation .

†This chapter is based on J.M. Lattimer and Y. Lim's work. We are checking the thermodynamic consistencies and will submit our work and provide the new EOS table soon.

These two tools can be combined to construct a Nuclear EOS Publicly available EOS tables are

- LS EOS [22]
  - Combines Skyrme type force model with Liquid droplet model,
  - Disregard consider neutron skin,
  - Consider phase transion using geometric function,
  - LS 220 is the best until now,

- STOS [59]
  - Uses RMF and semi-Thomas Fermi approximation (parametrized density profile.)
  - Awkward grid spacing,
  - New version available (2011), added hyperon interactions,

- SHT [61]
  - Uses RMF and Hartree Approximation ,
  - Larger radius for given mass of neutron stars,

For constructing our EOS table, we reconsider the LPRL numerical technique which includes neutron skin. As an improvement, we add Coulomb diffusion and Coulomb exchange energy. The liquid droplet approach is the only method which can guarantee thermodynamic consistency. We can obtain analytic derivatives for $\partial p/\partial \rho$, $\partial p/\partial T$, $\partial p/\partial Y_p$, etc.

The other approaches (Thomas Fermi, Hartree-Fock approximation) cannot give enough accuracy in thermodynamics because they have convergence issues. The thermodynamic derivatives can be obtained through the numerical derivatives in TF or HF. This can also produce a thermodynamic inconsistency.
The numerical time needed to construct the whole table can also be a problem. In SHT [61], it took 6,000 CPU-days to calculate 107,000 grid points. If we use the LDM approach, it takes less than 10 minutes to calculate $121 \times 50 \sim 302,500$ grid points. That means that we can easily generate another table using a different nuclear force model. We also consider phase transitions which occur in a neutron star's inner crust, as was done in the LS models.

As a nuclear force model, we use FRTF models and SLy4. SLy4 is believed to be the most accurate Skyreme-type nuclear force model. We choose it for comparison to check our FRTF model parameters.

6.2 Liquid Droplet Model as a numerical technique

First, we demonstrate that the liquid droplet model adequately describes nuclei. The liquid droplet model provides us with the energy per baryon of a single nucleus and nuclei in dense matter. The idea behind it is that the energy contribution of nuclei comes from bulk, surface,

Coulomb, and, symmetry part [24], in addition, there is a pairing effect such that [32]

$$\begin{aligned} E(A,Z) = &- BA + E_s A^{2/3} + S_v A \frac{(1-2Z/A)^2}{1+S_s A^{-1/3}/S_v} + E_C \frac{Z^2}{A} \\ &+ E_{\text{diff}} \frac{Z^2}{A} + E_{\text{ex}} \frac{Z^{4/3}}{A} + a \frac{\Delta}{\sqrt{A}} \,. \end{aligned} \tag{6.1}$$

In the above equation, B is the binding energy per baryon in the bulk nuclear matter, E_s is the surface symmetry energy, E_C, E_{diff}, and E_{ex} are energy coefficients in classical, diffusion, and exchange Coulomb energy. The coefficient a is 1 for odd-odd nuclei, 0 for odd-even nuclei, and -1 for even-even nuclei. The paring constant (Δ) is kept constant at 12 MeV. This liquid droplet model can be extended by adding the nuclear shell effect. The empirical formula for this shell effect is given by [50]

$$E_{\text{shell}} = \frac{1}{2} a_m (N_v + P_v) + \frac{1}{4} b_m (N_v + P_v)^2 \tag{6.2}$$

where N_v and P_v is the minimum difference for neutrons and protons between magic number, 2, 8, 20, 28, 50, 82, 126, and, 184. For example, $A = 50, Z = 23, N = 27$, then $Z_v = |23 - 20| = 3$, $N_v = |27 - 28| = 1$.

The general way to minimize the total energy at $T = 0$ MeV[†] for a given Z and A, we adopt the μ_n approach, in which only neutron skin exists on the surface of nuclei. μ_α method exists [32], however, it gives a different slope (S_s/S_v vs S_v) from the one μ_n method. We confirmed the slope from μ_n is closed to the one from FRTF model.

For a given nuclear model, the total energy (excluding rest mass energy) is given by

$$E = f_B(A - N_s) + 4\pi R^2 \sigma(\mu_n) + \mu_n N_s + E_C(R), \tag{6.3}$$

where f_B is the binding energy per baryon for a specific nuclear model and N_s is the total number of neutrons on the surface. We include in E_C the Coulomb, diffusive surface, and exchange energies. We assume that $f_B = f_B(\rho, x)$.
With two constraints,

$$\begin{aligned} x &= \frac{Z}{A - N_s} \\ A - N_s &= \frac{4\pi R^3}{3} \rho \end{aligned} \tag{6.4}$$

we can find the minimum of total binding energy using the Lagrange multiplier method.

$$\begin{aligned} E(\mu_n, N_s, R, \rho, x, \lambda_1, \lambda_2) = &f_B(\rho, x)(A - N_s) + 4\pi R^2 \sigma(\mu_n) + \mu_n N_s + E_c(R) \\ &+ \lambda_1 (A - N_s - \frac{4\pi R^3}{3} \rho) + \lambda_2 (Z - x(A - N_s)) \,. \end{aligned} \tag{6.5}$$

[†]If $T \neq 0$ MeV, we need to minimize the total free energy or free energy density because of entropy.

The derivative of E with respect to the unknowns gives,

$$\frac{\partial E}{\partial \mu_n} = 0: \quad 4\pi R^2 \frac{\partial \sigma}{\partial \mu_n} + N_s = 0 \tag{6.6a}$$

$$\frac{\partial E}{\partial N_s} = 0: \quad -f_B + \mu_n - \lambda_1 + x\lambda_2 = 0 \tag{6.6b}$$

$$\frac{\partial E}{\partial R} = 0: \quad 8\pi R\sigma + \frac{\partial E_C}{\partial R} - 4\pi R^2 \rho \lambda_1 = 0 \tag{6.6c}$$

$$\frac{\partial E}{\partial \rho} = 0: \quad \frac{\partial f_B}{\partial \rho}(A - N_s) - \lambda_1 \frac{4\pi}{3} R^3 = 0 \tag{6.6d}$$

$$\frac{\partial E}{\partial x} = 0: \quad \frac{\partial f_B}{\partial x}(A - N_s) - \lambda_2 (A - N_s) = 0 \tag{6.6e}$$

$$\frac{\partial E}{\partial \lambda_1} = 0: \quad A - N_s - \frac{4\pi}{3} R^3 \rho = 0 \tag{6.6f}$$

$$\frac{\partial E}{\partial \lambda_2} = 0: \quad Z - x(A - N_s) = 0\,. \tag{6.6g}$$

We will correct $E(A, Z)$ by the shell and pairing energies so these do not need to be included in the above. From eq. (6.6e) we have

$$\lambda_2 = \frac{\partial f_B}{\partial x}\,, \tag{6.7}$$

from eq. (6.6d) and (6.6f), we get

$$\lambda_1 = \rho \frac{\partial f_B}{\partial \rho}\,. \tag{6.8}$$

Using λ_1, λ_2, and eq. (6.6b), we obtain

$$\mu_n = f_B + \rho \frac{\partial f_B}{\partial \rho} - x \frac{\partial f_B}{\partial x}\,. \tag{6.9}$$

If we assume that σ depends on μ_n through x not ρ, and $\sigma = \sigma_0 - (1 - 2x)^2 \sigma_\delta$, we have four equations to solve, which are

$$4\pi R^2 4(1 - 2x) \frac{1}{\partial \mu_n / \partial x} + N_s = 0 \tag{6.10a}$$

$$8\pi R^2 \sigma + \frac{\partial E_c}{\partial R} - 4\pi R^2 \rho^2 \frac{\partial f_B}{\partial \rho} = 0 \tag{6.10b}$$

$$A - N_s - \frac{4\pi}{3} R^3 \rho = 0 \tag{6.10c}$$

$$Z - x(A - N_s) = 0\,. \tag{6.10d}$$

We can eliminate N_s, leading to three equations to solve,

$$16\pi R^2(1-2x)\sigma_\delta + \frac{\partial \mu_n}{\partial x}\left(A - \frac{4\pi}{3}R^3\rho\right) = 0 \tag{6.11a}$$

$$8\pi R^2(\sigma_0 - (1-2x)^2\sigma_\delta) + \frac{\partial E_c}{\partial R} - 4\pi R^2\rho^2\frac{\partial f_B}{\partial \rho} = 0 \tag{6.11b}$$

$$Z - \frac{4\pi}{3}R^3\rho x = 0\,. \tag{6.11c}$$

In the case of the incompressible model where ρ in the nuclei is fixed for all nuclei, we are left with one equation to solve (eq. 6.11a) :

$$16\pi\left(\frac{3}{4\pi\rho_0}\right)^{2/3}\left(\frac{Z}{x}\right)^{2/3}(1-2x)\sigma_\delta + \frac{\partial \mu_n}{\partial x}\left(A - \frac{Z}{x}\right) = 0\,, \tag{6.12}$$

with $\mu_n = f_B - x\frac{\partial f_B}{\partial x}$. In case of the simplest nuclear model,

$$f_B = -B + S_v(1-2x)^2 + \frac{K}{18}(1-u)^2\,. \tag{6.13}$$

Fig. **??** and 6.2 shows the contour plot of χ^2 for S_s/S_v and S_v space. The χ^2 from total

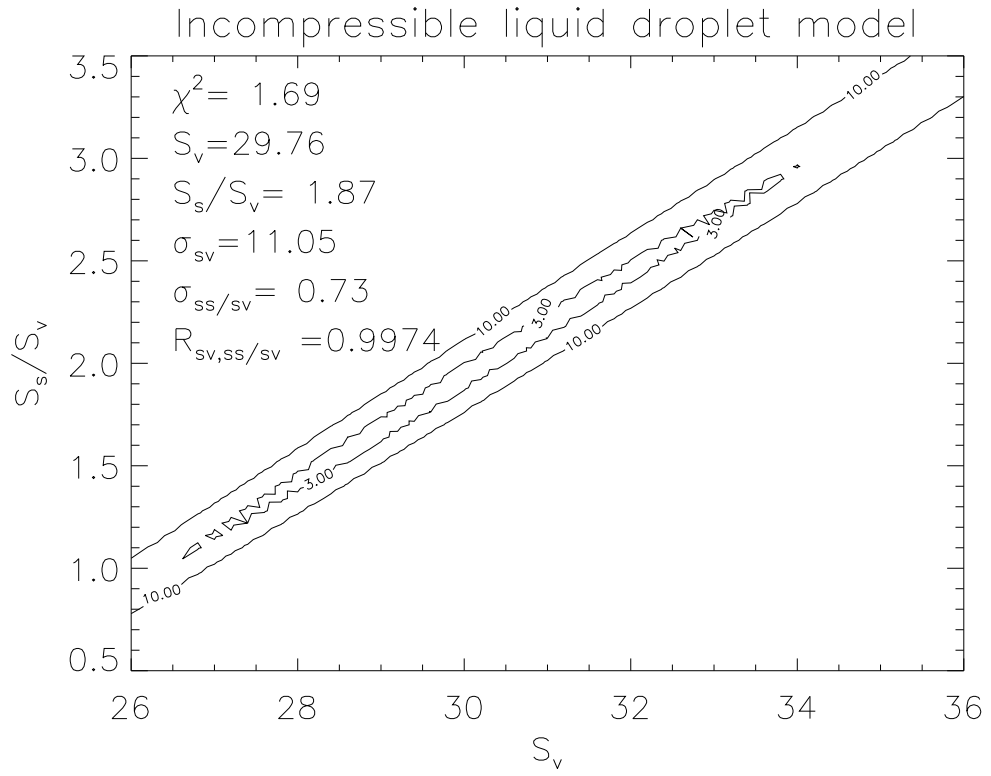

Figure 6.1: This is a contour plot of χ^2 when $\rho_0 = 0.155/\mathrm{fm}^3$ from incompressible model.

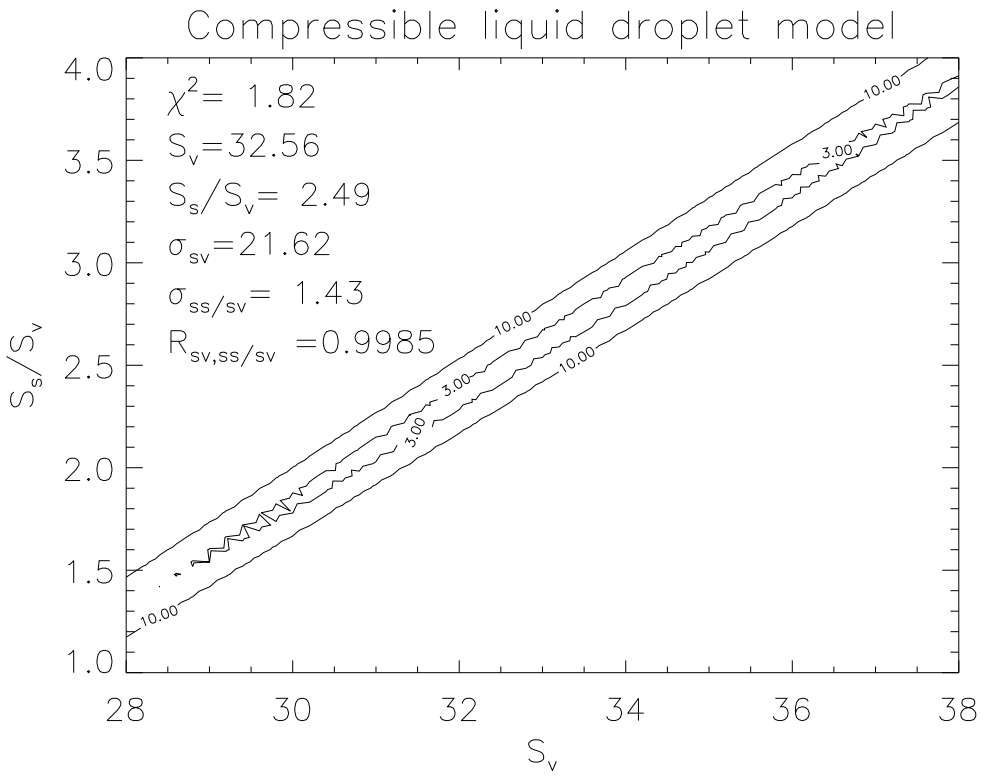

Figure 6.2: This is a contour plot of χ^2 from compressible and incompressible model.

binding energy of nuclei is not much different in both cases but the least χ^2 points with respect to S_v and S_s/S_v are different. The σ_{S_v} and σ_{S_s/S_v} [†] from the compressible liquid droplet model are twice larger than the ones from the incompressible liquid droplet model, which result in the larger contour plot when $\chi^2 = 3$. The correlations between S_v and S_s/S_v from two models are almost same so the slopes from both models are parallel.
χ^2 from above two liquid droplet models are less than the one ($\chi^2 = 4.75$) from FRTF model. This justifies the use of the liquid droplet approach as a numerical technique to construct EOS tables.

6.3 Choice of nuclear force model

The nuclear force model to make the EOS table should represent both nuclear experiments on Earth and neutron star's mass and radius relation. Up to now, only LS220 [22] fits both of constraints. To a choose nuclear force model, we need to take several tests. We show the result from non-relativistic potential (Skyrme force) model. There are more than 100 models and our tests were done on 62 models. As a model of single nucleus properties, they are all good enough to represent binding energy and root-mean-square radius when we use Hartree-Fock code. However, most of the model did not pass the simple test such as

[†]We adopted arbitrary σ_0 as 1.0 MeV in this case.

pressure from pure neutron matter, maximum mass of a cold neutron star, and Steiner et al.[53] allowed area of mass and radius.

6.3.1 Pure neutron matter

The pressure in the pure neutron matter should increase as density increases since neutron alone cannot be bound at all. However, some of nuclear force models cannot represent this simple behaviour. Fig. 6.3 shows pure neutron matter pressure from some of Skyrme force

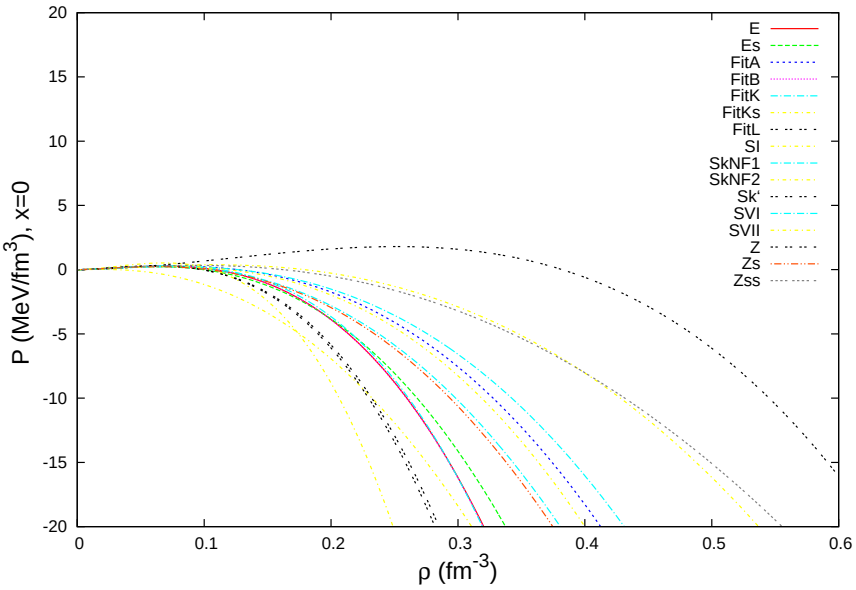

Figure 6.3: This figure shows the Skyrme force models which cannot make positive pressure of pure neutron matter.

models. These models on the list cannot explain positivity and monotonic slope of pressure. So, they should be excluded from the candidate of EOS nuclear force.

6.3.2 Maximum mass of a cold neutron star

Recently, PSR J16142230 [57] was found to have a mass of $1.97M_{\odot}$. Demorest et al.[57] analyzed time delay data of the pulsar's emission as it passed behind its white dwarf companion (Shapiro delay). This mass now becomes the minimum of maximum mass of neutron stars. Also this mass can be used to rule out the nuclear force model. Fig 6.4 shows the maximum mass of neutron star of some Skyrme force model. These models also cannot be used for suitable nuclear force model at high density.

6.3.3 Allowed region of mass and radii of neutron stars

Steiner et al.[53] analyzed the x-ray data and used atmosphere models of neutron stars to find the allowed area of mass and radii of neutron stars. From these regions, we can choose

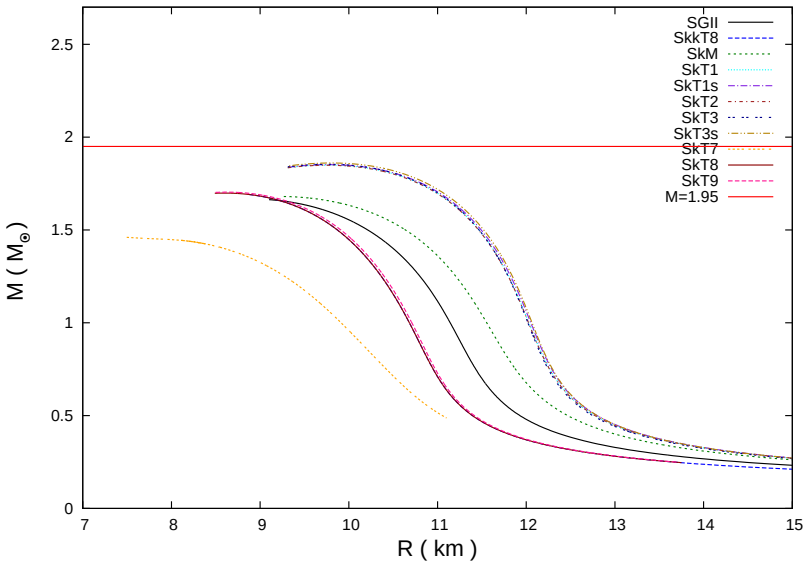

Figure 6.4: This figure shows the Skyrme force models which cannot produce a $1.97M_{\odot}$ neutron star.

final candidates for the nuclear force model of EOS table. Fig.6.5 shows the Skyrme force models which have too large radii for a given mass of neutron stars. Mathematically, these happen because of large L so it should be emphasized that L is another important nuclear constant which should be extracted from nuclear experiments or astrophysical observations. Of all three tests, we can see that SLy0, ... , SLy10, and our FRTF I, II, Gaussian models are good enough to be used as a nuclear force model. Fig.6.6 shows the mass and radius relation of Skyrme force models and our finite range force models, which are suitable for make an EOS table.
We did not take a test with any relativistic mean field models[†], since they usually have large L so they cannot make allowed regions of mass and radius in neutron stars.
To summarize (Appendix E), the nuclear force models which pass the 3 tests would have $S_v \simeq 32$ MeV, $L \simeq 46$ MeV, $K \simeq 230$ MeV, and $\rho_o \simeq 0.16\text{fm}^{-3}$.

6.4 Free energy

The fundamental idea of making an EOS table is to minimize free energy or free energy density for a given ρ, T, and Y_p. In the Liquid Droplet approach, the free energy in the Wigner-Seitz cell consists of the contributions from finite nuclei and nucleons outside finite nuclei. Fig. 6.7 shows the schematic picture inside the Wigner-Seitz cell. The heavy nuclei is in phase equilibrium with nucleons and alpha particles outside. The free energy per baryon contribution from heavy nuclei can be divided into,

$$f_N = f_{\text{bulk}} + f_{\text{Coul}} + f_{\text{surf}} + f_{\text{trans}} \tag{6.14}$$

[†]The $R_{1.4M_{\odot}} \propto L^{1/4}$ so RMF cannot make the allowed region.

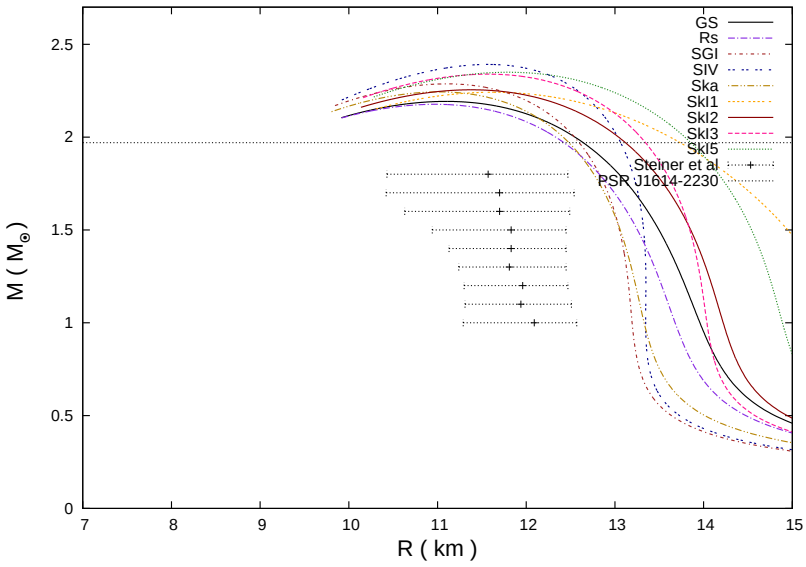

Figure 6.5: The Skyrme force models on the list have too large radii for given mass.

where f_{mbulk} is the free energy contribution from inside of heavy nuclei, $f_{\rm Coul}$ is the Coulomb energy contribution, $f_{\rm surf}$ is the one from surface, and $f_{\rm trans}$ comes from translational (or Kinetic) parametrizedenergy of heavy nuclei. We assume that heavy nuclei have uniform density from the center to the surface so we have the contribution from bulk and surface.

6.4.1 Bulk Matter inside and outside nuclei

The bulk free energy per baryon, $f_{\rm bulk}(\rho_i, x_i, T) \equiv f_{\rm bulk}/\rho_i$, is exactly that described in bulk matter in the finite range model (or SLy4). The subscript $i(o)$ refers to the bulk nuclear matter inside (outside) nuclei. The use of the same functional form for bulk matter both inside the nuclei and the 'dripped' bulk matter outside the nuclei is necessary for a consistent treatment. In general phase transition (which is often called, pasta phase) happen when the overall density (ρ) approach $0.5\rho_0$ to minize total energy.

6.4.2 Coulomb energy

The coulomb free energy is the electrostatic energy needed to assemble the static charge configuration. As an illustration, one could assume the positive charge of protons is distributed uniformly within a spherical nuclear volume (radius r_N), and this charge is neutralized by an equal, but opposite, charge distributed within radius (r_c) of a neutral (Wigner-Seitz) cell. In this case, the number density of nuclei would be $n_N = 3/(4\pi r_c^3)$, and the atomic number would be $Z = 4\pi r_N^3 \rho_i x_i/3$. As shown by Baym et al.[2], the Coulomb energy density of spherical nuclei is then given by

$$f_{\rm Coul} = \frac{3}{5}\frac{Z^2 e^2 \rho_N}{r_N}\left(1 - \frac{3}{2}u^{1/3} + \frac{1}{2}u\right) \equiv \frac{4\pi}{5}(r_N \rho_i x_i e)^2 D(u) \qquad (6.15)$$

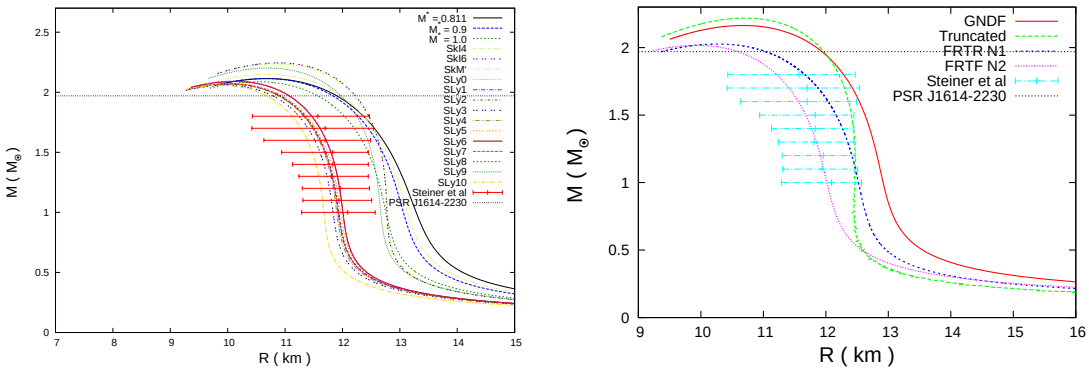

Figure 6.6: The left panel shows mass and radius relation of the Skyrme force models which passes all tests. The right figure shows the one from our force models.

where $u = (r_N/r_c)^3$ is the fraction of space occupied by the nuclei. This relation defines the function $D(u)$.

As shown by Ravenhall et al.[58] in many situations it may be energetically favorable for nuclei to deform from spheres into cylinders or plates, or even turn 'inside out' to form relatively vacuous bubbles surrounded by spherical nuclei and could also deform into spheroidal shapes. In an attempt to account for varying shapes that would minimize the systematic free energy, Lattimer & Swesty [22] defined a Coulomb shape function $c(u)$,

$$f_{\rm Coul} = \frac{4\pi}{5}(r_N \rho_i x_i e)^2 c(u)\,. \tag{6.16}$$

In the low density limit in which nuclei are expected to be spherical, $c(u) = uD(u)$. In the limit in which nuclei are inside-out, but the resulting bubbles are spherical,
$c = (1-u)D(1-u)$.

6.4.3 Nuclear surface energy

In the liquid droplet model, the surface energy is not calculated dynamically, but is instead parametrized as a leptodermous expansion in the curvature R^{-1} where R is the nuclear radius. In this work, we keep only the lowest order term, which is the surface tension of a semi-infinite, plane interface between two nuclear phases in mechanical and chemical equilibrium. The dense phase is characterized by the densities ρ_{ni}, ρ_{pi} corresponding to those inside the nucleus, while the light phase, characterized by the densities ρ_{no}, ρ_{po}, corresponds to the nuclear vapor outside nuclei. The neutron and proton chemical potentials for semi-infinite matter must be equal in both phases, and they are denoted by μ_n and μ_p respectively. At a given temperature, the phase equilibrium is determined by a single quantity, which can be taken to be the proton fraction x_i in the dense phase, or by the neutron chemical potential μ_n, or by the neutron-proton chemical potential difference $\mu_n - \mu_p$. The surface tension is actually a thermodynamic potential, and as a consequence it is formally a function of the neutron and proton chemical potentials, as well as of the temperature. If finite-size effects

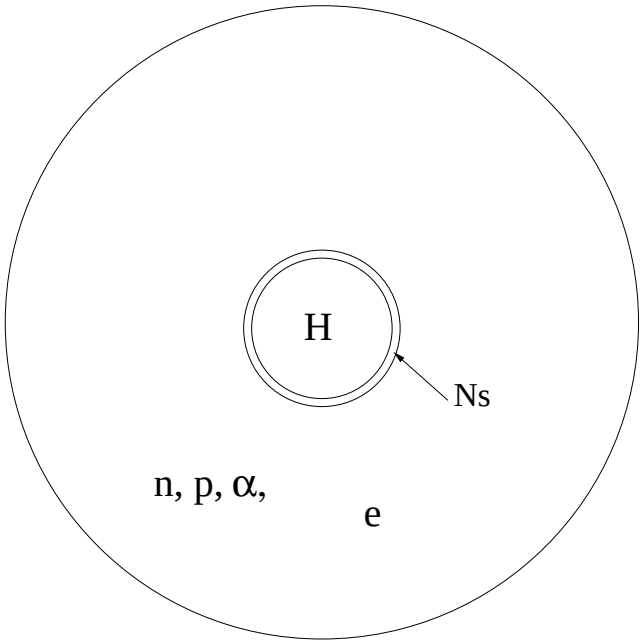

Figure 6.7: In the Wigner Seitz cell, there are one heavy nuclei and nucleons, electrons, and alpha particles outside. In this model, we have neutron skin on the surface of heavy nuclei.

such as the Coulomb forces can be ignored, the phase equilibrium dictates that the chemical potentials follow a unique trajectory determined only by the temperature and proton fraction in the dense phase. The work of Lattimer et al.[17] assumed that the surface tension could be therefore treated directly as a function of x_i and T.

However, Coulomb and other finite-size effects are not negligible, and the surface tension is modified by them. The approach we initially employ here is to treat the surface tension as a function of the neutron chemical potential of the surface (and temperature), and in turn to treat the neutron chemical potential of the surface as a function of the dense proton fraction (and the temperature).

As in chapter 2, the surface tension σ is obtained by minimization of the total free energy per unit area, and results in

$$\sigma = \int_{-\infty}^{\infty} (F - \mu_n \rho_n - \mu_p \rho_p - p_o) dz \tag{6.17}$$

where $F = H - TS_B$ and p_o is the pressure of the bulk matter (if any) in the dilute phase in the limit $z \to \infty$.

We employ a simplified description following Lattimer et al.[17], but extend it to contain three adjustable parameters: the surface tension of zero-temperature symmetric matter, the zero-temperature surface symmetry parameter, and a parameter describing the entropy (or

specific heat) of the surface of symmetric mater. This description is given below.

What appears in the liquid droplet model, however, is the surface free energy per unit area $\sigma + \mu_n\nu_n + \mu_p\nu_p$, where ν_t represent the areal density of particles in the surface. It will be found that these are determined by

$$\nu_t = -\frac{\partial\sigma}{\partial\mu_t}\Big|_T, \tag{6.18}$$

as is expected from thermodynamics. Since our liquid droplet model takes the reference interface to be located at the proton surface, this model explicitly considers a skin made only of neutrons. There are no 'surface protons', and $\nu_p = 0$. This is consistent with the statement above that, at a given temperature, the quantity σ is a function of a single quantity, μ_n. Therefore, the surface free energy per area is simply $\sigma(\mu_n, T) + \mu_n\nu_n$. In what follows, the neutron chemical potential for the surface is denoted by μ_s, but it will be shown that free energy minimization requires $\mu_s = \mu_{no}$.

The surface free energy density for spherical nuclei is thus

$$f_{\rm surf} = 4\pi r_N^2\rho_n(\sigma(\mu_s, T) + \mu_s\nu_n) = \frac{3u}{r_N}(\sigma(\mu_s, T) + \mu_s\nu_n)\,. \tag{6.19}$$

Once again, following the discussion of Lattimer & Swesty [22], the consequences of nuclear deformation or shape change are taken into account by the surface shape factor $s(u)$, so that

$$f_{\rm surf} = \frac{3s(u)}{r_N}(\sigma(\mu_s, T) + \mu_s\nu_n)\,. \tag{6.20}$$

Obviously, $s(u) = u$ for a sphere. As is the case for $c(u)$, the precise form for $s(u)$ will be required.

In practice, the results of plane-parallel surface energy calculations are most easily rendered in terms of the functions $\sigma(x, T)$ and $\mu_s(x, T)$, where x is the reference asymptotic proton fraction of the dense phase. Note that x is equivalent to x_i for a plane-parallel surface, but is not necessarily equivalent to x_i for a finite liquid droplet nucleus. The quantity x is simply a convenient intermediate variable used to simplify the construction of $\sigma(\mu_s)$.

As in section 3.4, we write the surface tension as a two-parameter function times a temperature dependence:

$$\sigma(x, T) = \sigma_o h(x, T)\left(\frac{2\cdot 2^\alpha + q}{x^{-\alpha} + q + (1-x)^{-\alpha}}\right)\,. \tag{6.21}$$

The quantity σ_o is the zero-temperature, symmetric matter, surface tension. In case of Skyrme force model, the numerical calculation of surface tension is not stable since it is a differential equation rather than an integral equation. The numerical method is described in Ravenhall et al. [29].

Table 6.1: Surface tension analytic fitting function for SLy4

Model	$\sigma_0(x_i = 0.5)$	α	q
SLy4	1.13754	3.4	29.0494

The factor $h(x,T)$ contains the explicit temperature dependence of the surface free energy, and can approximated by [29]

$$h(x,T) = \left[1 - \left(\frac{T}{T_c(x)}\right)\right]^p \tag{6.22}$$

where $T_c(x)$ is the maximum temperature for which nuclei can exist for a given value of x. For the truncate model and the modified model , $p = 5/3$ and $T_c(x)$ is given section 3.4. For SLy4, we use $p = 2$ [29]. $T_c(x)$ for SLy4 is given by the same formula, e.g. Eq. (3.31), but different coefficients.

Table 6.2: The critical temperature analytic fitting function for SLy4

Model	$T_{c,0}$	a	b	c
SLy4	14.502	-0.3649	-0.02025	-0.34368

The neutron chemical chemical potential μ_s, for a given value of x_i and T, is that which applies to bulk phase equilibrium. For proton fractions larger than approximately 0.3 at zero temperature, the phase outside the nucleus is a vacuum with $p_o = 0$. If the free energy is expanded about $\rho = \rho_0$ and T=0, the condition $p = 0$ results in

$$\mu_s(x,T) = f_{\rm bulk} - x\frac{\partial f_{\rm bulk}}{\partial x} \simeq -B - \frac{T^2}{15{\rm MeV}} + S_v(1-4x^2). \tag{6.23}$$

This formula works at low temperature and it cannot correctly represent neutron chemical potential on the surface. So, we may use a fitting function for neutron chemical potential of dense matter for given proton fraction and temperature. With appropriate units of coefficients,

$$\mu_s(x,T) = -B + \alpha(1-2x) + \beta(1-2x)^2 + \gamma T^2 + \delta(1-2x)T^2 \tag{6.24}$$

This fitting function is obtained from the numerical calculation of phase equilibrium. Table 6.4.3 shows the coefficients for the fitting function. Therefore, given that one of the equilibrium conditions will be $\mu_s = \mu_{no}$, the procedure is to determine the quantity x from μ_{no} and T by solving a quadratic equation.
The surface neutron density is then found from Eq. (6.18), or

$$\nu_n = -\frac{\partial\sigma(\mu_s,T)}{\partial\mu_s} = -\frac{\partial\sigma(x,T)}{\partial x}\left(\frac{\mu_s(x,T)}{\partial x}\right)^{-1}. \tag{6.25}$$

Table 6.3: The chemical potential fitting function

Model	B	α	β	γ	δ
Truncated	16.539	62.365	-28.900	-0.0455	-0.0414
Modified	16.000	79.627	-49.128	-0.0595	-0.1017
SLy4	15.987	63.963	-34.546	-0.0469	-0.0325

All surface thermodynamic quantities can then be evaluated. We again emphasize that for surface quantities, $x \neq x_i$ but close each other.

6.4.4 Nuclear translational energy

The nuclei essentially form a non-degenerate, non-relativistic Boltzmann gas. The free energy density of such a gas, ignoring any internal degrees of freedom, is

$$f_{\rm trans} = \rho_N(\mu_H - T) = \frac{u\rho_i}{A}T\left[\ln\left(\frac{u\rho_i}{\rho_Q A^{5/2}}\right) - 1\right]. \tag{6.26}$$

Here $\rho_Q = (mT/2\pi\hbar^2)^{3/2}$, where m is the nucleon mass, and μ_H represents a nuclear chemical potential. As in Lattimer et al.[17], it is assumed that the translational energy diminishes with temperature and disappears at T_c with the same behavior as the surface energy. This is enforced with the function $h(x_i, T)$. Following Lattimer & Swesty [22], the simplifying assumption is made to replace A in Eq. (6.26) with a constant $A_o = 60$ which is an approximation of mass number of heavy nuclei in neutron star crust. This approximation simplifies the algebra surrounding the equilibrium conditions. In addition, achieving a consistency in the limit $u \to 1$, where an inside-out phase may replace ordinary nuclei, u in Eq. (6.26) is replaced by $u(1-u)$. These approximations are justifiable, given that the translational energy is a relatively unimportant component. To summarize, the translational free energy density and nuclear chemical potential are taken to be

$$f_{\rm trans} = \frac{u(1-u)\rho_i}{A_o}h(x_i,T)(\mu_H - T); \qquad \mu_H = T\ln\left(\frac{u(1-u)\rho_i}{\rho_Q A_o^{5/2}}\right). \tag{6.27}$$

6.4.5 Alpha particles

To represent the thermodynamics of an ensemble of light nuclei, a gas of non-interacting, but finite volume, alpha particles is assumed. The alpha particles have substantial thermodynamic contributions in regions limited to those near the nuclear dissociation curves. The alpha particles for those temperatures and densities may be treated as a non-interacting Boltzmann gas. Alpha particles are bound relative to free neutrons by an energy $B_\alpha = 28.3$ MeV. Alpha particles also occupy a fairly large volume of space, $v_\alpha = 24$ fm^{-3} per alpha particle, and the total volume they occupy must be considered. With these stipulations, the

free energy density for the alpha particles is

$$F_\alpha = (1-u)\rho_\alpha(\mu_\alpha - T - B_\alpha)\,, \tag{6.28}$$

where ρ_α and μ_α are the number density and chemical potential of alpha particles, respectively. It is assumed that the fractional volume u is already occupied by nuclei and is not available for alpha particles to occupy. μ_α is related to ρ_α by

$$\mu_\alpha = T \ln\left(\frac{\rho_\alpha}{8\rho_Q}\right)\,. \tag{6.29}$$

6.5 The Combined model

The free energy of each component of dense matter has been developed in the previous sections. In dense matter, these components are present in varying concentrations, and one has to allow for the volume occupied by nuclei and by alpha particles. In the most general case, in which the four components H, n, p, α exists, the baryon conservation equation is

$$\rho = u\rho_i + 2s(u)\frac{\nu_n}{r_N} + (1-u)[4\rho_\alpha + (1-\rho_\alpha v_\alpha)\rho_o]\,. \tag{6.30}$$

The charge conservation equation is

$$\rho Y_p = ux_i\rho_i + (1-u)[2\rho_\alpha + (1-\rho_\alpha v_\alpha)x_o\rho_o]\,. \tag{6.31}$$

The total free energy density for the entire system becomes:

$$\begin{aligned} F =& u\rho_i f_{\rm bulk}(\rho_i, x_i, T) + \frac{3s(u)}{r_N}(\sigma(\mu_s, T) + \mu_s(x, T)\nu_n) + \frac{4\pi}{5}(r_N\rho_i x_i e)^2 c(u) \\ &+ f_{\rm trans}(u, \rho_i, x_i, T) + F_\alpha(\rho_\alpha, u, T) + (1-u)(1-\rho_\alpha v_\alpha)\rho_o f_{\rm bulk}(\rho_o, x_o, T)\,. \end{aligned} \tag{6.32}$$

We neglect the free energy contribution from leptons and photons since we can treat them separately in nuclear equilibrium.

6.5.1 Equilibrium conditions

The total free energy density is a function of the independent variables (ρ, Y_p, T), but also a function of the 9 independent variables $(\rho_i, x_i, r_N, \mu_s, \nu_n, u, \rho_o, x_o, \rho_\alpha)$. Note that ρ_o and x_o can be eliminated by the baryon and charge conservation equations:

$$\begin{aligned} \rho_o &= \left[\frac{1}{1-\rho_\alpha v_\alpha}\frac{\rho - u\rho_i - 3s\nu_n/r_N}{1-u} - 4\rho_\alpha\right] \\ x_o &= \frac{\rho Y_p - ux_i\rho_i - 2\rho_\alpha(1-u)}{\rho - u\rho_i - 3s\nu_n/r_N - 4\rho_\alpha(1-u)}\,. \end{aligned} \tag{6.33}$$

The specification of nuclear statistical equilibrium for the system demands that F be minimized with respect to each of the 7 remaining dependent variables. It is convenient to use

the seven $(\rho_i, x_i, r_N, x, \nu_n/r_N, u, \rho_\alpha)$ variables set.
The derivative with respect to ρ_o and x_o can be resolved with

$$
\begin{aligned}
&\frac{\partial \rho_o}{\partial \rho_i} = -\frac{u}{(1-u)(1-\rho_\alpha v_\alpha)}\,, \qquad \frac{\partial x_o}{\partial \rho_i} = -\frac{u(x_o - x_i)}{\rho_o(1-u)(1-\rho_\alpha v_\alpha)}\,,\\
&\frac{\partial \rho_o}{\partial x_i} = 0\,, \qquad\qquad\qquad\qquad \frac{\partial x_o}{\partial x_i} = -\frac{u\rho_i}{\rho_o(1-u)(1-\rho_\alpha v_\alpha)}\,,\\
&\frac{\partial \rho_o}{\partial(\nu_n/r_N)} = -\frac{3s(u)}{\rho_o(1-u)(1-\rho_\alpha v_\alpha)}\,, \qquad \frac{\partial x_o}{\partial(\nu_n/r_N)} = \frac{3s(u)x_o}{\rho_o(1-u)(1-\rho_\alpha v_\alpha)}\,,\\
&\frac{\partial \rho_o}{\partial u} = \frac{-\rho_i - 3s'(\nu_n/r_N) + 4\rho_\alpha + \rho_o(1-\rho_\alpha v_\alpha)}{(1-u)(1-\rho_\alpha v_\alpha)}\,,\\
&\frac{\partial x_o}{\partial u} = \frac{\rho_i(x_o - x_i) + 2\rho_\alpha(1-2x_o) + 3s' x_o \nu_n/r_N}{\rho_o(1-u)(1-\rho_\alpha v_\alpha)}\,,\\
&\frac{\partial \rho_o}{\partial \rho_\alpha} = \frac{\rho_o v_\alpha - 4}{1-\rho_\alpha v_\alpha}\,, \qquad\qquad \frac{\partial x_o}{\partial \rho_\alpha} = \frac{4x_o - 2)}{\rho_o(1-\rho_\alpha v_\alpha)}\,.
\end{aligned}
\tag{6.34}
$$

Here $s' = \partial s(u)/\partial u$.
The minimizations are :

$$\frac{\partial F}{\partial \rho_i} = 0 = u\left(\mu_{ni} - x_i\hat{\mu}_i - \mu_{no} + x_i\hat{\mu_o} + \frac{h_i}{A_o}(1-u)\mu_H\right) + \frac{8\pi}{5}(r_N x_i e)^2 \rho_i c(u)\,, \tag{6.35a}$$

$$\frac{\partial F}{\partial x_i} = 0 = u\rho_i(\hat{\mu_o} - \hat{\mu}_i) + \frac{8\pi}{5}(r_N \rho_i e)^2 x_i c(u) + h_i' \frac{\rho_i}{A_o} u(1-u)(\mu_H - T)\,, \tag{6.35b}$$

$$\frac{\partial F}{\partial r_N} = 0 = -\frac{3s(u)\sigma}{r_N^2} + \frac{8\pi}{5}(\rho_i x_i e)^2 r_N c(u)\,, \tag{6.35c}$$

$$\frac{\partial F}{\partial x} = 0 = \frac{3s(u)\sigma}{r_N}\left(\frac{\partial \sigma}{\partial x} + \nu_n \frac{\partial \mu_s}{\partial x}\right),, \tag{6.35d}$$

$$\frac{\partial F}{\partial(\nu_n/r_N)} = 0 = 3s(u)(\mu_s - \mu_{no})\,, \tag{6.35e}$$

$$\frac{\partial F}{\partial u} = 0 = \rho_i(f_{buli}(\rho_i, x_i, T) - \mu_{no} + x_i\hat{\mu_o}) + \frac{3s'}{r_N}\Big[\sigma + \nu_n(\mu_s - \mu_{no})\Big] + \frac{4\pi}{5}(\rho_i x_i r_N e)^2 c' + (1-2u)\frac{h_i\rho_i}{A_o}\mu_H + p_o + \rho_\alpha T\,, \tag{6.35f}$$

$$\frac{\partial F}{\partial \rho_\alpha} = 0 = (1-u)(\mu_\alpha - B_\alpha - 4\mu_{no} + 2\hat{\mu_o} + P_o v_\alpha)\,. \tag{6.35g}$$

Here $\hat{\mu} = \mu_n - \mu_p$, $h_i = h(x_i)$, $h_i' = \partial h(x_i)/\partial x_i$, and $c' = \partial c(u)/\partial u$.

Eq. (6.35c) represents the Nuclear virial theorem, that the surface energy equals twice the Coulomb energy. Solving for r_N yields

$$r_N^3 = \frac{15 s(u)\sigma}{8\pi(\rho_i x_i e)^2 c(u)}\,, \tag{6.36}$$

which can be written more succinctly as

$$r_N = \frac{9\sigma}{2\beta}\Big(\frac{s}{c}\Big)^{1/3}\,, \qquad \beta \equiv \left(\frac{243\pi}{5}\right)^{1/3}(\rho_i x_i \sigma e)^{2/3}\,. \tag{6.37}$$

Therefore r_N can be eliminated from the equilibrium equations. It should be noted that because of the Nuclear virial theorem, the total of the surface and Coulomb energy densities

is

$$f_{\rm surf} + f_{\rm Coul} = \beta(cs^2)^{1/3}\left(1 + \frac{2\mu_s\nu_n}{3\sigma}\right) \equiv \mathcal{D}(u)\left(1 + \frac{2\mu_s\nu_n}{3\sigma}\right), \tag{6.38}$$

where $\mathcal{D}(u)$ is defined [22]. The estimation of $\mathcal{D}(u)$ is described below.

Eq. (6.35e) proves the earlier statement that the neutron chemical potential of the surface μ_s should be equal to μ_{no}. Eq. (6.35d) also proves the earlier definition of the surface density of neutrons ν_n. Eq. (6.35g) determines the alpha particle density, reiterating that the alpha particles are in nuclear statistical equilibrium. The last term of Eq. (6.35g) represents an effective repulsive interaction for the alpha particles because of the excluded volume.

The remaining three equilibrium equations can be manipulated into the expected results concerning equilibrium among chemical potentials and pressure. Together with the conservation equations, the seven equations to be solved simultaneously are

$$A_1 = 0 = p_i - p_o - \rho_\alpha T - \beta\left(\mathcal{D}' - \frac{2\mathcal{D}}{3u}\right) + \frac{u\rho_i h_i}{A_o}\mu_H\,, \tag{6.39a}$$

$$A_2 = 0 = \mu_{ni} - \mu_{no} + \frac{1-u}{A_o}\Big[h_i\mu_H - h_i' x_i(\mu_H - T)\Big]\,, \tag{6.39b}$$

$$A_3 = 0 = \mu_{pi} - \mu_{po} + \frac{2\beta\mathcal{D}}{3\rho_i x_i u} + \frac{1-u}{A_o}\Big[h_i\mu_H + (1-x_i)h_i' x_i(\mu_H - T)\Big]\,, \tag{6.39c}$$

$$A_4 = 0 = ux_i\rho_i - \rho Y_p + (1-u)(\rho_{po} + r_p\rho_\alpha)\,, \tag{6.39d}$$

$$A_5 = 0 = u\rho_i - \rho + \frac{2\beta}{3\sigma}\mathcal{D}\nu_n + (1-u)\Big[\rho_{no} + \rho_{po} + (r_n + r_p)\rho_\alpha\Big]\,, \tag{6.39e}$$

$$\mu_s = \mu_{no}\,, \tag{6.39f}$$

$$\mu_\alpha = B_\alpha + 2\mu_{no} + 2\mu_{po} - p_o v_\alpha\,. \tag{6.39g}$$

We defined the useful abbreviations

$$r_n = 2 - \rho_{no}v_\alpha\,, \qquad r_p = 2 - \rho_{po}v_\alpha\,. \tag{6.40}$$

Note that the functions c and s could be completely replaced in Eq. (6.39) in favor of $\mathcal{D}$ because $3\mathcal{D}' = uc'/c + 2us'/s$. The nuclear equilibrium is determined only by the combination cs^2, or equivalently, by $\mathcal{D}$.

Eq. (6.39g) illustrates that μ_α, and hence ρ_α, is a function of ρ_{no} and ρ_{po} alone. In addition, σ and ν_n, which are functions of x, are also determinable from ρ_{no} and ρ_{po}, because of Eq. (6.39g). Therefore, it is necessary to simultaneously solve the 5 equations $A_i = 0$ and the two supplementary constraints. Note that it would have been inconsistent to evaluate σ and ν_n directly as functions of x_i, which seems the more straightforward procedure, because this does not ensure the full minimization of F.

6.5.2 Determination of Coulomb surface shape parameter $\mathcal{D}$

Following the work of Ravenhall et al.[58], one can identify the dependence of surface and Coulomb energies on the dimensionality d of the geometry. For $d = 3$, one has spheres of radius r_N, For $d = 2$, one has cylinders of radius r_N. For d=1, one has plates of thickness r_N. The surface and Coulomb energy densities of an isolated configuration with dimension d are then

$$f_{\rm surf} = \frac{ud\sigma}{r_N}\,, \qquad f_{\rm Coul} = \frac{4\pi}{5}(\rho_i x_o r_N e)^2 D_d(u) \tag{6.41}$$

where

$$D_d(u) = \frac{5}{d^2-4}\left[1 - \frac{d}{2}u^{1-2/d} + \frac{d-2}{2}u\right]\,. \tag{6.42}$$

In the case $d = 2$, the limit of D_d becomes

$$D_2(u) = \frac{5}{8}[u - 1 - \ln(u)]\,. \tag{6.43}$$

Thus, one has $s(u) = ud/3$ and $c(u) = uD_d(u)$. In the event of inside-out matter, one simply replaces u by $1 - u$ in these equations.

Both s and c depend upon d. The minimization of F with respect to r_N allows the elimination of r_N and the identification $f_{\rm surf} + f_{\rm Coul} = \beta\mathcal{D}$ implies that

$$\mathcal{D} = u\left(\frac{d^2 D_d(u)}{9}\right)^{1/3}\,. \tag{6.44}$$

The formulas Eq. (6.41) are valid for integer values of d , but gradual deformations between the integer states could be modeled by allowing d to vary [58]. The minimization of $f_{\rm surf} + f_{\rm Coul} = \beta\mathcal{D}$ with respect to d then implies that d is determined from minimization of $\mathcal{D}$, or equivalently $d^2 D_d$, at each value of u, subject to a maximum of 3 and a minimum of 1 for d. Fig. 6.8 shows the geometric factor $\mathcal{D}$. $\mathcal{D}$ does not depends on density so we can find a fitting function. Lattimer & Swesty [22] showed that a suitable approximation to this minimization, but also allowing for the possibility of inside-out matter, is obtained by using

$$\mathcal{D}(u) = u(1-u)\frac{(1-u)D_3^{1/3}(u) + uD_3^{1/3}(1-u)}{u^2 + (1-u)^2 + 0.6u^2(1-u)^2}\,. \tag{6.45}$$

6.5.3 Solving the equilibrium equations

There are seven equilibrium equations, including the two conservation equations for baryon number and charge, for seven variables, which can be taken to be $\rho_i, x_i, u, \rho_{no}, \rho_{po}, \rho_\alpha$ and x. Lattimer & Swesty [22] chose to reduce an analogous system by eliminating two variables with the conservation constraints. Even though we can reduce the number of equations to solve, we may probably meet numerical difficulties since, for example, the density of outside nucleons can be negative and code breaks. Thus, we do not eliminate the number of unknowns from the conservation properties but leave them to solve. However, as seen above,

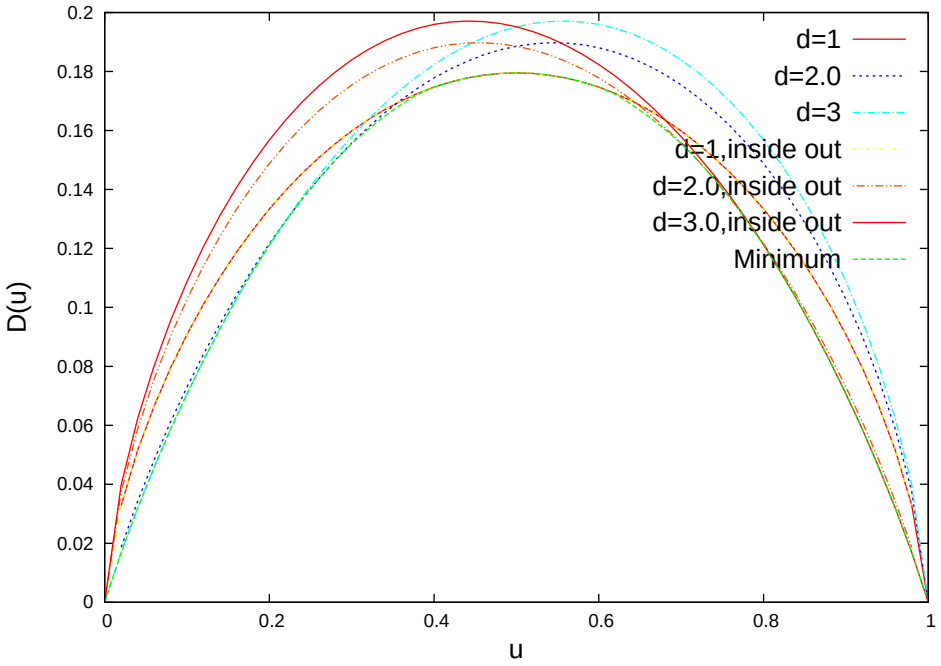

Figure 6.8: $\mathcal{D}$ as a function of u for given dimension($d = 1, 2, 3$). The minimum can be obtained the continuous change of d.

there are two trivial equilibrium conditions so that the variables $y_i = (\rho_\alpha, x)$ can be substituded in terms of ρ_{no} and ρ_{po}.

The most convenient form for the five dependent variables is
$z_i = (\rho_i, \ln \rho_{no}, \ln \rho_{po}, x_i, \ln u)$. The 'log' variables were introduced to prevent the variables from becoming negative. It also handles the accuracy of the small number.

Solutions are obtained via Newton-Raphson iteration, in which successive changes Δz_j in the independent variables z_j are found from the matrix equation (summing over repeated indices),

$$\Delta z_j = -(B_{ij})^{-1} A_i \,. \tag{6.46}$$

Here A_i is the vector of equations, defined in Eq. (6.39), to be zeroed, and

$$B_{ij} \equiv \left. \frac{\partial A_i}{\partial z_j} \right|_{y,\lambda} , \tag{6.47}$$

where $\lambda = (\rho, Y_p, T)$.

6.6 Result

As mentioned earlier in this chapter, our code is fast enough to generate an EOS table so we can easily compare EOS tables with different force models. The liquid droplet approach also

gives analytic derivatives of thermodynamic quantities. This means that we can guarantee the thermodynamic consistency compared with the Thomas-Fermi or Hartree-Fock approximation, in which thermodynamic derivatives can be obtained numerically. For these reasons, the liquid droplet approach is the most favorable method to make EOS tables.
For each point, we allow the independent variables change with small amounts of them since we use the previous solution of the variable set. By doing this, we can avoid code breaking and speed up the convergence. In the subroutine eos(ρ, T, Y_p) which consists of two subroutine, Newton-Rapshon code is to seek nucleons, alpha particle, and heavy nuclei (npaH) solution at first, if it does not converge, try to find nucleons and alpha particle (npa) solution, if it does not exist, nucleons (np) solution is to be found.
Now we present some of the result from our table [†].

6.6.1 Energy density and pressure

At zero temperature, the energy density and pressure is a function of density for both FRTFs and SLy4 since the Fermi-Dirac distribution function is frozen to 1 so we have a momentum density as a function of density, Eq (2.18, 2.36). For non-zero temperature, we need to calculate degeneracy parameters using interpolation or JEL scheme [12], then we can find energy density and pressure for given ρ, T, and Y_p.

6.6.2 Phase Boundaries

For a given density and proton fraction, the heavy nucleus dissolves into nucleons. This phenomenon corresponds to phase equilibrium and critical temperature. Simply, if the critical temperature of bulk equilibrium is high, the nucleus can exist in relatively high temperature. Fig. 6.9 shows the phase boundaries of hot dense matter for a given proton fraction (Y_p). In general in the region below the curve, there exist nucleons, alpha particle, and heavy nuclei (npaH). On the upper left region, nucleons exist with alpha particle. On the right region of the curve, only nucleons exist. FRTFs and SLy4 have the similar phase boundaries. In SLy4, nuclei exist larger range of density than FRTFs. Nuclei can exist at higher temperature in Truncated model because of higher critical temperature.

6.6.3 Atomic number in the heavy nuclei

The most stable nucleus on the earth is ^{56}Fe which has $Z = 26$. However, in the dense matter or neutron star crust, there are lots of nucleons and leptons outside, so the interaction among them may change the configuration of the most stable nuclei. Fig. 6.10 shows the atomic number as a function of density at given proton fraction ($Y_e = 0.45$) and temperature ($T = 0.726$ MeV). The phase transition in SLy4 has completed for large domain of density so the atomic number increase abruptly for narrow range of density. SLy4 always have a large number of protons in heavy nuclei for a given density, proton fraction, and temperature. In case of FRTF II, the atomic number is the smallest because of low surface tension.

[†]The result presented in this thesis is from beta version. We'll post them on the website soon after checking thermodynamic consistency.

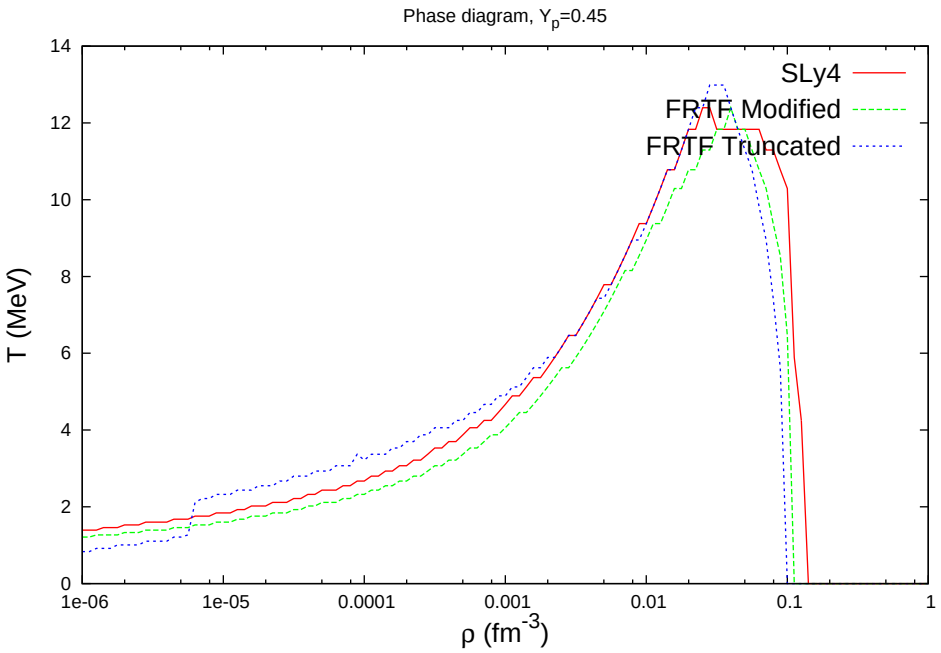

Figure 6.9: This figure shows the phase boundaries of dense matter when $Y_p = 0.45$.

6.7 Conclusions

The liquid droplet approach is the most promising method to generate thermodynamically consistent nuclear EOS table. The nuclear force model should be tested before making an EOS table so that the table represents both nuclear experiments on Earth and astrophysical observations.

To make the EOS consistent with the nuclear physics aspect, we have to use one nuclear force model to calculate the energy contribution from heavy nuclei, nucleons outside, and surface tension. In the thermodynamical sense, the derivatives in liquid droplet approach are written analytically and can be compared with numerical derivatives.

We treat electrons and photons separately since they interact weakly. But we add them to calculate total energy, pressure, entropy and their derivative with respect to temperature, density, and proton composition.
For finite temperature, we have to calculate the Fermi integral ($F_{1/2}$, $F_{3/2}$) to obtain number density and momentum density. The interpolation from the table cannot give enough accuracy at low temperature ($T \leq 1$ MeV). JEL is a successful scheme to give enough accuracy for all domains (relativistic vs. non-relativistic, degenerate and non-degenerate).
Phase transitions around half of nuclear saturation density ($1/2\rho_0$) can be achieved when we employ the geometric function $\mathcal{D}$ and changing the dimension d continuously.
We should be able to combine the liquid droplet approach with a relativistic mean field model in the near future if we handle the large L with acceptable values so new parameters

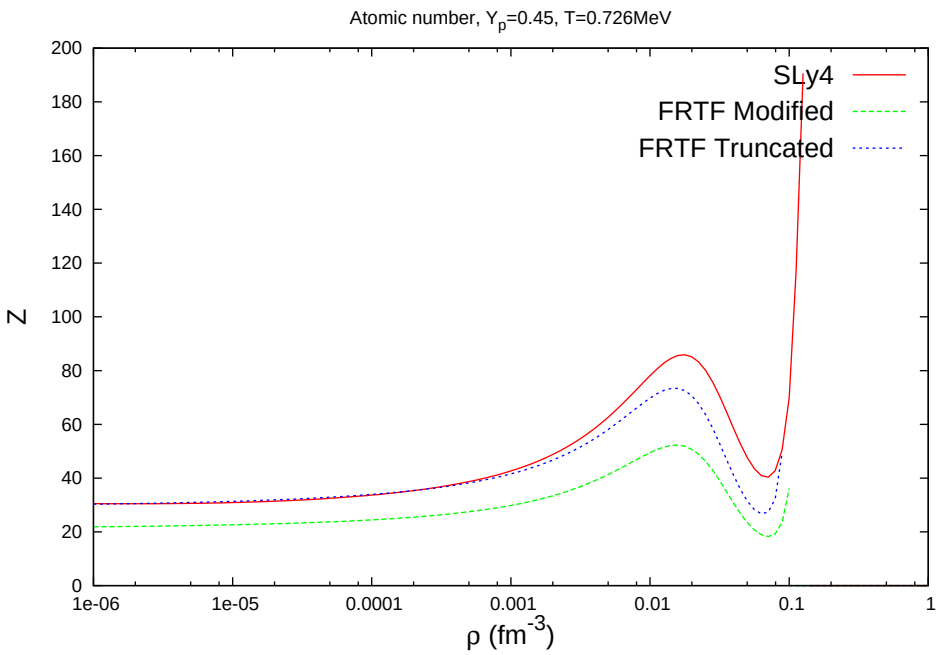

Figure 6.10: The atomic number increases as density increases in general. Around phase transition region, the atomic number drops and increases again.

in RMF can represent the allowed regions of mass and radius of neutron stars.

Chapter 7

Conclusions

The nuclear equation of state is needed to simulate supernovae explosions, proto-neutron stars, and compact binary mergers involving neutron stars. For these simulations, we need thermodynamic information for given baryon density, proton fraction, and temperature. Since the EOS should cover wide range of the above variables, we need to be careful when we choose a nuclear force model to make the EOS table. A good nuclear force model should represent both low and high densities nuclear phenomena as well as pure neutron and astrophysical matter.

First of all, we study nuclear physics using Finite Range force model. In the Finite Range force model, the nuclear interaction energy at density each point has the contribution from every spacial point with weight factor ($e^{-r/a}$). The first model that we investigated is the truncated model (Chapter 2). To find the parameters in the truncated model, we use the standard nuclear matter properties of symmetric nuclear matter , such as $E/A = -B \simeq -16$ MeV, $P = 0$ MeV/fm^3, $S_v \simeq 32$ MeV, $L \simeq 60$MeV. a, which is a nuclear diffuseness parameter can be obtained from semi-infinite nuclear matter calculation. This truncated model is improved by adding new density dependent interactions to fit optical potential, nuclear incompressibility, and pure neutron matter. To get optimized parameter set for the modified model, we compare the results of total binding energy of single nucleus from the modified model with experimental values. The recent constraints of S_v and L [47] confirm that our parameter set for the modified model is a good choice.

Both the truncated and modified models model are used to calculate energy per baryon of single nucleus and heavy nuclei in dense matter. Since the finite range model gives integral equations instead of differential equations, the boundary condition has no difficulty and the numerical calculation in the unit (Wigner-Seitz) cell is much easier to perform than differential equations. Thomas-Fermi approximation is employed to find the nuclear density profile. In TF, we are seeking the local density at each point instead of finding the full wave functions. From the density profile, we find the plane wave so that we are able to calculate momentum density to calculate Hamiltonian density or kinetic energy. At zero temperature, the relation between the number density and momentum density is simple since the Fermi-Dirac distribution function is frozen to 1. At finite temperature, however, we have to calculate the Fermi integral which is not an analytic function. For example, from the number density, we are supposed to find the degeneracy parameter (ϕ) from Fermi integral, $F_{3/2}(\phi)$ and to get the momentum density from Fermi integral, $F_{5/2}(\phi)$. JEL scheme provides polynomial fits

for Fermi integral. This fitting function has remarkably high accuracies to calculate Fermi integral. We employ JEL scheme to calculate nuclear force at finite temperature.

To find the density profile of nuclei, we use Euler-Lagrange equations to minimize total binding energy, and it gives that $\mu_{n,i}$ and $\mu_{p,i}$ are constant in the cell if we set the density at each grid point as unknown. The multi-dimensional Newton-Raphson method is used to solve the equations. If the initial guess is good enough, the number of iterations to get solutions is only two or three so the code is fast enough to calculate binding energy of all nuclei present on earth.

The bulk equilibrium calculation is an example of using JEL scheme. Bulk (dense-dilute) matter equilibrium is the simplified case of heavy nuclei in dense matter. That is, if bulk equilibrium is possible, that suggests there might be a phase of heavy nuclei in dense matter. If bulk equilibrium does not exist, there would be uniform nuclear matter phase for given density, proton fraction, and temperature. The conditions for bulk equilibrium are made by minimizing the total free energy density, which are $P_I = P_{II}$, $\mu_{nI} = \mu_{nII}$, and $\mu_{pI} = \mu_{pII}$. $I(II)$ represent dense (dilute) phase. From phase equilibrium calculations, we can get the critical temperature in which both phases have the same density and proton fraction. Beyond the critical temperature, phase equilibrium does not exist any more. Semi-infinite nuclear matter density profile is obtained from the finite range force models. Since the curvature effect of finite nuclei is small, the semi-infinite nuclear matter calculation is used to find the surface tension for nuclei. With the critical temperature from phase equilibrium, semi-infinite calculation gives analytic fitting function for surface tension formula ($\omega = \omega(x, T)$).

The importance of choosing of nuclear force model to make EOS table can also be seen when we study neutron star crust. The nuclear potentials have a lot of different form. These difference does not effect the pressure, energy density, and atomic number in neutron star crust. If we extend the potentials, however, to high density, the difference in the mass-radius relation of neutron stars is apparent.

Using the finite-range model with liquid droplet approach, we build EOS table for astrophysical simulations. Thomas-Fermi and Hartree (Fock) approximation gives only numerical quantities of thermodynamic quantities. On the other hand, liquid droplet approach gives analytic thermodynamic quantities, that means thermodynamic consistency. Compared to LS EOS and LPRL [17], our LDM approach contains neutron skins and surface diffuseness to improve the liquid droplet formalism. The LDM approach is fast to build the full EOS table so that we can manipulate different nuclear force model without difficulty and we can make an EOS table with a large number of grid points. The atomic number at the lower density region ($\simeq 0.01/\mathrm{fm}^3$) remains around 30 and has experienced abrupt changes between the phase transition regions ($0.5\rho_0$). This is a general feature in both the non-relativistic mean field model and relativistic mean field model. In the phase transition region, the atomic number from RMF models is an order of magnitude greater than the one from the non-relativistic potential models. Between SLy4 and finite range force model, the phase transition to uniform matter happens later in SLy4. Since the truncated model has the higher critical temperature than SLy4 and the modified model, nuclei can exist in higher temperature in the truncated model.

It is necessary to compare the EOS tables using the same nuclear force model but with different numerical techniques (LDM, TF, HF) to see how similar the each EOS table would be. This work will be begun in the near future.

Bibliography

[1] Barranco, M. & Buchler, J. R. 1980, Phys. Rev. **C22**, 1729.

[2] Baym, G., Bethe, H. A. & Pethick, C. J. 1971 Nucl. Phys. **A175**, 225.

[3] Blaizot, J. P. 1980, Phys. Rep. **64**, 171.

[4] Blaizot, J. P., Gogny, D. & Grammaticos, B. 1976, Nucl. Phys. **A265**, 315.

[5] Bonche, P. & Vautherin, D. 1981, Nucl. Phys. **A372** 496.

[6] Buchler, J. R. & Barranco, M. 1980, J. de Phys. **41**, C2-31.

[7] Danielewicz, P. 2003, Nucl. Phys. **A727**, 233.

[8] Eggleton, P. P., Faulkner, J. & Flannery, B. P. 1973, A & A. **23**, 325.

[9] Glendenning, N. K. & Csernai, L. P. & Kapusta, J. I. 1985, Phys. Rev. **C33**, 1299.

[10] Horowitz, C. J. & Piekarewicz 2001, Phys. Rev. Lett. **86**, 5647.

[11] Horowitz, C. J., Pollock, S. J., Sonder, P. A. & Michaels, R. 2001, Phys. Rev. **C63** 025501.

[12] Johns, S. M., Ellis, P. J. & Lattimer, J. M. 1996, Ap. J. **473**, 1020.

[13] Kolehmainen, K., Prakash, M. & Lattimer, J. M. 1985, Nucl. Phys. **A439**, 535.

[14] Küpper, W. A., Wegmann, G. & Hilf, E. R. 1974, A & A **88**, 454.

[15] Lamb, D. Q., Lattimer, J. M., Pethick, C. J. & Ravenhall, D. G. 1978, Phys. Rev. Lett. **41**, 1623.

[16] Lamb, D. Q., Lattimer, J. M., Pethick, C. J. & Ravenhall, D. G. 1981, Nucl. Phys. **A360**, 459.

[17] Lattimer, J. M., Pethick, C. J., Ravenhall, D. G. & Lamb, D. Q. 1985, Nucl. Phys. **A432**, 646.

[18] J. Xu, L.W. Chen, B.A. Li, and H.R. Ma, Phys. Rev. **C79** (2009) 035802

[19] Lattimer, J. M. & Prakash, M. 2007, Phys. Rep. **442**, 109.

[20] C.J. Pethick and D.G. Ravenhall, Ann. Rev. Nucl. Part. Sci. **45** (1995) 429

[21] Lattimer, J. M. & Ravenhall, D. G. 1978, ApJ. **223**, 314.

[22] Lattimer, J. M. & Swesty, F. D. 1991, Nucl. Phys. **A535**, 331.

[23] Müller, H. & Serot, B. D. 1995, Phys. Rev. **C52**, 2072.

[24] Myers, W. D. & Swiatecki, W. J. 1969, Ann. Phys. (N.Y.) **55**, 395.

[25] Myers, W. D. & Swiatecki, W. J. 1973, Ann. Phys. (N.Y.) **84**, 186.

[26] Myers, W. D. & Swiatecki, W. J. 1990, Ann. Phys. (N.Y.) **204**, 401.

[27] Myers, W. D. & Swiatecki, W. J. 1991, Ann. Phys. (N.Y.) **211**, 292.

[28] Negele, J. W. and Vautherin, D. 1973, Nucl. Phys. **A207**, 298.

[29] Ravenhall, D. G., Pethick, C. J. & Lattimer, J. M. 1983, Nucl. Phys. **A407**, 571.

[30] Seyler, R. G. & Blanchard, C. H. 1961, Phys. Rev. **124**, 227.

[31] Seyler, R. G. & Blanchard, C. H. 1963, Phys. Rev. **131**, 355.

[32] Steiner, A. W., Praksh, M., Lattimer, J. M. & Ellis, P. 2005, Phys. Rep. **411**, 325.

[33] Swesty, F. D., Lattimer, J. M. & Myra, E. S. 1994, ApJ. **425**, 1955.

[34] W. Greiner and J.A. Maruhn, *Nuclear models*(Springer, 1989)

[35] A. Akmal, V. R. Pandharipande, and D. G. Ravenhall, Phys. Rev. **C58** (1998) 1804

[36] J.W. Negele and H. Orland *Quantum Many-Particle Systems* (Addison-Wesley, 1987)

[37] N.K. Glendenning *Compact stars*(Springer, 2nd Edition)

[38] S.L. Shapiro and S.A. Teukolsky *Black Holes, White Dwarfs, and Neutron Stars*(John Wiley & Sons, 1983)

[39] J.M. Lattimer, *Personal note*

[40] A. Burrows and J.M. Lattimer, ApJ. **307** (1986) 178

[41] K. Oyamatsu, Nucl. Phys. **A561** (1993) 431

[42] F. Douchin and P. Haensel, A&A. **151** (2001) 380

[43] J.M. Lattimer and B.F. Schutz, ApJ. **629 (2005) 979**

[44] K. Hebeler and A. Schwenk, Phys. Rev. C82, 014314 (2010)

[45] G. Audi, A. H. Wapstra, and C. Thibault, Nucl. Phys. A729, 337 (2003).

[46] M. Kortelainen, T. Lesinski, J. Mor, W. Nazarewicz, J. Sarich, N. Schunck, M. V. Stoitsov, and S. Wild3, Phys. Rev. C82, 024313 (2010)

[47] J. M. Lattimer and Y. Lim, arXiv:1203.4286

[48] L.-W. Chen et al., Phys. Rev. C82, 024321 (2010)

[49] L. Trippa, G. Col and E. Vigezzi, Phys. Rev. C77, 061304 (2008)

[50] J. G. Hirsch, C. Barbero, A. E. Mariano, arXiv:1108.0707

[51] M. B. Tsang et al., Phys. Rev. Lett. 102, 122701 (2009).

[52] A. Tamii et al., Phys. Rev. Lett. 107, 062502 (2011).

[53] A. W. Steiner, J. M. Lattimer and E. F. Brown, ApJ. 722, 33 (2010)

[54] K. Hebeler, J. M. Lattimer, C. J. Pethick and A. Schwenk, Phys. Rev. Lett. 105, 161102 (2010)

[55] S. Gandolfi, J. Carlson and S. Reddy, Phys. Rev. C, in press; arXiv:1101.1921 (2012).

[56] J.M. Lattimer, *The Nuclear Equation of State and Supernovae*, in Nuclear Equation of State, ed. A. Ansari & L. Satpathy (World Scientific, Singapore) , pp. 83-208 (1996)

[57] P.B. Demorest et al., Nature, 467, 1081 (2010)

[58] D. G. Ravenhall, C. J. Pethick, and J. R. Wilson, Phys. Rev. Lett, 50, 2066 (1983)

[59] H. Shen, H.Toki, K.Oyamatsu, and, K.Sumiyoshi, Nucl. Phys. A637, 435 (1998)

[60] H. Shen, H.Toki, K.Oyamatsu, and, K.Sumiyoshi, ApJ. 197 (2011) 20

[61] G. Shen, C. J. Horowitz, and S. Teige, Phys. Rev. C82, 015806, (2010)

[62] G. Glen and P. Sutherland, ApJ. 239, 671 (1980)

[63] Matthias Hempel and Jrgen Schaffner-Bielich, arXiv:0911.4073

[64] M. Hempel, T. Fischer, J. Schaffner-Bielich, and M. Liebendrfer, ApJ. 748, (2012) 70

[65] S.I. Blinnikov, I.V. Panov, M.A.Rudzsky , and K. Sumiyoshi, A & A 535 (2011) A37

[66] S. Furusawa, S. Yamada, K. Sumiyoshi, and H. Suzuki, ApJ. 738 (2011) 178F

[67] D.G. Yakovlev, G. Baym, P. Hanse, and C.J. Pethick, *Landau and Neutron stars*, presentation, (2008)

Appendix A

Finite Range Integration

In the Yukawa type finite range force mode, one has

$$\widetilde{g(r_1)} = \int d^3r_2 f(r_{12}/a) g(r_2) = \int d^3r_2 \frac{1}{4\pi r_{12} a^2} e^{-r_{12}/a} g(r_2)\,. \tag{A.1}$$

This integration is not converged easily. The integration which involves
$\int f(x)e^{-x}\,dx$ has $\sim 1/N^2$ convergence properties, where N is number of grid points. Mathematically, we can increase N as much as possible, but the number of times to calculate the integration increases as $\sim N^2$ and the current ability of cpu may have numerical noise when we increase the number of grid points.
One way to solve the convergence issues is to use mathematical induction, or, geometric sequence. That is, the the error between $\tilde{g}_N$ and $\tilde{g}_{2N}$ decreases as

$$\tilde{g}_{2N} - \tilde{g}_N = \Delta\,, \quad \tilde{g}_{4N} - \tilde{g}_{2N} = \frac{1}{4}\Delta\,, \quad \tilde{g}_{8N} - \tilde{g}_{4N} = \frac{1}{16}\Delta\,, \ldots \tag{A.2}$$

Thus we may have

$$\tilde{g}_\infty = \tilde{g}_N + \Delta + \frac{1}{4}\Delta + \frac{1}{16}\Delta + \cdots = \tilde{g}_N + \frac{4}{3}\Delta = \frac{4}{3}\tilde{g}_{2N} - \frac{1}{3}\tilde{g}_N\,. \tag{A.3}$$

This induction shows enough accuracies when $N = 50$ and $N = 100$ for given Wigner seitz cell(12fm). However, we need to calculate the integration twice to complete the convergence. Now, we show the more efficient method to calculate this Yukawa type integration.

A.1 Taylor expansion integration

The integrand in the Yukawa integration is expand to take into account the variation between r and $r+\Delta$. For example, for given interval $(r_i, r_i+\delta)$,

$$\begin{aligned} f(r) =& f(r_i) + f'(r_i)(r-r_i) + \frac{1}{2}f''(r_i)(r-r_i)^2 + \frac{1}{3!}f^{(3)}(r_i)(r-r_i)^3 + \cdots \\ =& f_i + \frac{f_{i+1}-f_{i-1}}{2\Delta}(r-r_i) + \frac{f_{i+1}-2f_i+f_{i-1}}{2\Delta^2}(r-r_i)^2 + \cdots . \end{aligned} \tag{A.4}$$

By doing this, we can eliminate the contamination in the integral between r_i and r_{i+1} when we use simple trapezoid rule ($\int_i^{i+1} f(x)dx = \frac{1}{2}\Delta(f_i + f_{i+1})$).

A.1.1 1D plane parallel nuclear matter

The study of 1D parallel (semi-infinite) nuclear matter sheds light on how the surface tension changes for a given temperature and proton fraction. In the semi-infinite nuclear matter, without loss of generality, we can say $g(r) = g(x,y,z) = g(z)$. Then the original finite range integration becomes

$$\tilde{g}(z_o) = \int_{-\infty}^{\infty} dx \int_{-\infty}^{\infty} dy \int_{-\infty}^{\infty} dz \frac{e^{-\sqrt{x^2+y^2+(z-z_o)^2}/a}}{4\pi a^2\sqrt{x^2+y^2+(z-z_o)^2}}\, g(z). \tag{A.5}$$

Changing variables, $x^2+y^2=\rho^2$, $\int dx \int dy = 2\pi \int \rho\, d\rho$ give

$$\begin{aligned} \tilde{g}(z_o) =& \frac{1}{2}\int_{-\infty}^{\infty} dz g(z) \int_0^{\infty} \frac{e^{-\sqrt{\rho^2+(z-z_o)^2}/a}}{a^2\sqrt{\rho^2+(z-z_o)^2}}\, g(z) \\ =& \frac{1}{2a}\int_{-\infty}^{\infty} dz g(z)(-)e^{-\sqrt{\rho^2+(z-z_o)^2}/a}\Big|_{\infty}^{0} \\ =& \frac{1}{2a}\int_{-\infty}^{\infty} dz g(z) e^{-|z-z_o|/a} \end{aligned} \tag{A.6}$$

With the above general equation in 1D plane parallel case, we apply Taylor expansion for smooth distance dependent function u.

$$\tilde{u}(z) = \frac{1}{2a}\left[\int_{-\infty}^{z} u(z')e^{(z'-z)/a}\, dz' + \int_z^{\infty} u(z')e^{(z-z')/a}\, dz'\right] \equiv u^-(z) + u^+(z) \tag{A.7}$$

This equation can be calculated by iteration scheme.

$$\begin{aligned} u_{i+1}^- =& \frac{1}{2a}\int_{-\infty}^{z_{i+1}} u(z')e^{(z'-z_{i+1})/a}\,dz' \\ =& \frac{1}{2a}\int_{-\infty}^{z_i} u(z')e^{(z'-z_i)/a}e^{-\Delta/a}\,dz' + \frac{1}{2a}\int_{z_i}^{z_{i+1}} u(z')e^{(z'-z_{i+1})/a}\,dz' \\ =& e^{-\Delta/a}u_i^- + \frac{1}{2a}\int_{z_i}^{z_{i+1}} u(z)e^{(z-z_{i+1})/a}\,dz\,. \end{aligned} \tag{A.8}$$

For the integration at the end, we expand

$$u(z) = u_i + \frac{u_{i+1}-u_i}{\Delta}(z-z_i) + O(\Delta^2) \tag{A.9}$$

then we have

$$u_{i+1}^- = fu_i^- + I_0^- u_i + I_1^- u_{i+1}\,, \tag{A.10}$$

where

$$\begin{aligned} f =& e^{-\Delta/a} \\ I_0^- =& \frac{1}{2a}\int_0^\Delta \Big(1-\frac{z}{\Delta}\Big)e^{z/a}e^{-\Delta/a}\,dz = \frac{a-(a+\Delta)e^{-\Delta/a}}{2\Delta} \\ I_1^- =& \frac{1}{2a}\int_0^\Delta \frac{z}{\Delta}e^{z/a}e^{-\Delta/a}\,dz = \frac{\Delta-a+ae^{-\Delta/a}}{2\Delta}\,. \end{aligned} \tag{A.11}$$

In the same manner, we have an equation for u_i^+,

$$\begin{aligned} u_i^+ =& \frac{1}{2a}\int_{z_i}^{\infty} u(z')e^{(z_i-z')/a}\,dz' \\ =& \frac{1}{2a}\int_{z_i}^{z_{i+1}} u(z')e^{(z_i-z')/a}\,dz' + \frac{1}{2a}\int_{z_{i+1}}^{\infty} u(z')e^{(z_{i+1}-z')/a}e^{-\Delta/a}\,dz' \\ =& \frac{1}{2a}\int_{z_i}^{z_{i+1}} u(z)e^{(z_i-z)/a}\,dz + e^{-\Delta/a}u_{i+1}^+\,. \end{aligned} \tag{A.12}$$

With the first order Taylor expansion before, we have

$$u_i^+ = fu_{i+1}^+ + I_0^+ u_i + I_1^+ u_{i+1}\,, \tag{A.13}$$

where

$$\begin{aligned} I_0^+ =& \frac{1}{2a}\int_0^\Delta \Big(1-\frac{z}{\Delta}\Big)e^{-z/a}\,dz' = I_1^- \\ I_1^+ =& \frac{1}{2a}\int_0^\Delta \frac{z}{\Delta}e^{-z/a}\,dz' = I_0^-\,. \end{aligned} \tag{A.14}$$

As a second order expansion, we have

$$u(z) = u_i + \frac{u_{i+1}-u_{i-1}}{2\Delta}(z-z_i) + \frac{u_{i+1}-2u_i+u_{i-1}}{2\Delta^2}(z-z_i)^2 + O(\Delta^3) \tag{A.15}$$

then

$$u^-_{i+1} = f u^-_i + J^-_0 u_{i-1} + J^-_1 u_i + J^-_2 u_{i+1} \tag{A.16}$$

where

$$\begin{aligned}
J^-_0 =& \frac{1}{2a} e^{-\Delta/a} \int_0^\Delta \Big(-\frac{z}{2\Delta} + \frac{z^2}{2\Delta^2}\Big) e^{z/a}\, dz = \frac{2a^2 - a\Delta - a(2a+\Delta)e^{-\Delta/a}}{4\Delta^2} \\
J^-_1 =& \frac{1}{2a} e^{-\Delta/a} \int_0^\Delta \Big(1 - \frac{z^2}{\Delta^2}\Big) e^{z/a}\, dz = \frac{-2a^2 + 2a\Delta + (2a^2 - \Delta^2)e^{-\Delta/a}}{2\Delta^2} \\
J^-_2 =& \frac{1}{2a} e^{-\Delta/a} \int_0^\Delta \Big(\frac{z}{2\Delta} + \frac{z^2}{2\Delta^2}\Big) e^{z/a}\, dz = \frac{2a^2 - 3a\Delta + 2\Delta^2 - a(2a-\Delta)e^{-\Delta/a}}{4\Delta^2}\,.
\end{aligned} \tag{A.17}$$

For u^+_i,

$$u^+_i = f u^+_{i+1} + J^+_0 u_{i-1} + J^+_1 u_i + J^-_2 u_{i+1}\,, \tag{A.18}$$

where

$$\begin{aligned}
J^+_0 =& \frac{1}{2a} \int_0^\Delta \Big(-\frac{z}{2\Delta} + \frac{z^2}{2\Delta^2}\Big) e^{-z/a}\, dz = \frac{2a^2 - a\Delta - a(2a+\Delta)e^{-\Delta/a}}{4\Delta^2} = J^-_0 \\
J^+_1 =& \frac{1}{2a} \int_0^\Delta \Big(1 - \frac{z^2}{\Delta^2}\Big) e^{-z/a}\, dz = \frac{\Delta^2 - 2a^2}{2\Delta^2} + \frac{a(a+\Delta)e^{-\Delta/a}}{\Delta^2} \\
J^-_2 =& \frac{1}{2a} \int_0^\Delta \Big(\frac{z}{2\Delta} + \frac{z^2}{2\Delta^2}\Big) e^{-z/a}\, dz = \frac{2a^2 + a\Delta - (2\Delta^2 + 3a\Delta + 2\Delta^2)e^{-\Delta/a}}{4\Delta^2}\,.
\end{aligned} \tag{A.19}$$

For this second order expansion, we have to be careful for u^-_1 and u^+_{N-1}, which will be

$$u^-_1 = f u^-_0 + I^{-1}_0 u_0 + I^{-1}_1 u_1 u^+_{N-1} = f u^N_0 + I^+_0 u_{N-1} + I^+_1 u_N \tag{A.20}$$

because there will be no second order derivatives at $i = 1$ and $i = N - 1$.
For the test of accuracy of this tilde equation, we now compare analytic solution of $u(z) = \frac{1}{1+e^{z/a}}$ where a is chosen as 1 fm for the test problem.

$$\tilde{u}(z) = \frac{1}{2}\left(1 + \frac{z}{a} e^{z/a}\right) - \frac{1}{2}(e^{z/a} - e^{-z/a}) \ln(1 + z/a)\,. \tag{A.21}$$

Fig A.1.1 shows the error between the analytic solution and the numerical calculation. This confirms that the second order expansion gives enough accuracy for integration technique.

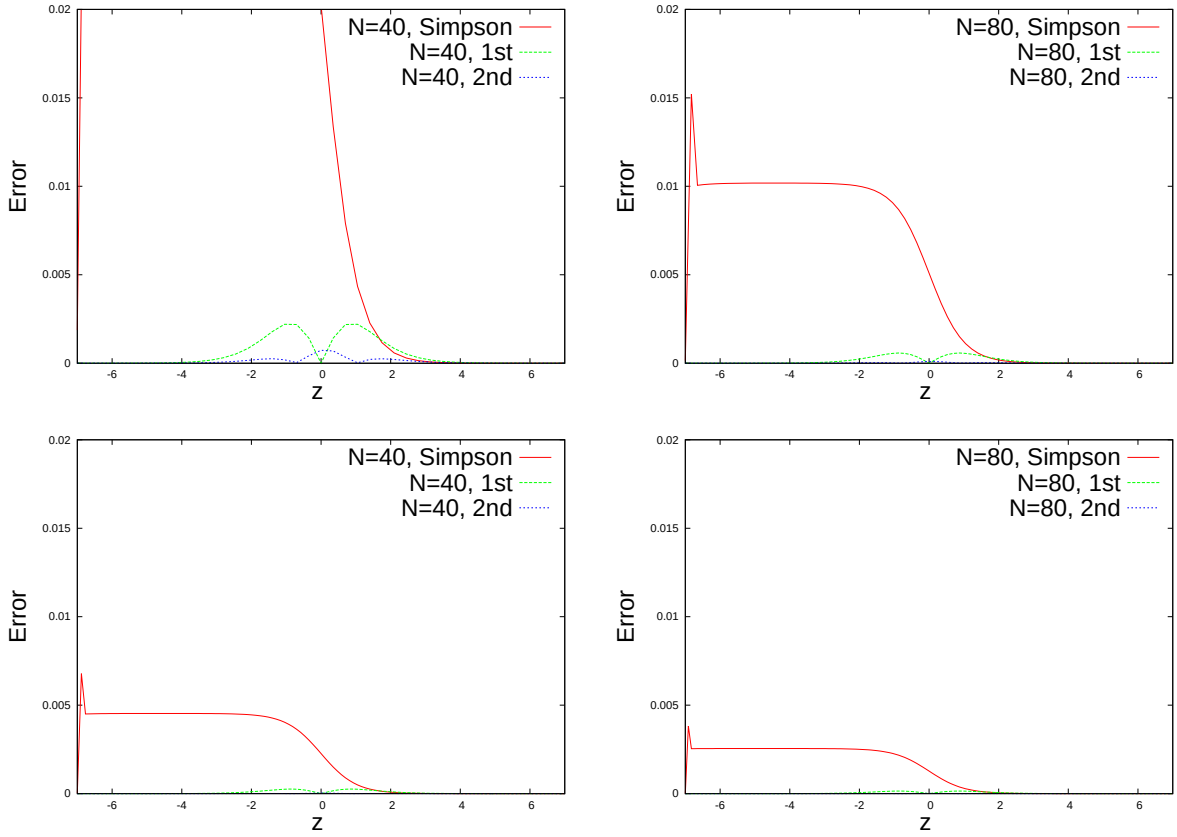

Figure A.1: The error between analytic solution and numerical calculation. The red (green, blue) one represent the absolute error between analytic solution and trapezoidal (1st, 2nd Taylor expansion) numerical integration. N is the number of zone in the given domain (-6,6) The error decrease as N increases. The error from 2nd order expansion is always smaller than any others.

A.1.2 3D radial symmetric nuclear matter

In the symmetric nuclei or nuclei with neutron gas matter, we need to calculate

$$\begin{aligned}\widetilde{g(r_1)} &= \int d^3r_2 f(r_{12}/a)g(r_2) \\ &= \frac{1}{2ar_1}e^{-r_1/a}\int_0^{r_1} g(r)r\left(e^{r/a}-e^{-r/a}\right)dr \\ &+ \frac{1}{2ar_1}\left(e^{r_1/a}-e^{-r_1/a}\right)\int_{r_1}^{R} g(r)re^{-r/a}dr \\ &+ \frac{1}{2ar_1}\left(e^{r_1/a}-e^{-r_1/a}\right)\int_{R}^{\infty} g(r)re^{-r/a}dr\,.\end{aligned} \tag{A.22}$$

The last integration represents the effect from out side nucleons. We now address the coefficient from the second order Taylor expansion method.

We separate the two integrals as in the 1D semi-infinite nuclear matter,

$$\widetilde{g(r)} = \tilde{g}^{(-)}(r) + \tilde{g}^{(+)}(r) + \frac{1}{2r}\Big(e^{r/a} - e^{-r/a}\Big)e^{-R/a}(a+R)g(R)\,. \tag{A.23}$$

There is no difference in the finite range integration between finite nuclei and nuclei in dense matter except the final tail term.
The discrete integration for $\tilde{g}^{(-)}(r_{i+1})$ has the form of

$$\begin{aligned}\tilde{g}^{(-)}(r_{i+1}) &= \frac{1}{2ar_{i+1}}e^{-r_{i+1}/a}\sum_{k=0}^{i}\int_{r_k}^{r_{k+1}} g(r)r(e^{r/a} - e^{-r/a})dr \\ &= f_i^{(-)}\tilde{g}^{(-)}(r_i) + \frac{1}{2a(r_i+\Delta)}e^{-(r_i+\Delta)/a}\int_{r_i}^{r_i+\Delta} g(r)r(e^{r/a} - e^{-r/a})dr\,,\end{aligned} \tag{A.24}$$

where $f_i^{(-)}$ is given by

$$f_i^{(-)} = \frac{r_i}{r_i+\Delta}e^{-\Delta/a}\,. \tag{A.25}$$

The right hand side integration can be extended by

$$g(r) = g_i + \frac{g_{i+1} - g_{i-1}}{2\Delta}(r - r_i) + \frac{g_{i+1} - 2g_i + g_{i-1}}{2\Delta^2}(r - r_i)^2\,. \tag{A.26}$$

We use the $g_i' = \frac{g_{i+1}-g_{i-1}}{2\Delta}$, since this expansion has higher order ($O(\Delta^3)$) error than the forward ($f_i' = (f_{i+1} - f_i)/\Delta$) and backward ($f_i' = (f_i - f_{i-1})/\Delta$) error ($O(\Delta^2)$).
We can find coefficients which correspond to each g_{i-1}, g_i, and g_{i+1} through the integration so that

$$\begin{aligned}\tilde{g}_{i+1}^{(-)} &= f_i^{(-)}\tilde{g}_i^{(-)} + w_{1i}g_{i-1} + w_{2i}g_i + w_{3i}g_{i+1} - w_{4i}g_{i-1} - w_{5i}g_i - w_{6i}g_{i+1} \\ &= f_i^{(-)}\tilde{g}_i^{(-)} + (w_{1i} - w_{4i})g_{i-1} + (w_{2i} - w_{5i})g_i + (w_{3i} - w_{6i})g_{i+1}\end{aligned} \tag{A.27}$$

where

$$
\begin{aligned}
w_{1i} &= \frac{1}{2a(r_i+\Delta)} e^{-(r_i+\Delta)/a} \int_{r_i}^{r_i+\Delta} \left[-\frac{(r-r_i)}{2\Delta} + \frac{(r-r_i)^2}{2\Delta^2} \right] r e^{r/a}\, dr\,, \\
w_{2i} &= \frac{1}{2a(r_i+\Delta)} e^{-(r_i+\Delta)/a} \int_{r_i}^{r_i+\Delta} \left[1 - \frac{(r-r_i)^2}{\Delta^2} \right] r e^{r/a}\, dr\,, \\
w_{3i} &= \frac{1}{2a(r_i+\Delta)} e^{-(r_i+\Delta)/a} \int_{r_i}^{r_i+\Delta} \left[\frac{(r-r_i)}{2\Delta} + \frac{(r-r_i)^2}{2\Delta^2} \right] r e^{r/a}\, dr\,, \\
w_{4i} &= \frac{1}{2a(r_i+\Delta)} e^{-(r_i+\Delta)/a} \int_{r_i}^{r_i+\Delta} \left[-\frac{(r-r_i)}{2\Delta} + \frac{(r-r_i)^2}{2\Delta^2} \right] r e^{-r/a}\, dr\,, \\
w_{5i} &= \frac{1}{2a(r_i+\Delta)} e^{-(r_i+\Delta)/a} \int_{r_i}^{r_i+\Delta} \left[1 - \frac{(r-r_i)^2}{\Delta^2} \right] r e^{-r/a}\, dr\,, \\
w_{6i} &= \frac{1}{2a(r_i+\Delta)} e^{-(r_i+\Delta)/a} \int_{r_i}^{r_i+\Delta} \left[\frac{(r-r_i)}{2\Delta} + \frac{(r-r_i)^2}{2\Delta^2} \right] r e^{-r/a}\, dr\,.
\end{aligned}
\tag{A.28}
$$

Each w_i can be obtained

$$
\begin{aligned}
w_{1i} &= \frac{ae^{-\Delta/a}}{4\Delta^2(\Delta+r_i)}\Big[6a^2+2a\Delta-2ar_i-\Delta r_i \\
&\qquad\qquad -e^{\Delta/a}\Big(6a^2+\Delta(\Delta+r_i)-2a(2\Delta+r_i)\Big)\Big]\,, \\
w_{2i} &= \frac{e^{-\Delta/a}}{2\Delta^2(\Delta+r_i)}\Big[-6a^3+a\Delta^2+2a^2r_i-\Delta^2r_i \\
&\qquad\qquad +2ae^{\Delta/a}\Big(3a^2+\Delta(\Delta+r_i)-a(3\Delta+r_i)\Big)\Big]\,, \\
w_{3i} &= \frac{e^{-\Delta/a}}{4\Delta^2(\Delta+r_i)}\Big[6a^3+a\Delta r_i-2a^2(\Delta+r_i) \\
&\qquad\qquad -e^{\Delta/a}\Big(6a^3-2\Delta^2(\Delta+r_i)-2a^2(4\Delta+r_i)+a\Delta(5\Delta+3r_i)\Big)\Big]\,, \\
w_{4i} &= \frac{ae^{-2(r_i+\Delta)/a}}{4\Delta^2(\Delta+r_i)}\Big[-6a^2-\Delta(\Delta+r_i)-2a(2\Delta+r_i) \\
&\qquad\qquad +e^{\Delta/a}\Big(6a^2-\Delta r_i+2a(-\Delta+r_i)\Big)\Big] \\
w_{5i} &= \frac{e^{-2(r_i+\Delta)/a}}{2\Delta^2(\Delta+r_i)}\Big[e^{\Delta/a}\Big(-6a^3+a\Delta^2-2a^2r_i+\Delta^2r_i\Big) \\
&\qquad\qquad +2a\Big(3a^2+\Delta(\Delta+r_i)+a(3\Delta+r_i)\Big)\Big]\,, \\
w_{6i} &= \frac{e^{-2(r_i+\Delta)/a}}{4\Delta^2(\Delta+r_i)}\Big[ae^{\Delta/a}\Big(6a^2+\Delta r_i+2a(\Delta+r_i)\Big) \\
&\qquad\qquad -\Big(6a^3+2\Delta^2(\Delta+r_i)+2a^2(4\Delta+r_i)+a\Delta(5\Delta+3r_i)\Big)\Big]\,.
\end{aligned}
\tag{A.29}
$$

In the same manner, we have

$$
\begin{aligned}
\tilde{g}_i^{(+)} &= \frac{1}{2ar_i}\Big(e^{r_i/a}-e^{-r_i/a}\Big)\sum_{k=i}^{N-1}\int_{r_k}^{r_{k+1}} g(r)re^{-r/a}\,dr \\
&= f_i^{(+)}\tilde{g}_{i+1}+\frac{1}{2ar_i}\Big(e^{r_i/a}-e^{-r_i/a}\Big)\int_{r_i}^{r_i+\Delta} g(r)re^{-r/a}\,dr \\
&= f_i^{(+)}\tilde{g}_{i+1}+w_{7i}g_{i-1}+w_{8i}g_i+w_{9i}g_{i+1}\,,
\end{aligned}
\tag{A.30}
$$

where

$$
\begin{aligned}
f_i^{(+)} &= \frac{r_i+\Delta}{r_i}\frac{e^{r_i/a}-e^{-r_i/a}}{e^{(r_i+\Delta)/a}-e^{-(r_i+\Delta)/a}} \\
w_{7i} &= \frac{a\cosh(r_i/a)e^{-(r_i+\Delta)/a}}{2\Delta^2 r_i} \\
&\quad\times\left[-6a^2-\Delta(\Delta+r_i)-2a(2\Delta+r_i)+e^{\Delta/a}\Big(6a^2-\Delta r_i+2a(-\Delta+r_i)\Big)\right], \\
w_{8i} &= \frac{\cosh(r_i/a)e^{-(r_i+\Delta)/a}}{\Delta^2 r_i} \\
&\quad\times\left[e^{\Delta/a}\Big(-6a^3+a\Delta^2-2a^2r_i+\Delta^2 r_i\Big)+2a\Big(3a^2+\Delta(\Delta+r_i)+a(3\Delta+r_i)\Big)\right], \\
w_{9i} &= \frac{\cosh(r_i/a)e^{-(r_i+\Delta)/a}}{2\Delta^2 r_i} \\
&\quad\times\left[ae^{\Delta/a}\Big(6a^2+\Delta r_i+2a(\Delta+r_i)\Big)\right. \\
&\qquad\left.-\Big(6a^3+2\Delta^2(\Delta+r_i)+2a^2(4\Delta+r_i)+a\Delta(5\Delta+3r_i)\Big)\right].
\end{aligned}
\tag{A.31}
$$

The initial points for $g_0^{(-)}$ and $g_N^{(+)}$ are given by

$$
g_0^{(-)}=0, \qquad g_N^{(+)}=0\,. \tag{A.32}
$$

Since $g_1^{(-)}$ and $g_0^{(+)}$ can't have 3 points for numerical derivative, we use the first derivative so

$$
\begin{aligned}
g_1^{(-)} &= \frac{1}{2a\Delta}e^{-\Delta}\int_0^\Delta g(r)r\big(e^{r/a}-e^{-r/a}\big)dr \\
&= \frac{1}{2a\Delta}e^{-\Delta}\int_0^\Delta\left[g_0+\frac{g_1-g_0}{\Delta}r\right]r\big(e^{r/a}-e^{-r/a}\big)dr \\
&= \frac{ae^{-\Delta/a}\Big[2a-2a\cosh(\Delta/a)+\Delta\sinh(\Delta/a)\Big]}{\Delta^2}g_0 \\
&\quad+\frac{e^{-\Delta/a}\Big[(2a^2+\Delta^2)\cosh(\Delta/a)-2a\Big(a+\Delta\sinh(\Delta/a)\Big)\Big]}{\Delta^2}g_1\,.
\end{aligned}
\tag{A.33}
$$

$$
\tilde{g}_0^{(+)} = f_0^{(+)}\tilde{g}_1^{(+)}+\frac{1}{2ar_0}\Big(e^{r_0/a}-e^{-r_0/a}\Big)\int_0^\Delta g(r)re^{-r/a}\,dr\,, \tag{A.34}
$$

By expanding $e^{r_0/a} - e^{-r_0/a}$ in terms of r_0, we have

$$f_0^{(+)} = \frac{2\Delta}{a} \frac{1}{e^{\Delta/a} - e^{-\Delta/a}}\,, \tag{A.35}$$

and the integration becomes

$$\begin{aligned}
\tilde{g}_0^{(+)} &= f_0^{(+)} \tilde{g}_1^{(+)} + \frac{1}{a^2} \int_0^{\Delta} g(r) r e^{-r/a}\, dr \\
&= f_0^{(+)} \tilde{g}_1^{(+)} + \frac{1}{a^2} \int_0^{\Delta} \left[g_0 + \frac{g_1 - g_0}{\Delta} r \right] r e^{-r/a}\, dr \\
&= f_0^{(+)} \tilde{g}_1^{(+)} + \frac{e^{-\Delta/a}\left[2a + \Delta + (-2a + \Delta) e^{\Delta/a} \right]}{\Delta} g_0 \\
&\qquad + \frac{2a^2 - (2a^2 + 2a\Delta + \Delta^2) e^{-\Delta/a}}{a\Delta} g_1\,.
\end{aligned} \tag{A.36}$$

Fig A.1.2 shows the result of ^{56}Fe binding energy calculation as a function of number of grids. The nuclear force used is FRTF II. The energy converges quickly if we use 2nd order Taylor expansion. The right panel shows the log scale error and the error of 2nd order Taylor expansion is less than 0.1% even in the 40 zones. These method is also used to find

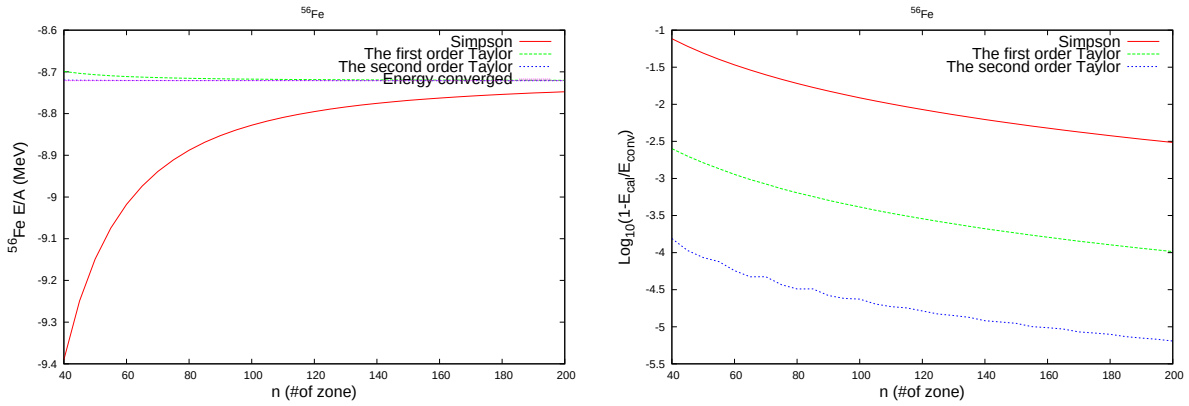

Figure A.2: ^{56}Fe binding energy calculation and relative error in log scale. The Simpson method doesn't give the enough accuracy even in N=200.

the properties of heavy nuclei in the dense matter.

Appendix B

JEL thermodynamic integration

To compute the properties of finite-temperature matter, it is necessary to calculate the Fermi integrals $F_{1/2}$ and $F_{3/2}$. Directly calculating these integrals by usual integral methods is not advisable for applications like hydrodynamics, which require a high degree of thermodynamic consistency. The approach we adopt is due to Johns, Ellis & Lattimer[12] (hereafter referred to as JEL), which is a modification of a less accurate scheme originated by Eggleton, Faulkner & Flannery[8]. These approaches involve polynomial interpolations for arbitrary degeneracy and relativity. However, in the finite-range model, nucleons are treated non-relativistically, so the interpolation method can be considerably simplified from the general case.

The degeneracy parameter Ψ, and an associated variable f, are defined in terms of the chemical potential and temperature as

$$\Psi = \frac{\mu - V}{T} = 2\sqrt{1 + \frac{f}{a}} + \ln \frac{\sqrt{1 + f/a} - 1}{\sqrt{1 + f/a} + 1}, \tag{B.1}$$

such that

$$f' = \frac{df}{d\Psi} = \frac{f}{\sqrt{1 + f/a}}. \tag{B.2}$$

In the above, a is a fitting parameter and is given in table B. The Fermi integrals are expressed as polynomials in f with additional parameters p_m, where $m = 0 \ldots M$, that are fixed by the requirements of yielding exact results for the pressure, energy and entropy in the extremely degenerate and non-degenerate limits or by fitting intermediate results. Using

M	3		2
a	0.433		1
p_0	$(e^2/a)\sqrt{\pi/32} = 5.34689$		$(e^2/a)\sqrt{\pi/32} = 2.31520$
p_1	16.8441		$a^{-1/4}[\pi^2 - 8 + 56/(5a)]/3 = 44.35653$
p_2	$a^{-1/4}[\pi^2 - 8 + 88/(5a)]/3 = 17.4708$		$32a^{-5/4}/15 = 2.13333$
p_3	$32a^{-5/4}/15 = 6.07364$		—

Table B.1: Non-relativistic fermion coefficients

the results of JEL, one finds

$$\begin{aligned}
F_{3/2}(\Psi) =& \frac{3f(1+f)^{1/4-M}}{2^{3/2}} \sum_{m=0}^{M} p_m f^m, \\
F_{1/2}(\Psi) =& \frac{f'(1+f)^{1/4-M}}{\sqrt{2}} \sum_{m=0}^{M} p_m f^m \left[1 + m - (M - \frac{1}{4})\frac{f}{1+f}\right], \\
F_{-1/2}(\Psi) =& -\frac{f'}{f+a} F_{1/2}(\Psi) \\
&+ \sqrt{2}\frac{f(1+f)^{1/4-M}}{1+f/a} \sum_{m=0}^{M} p_m f^m \left[(1+m)^2 - \right. \\
&\left. - (M - \frac{1}{4})\frac{f}{1+f}(3 + 2m - (M + \frac{3}{4})\frac{f}{1+f})\right].
\end{aligned} \tag{B.3}$$

The parameters are given in Table B for two cases, $M = 2$ and 3. With the 1 free parameter of the $M = 2$ scheme (i.e., a), accuracy is better than 3%. With the 2 free parameters of the $M = 3$ scheme, *i.e.*, a and p_1, accuracy improves about 100-fold.

For EOS table, we have a large range of temperature and density, so the electron can have four different regimes such as, non-relativistic non-degenerate, non-relativistic degenerate, relativistic non-degenerate, and relativistic degenerate. We treat electrons as non-interacting fermions except for the Coulomb interaction. In this case, we add another parameter g to account for relativistic effects. Then the pressure from electrons can be written, as

$$p = \frac{m_e}{\pi^2}\left(\frac{m_e}{\hbar}\right)^3 \frac{f g^{5/3}}{(1+f)^M (1+g)^{N-3/2}} \sum p_{mn} f^m g^n \,, \tag{B.4}$$

where

$$g = \frac{T}{m_e}\sqrt{1+f}\,, \tag{B.5}$$

and the electron's degeneracy parameter is given eq. (B.1). The coefficient p_{mn} is provided in Ref.[12].
Among the thermodynamic quantities in EOS table, we may calculate $\partial p/\partial n$, $\partial p/\partial T$, and

p_{mn}	$n=0$	$n=1$	$n=2$	$n=3$
$m=0$	5.34689	18.0517	21.3422	8.53240
$m=1$	16.8441	55.7051	63.6901	24.6213
$m=2$	17.4708	56.3902	62.1319	23.2602
$m=3$	6.07364	18.9992	20.0285	7.11153

Table B.2: Fermion coefficients p_{mn} for $M=N=3$; a=0.433

$\partial s/\partial T$. In JEL scheme, we treat f, g variables independent.

$$\begin{aligned} dp =& \frac{\partial p}{\partial f} df + \frac{\partial p}{\partial g} dg \\ dn =& \frac{\partial n}{\partial f} df + \frac{\partial n}{\partial g} dg \\ dt =& \frac{\partial t}{\partial f} df + \frac{\partial t}{\partial g} dg \,, \end{aligned} \tag{B.6}$$

where

$$t = \frac{T}{m_e c^2} \,, \quad g = t(1+f)^{1/2} \,. \tag{B.7}$$

The $\partial p/\partial n$ can be obtained when we make $dt=0$, then

$$\frac{\partial p}{\partial n} = \frac{\frac{\partial p}{\partial f} + \frac{\partial p}{\partial g}\frac{\partial g}{\partial f}}{\frac{\partial n}{\partial f} + \frac{\partial n}{\partial g}\frac{\partial g}{\partial f}} \,, \quad \text{where} \quad \frac{\partial g}{\partial f} = -\frac{\frac{\partial t}{\partial f}}{\frac{\partial t}{\partial g}} \tag{B.8}$$

In this manner, we can show that

$$\frac{\partial p}{\partial t} = \frac{\frac{\partial p}{\partial f} + \frac{\partial p}{\partial g}\frac{\partial g}{\partial f}}{\frac{\partial t}{\partial f} + \frac{\partial t}{\partial g}\frac{\partial g}{\partial f}} \,, \quad \text{where} \quad \frac{\partial g}{\partial f} = -\frac{\frac{\partial n}{\partial f}}{\frac{\partial n}{\partial g}} \,. \tag{B.9}$$

For $\partial S/\partial T$, we have

$$\frac{\partial S}{\partial T} = \frac{g}{T}\left[\frac{g}{T}\frac{\partial^2 p}{\partial g^2} - \psi\frac{\partial n}{\partial g}\right] . \tag{B.10}$$

We can find the derivative of $\partial p/\partial f$ and $\partial p/\partial g$ from eq. (B.4)

$$\begin{aligned} \frac{\partial p}{\partial f} &= \frac{mc^2 n_c\, g^{5/2}}{(1+f)^{M+2}(1+g)^{N-3/2}} \sum p_{mn} f^m g^n \big[1 + m + f(m-M)\big] \\ \frac{\partial p}{\partial g} &= \frac{mc^2 n_c\, f g^{3/2}}{(1+f)^{M+1}(1+g)^{N-1/2}} \sum p_{mn} f^m g^n \left[n + \frac{5}{2} + g(4+n-N)\right] , \end{aligned} \tag{B.11}$$

where $n_c = \frac{1}{\pi^2}\left(\frac{mc}{\hbar}\right)^3$.
We also need to find the derivatives of $\partial^2 p/\partial f^2$, $\partial^2 p/\partial f \partial g$, and $\partial^2 p/\partial g^2$. In this case, instead

of find exact polynomial expression, we might use recursion relation, that is,

$$\begin{aligned}
\frac{\partial^2 p}{\partial f^2} =& -\frac{M+2}{1+f}\frac{\partial p}{\partial f} + \frac{mc^2 n_c\, g^{5/2}}{(1+f)^{M+2}(1+g)^{N-3/2}}\times \\
& \sum p_{mn} f^m g^n \left[\frac{(1+m)m}{f} + m(m-M) + m - M\right], \\
\frac{\partial p^2}{\partial f \partial g} =& \left(\frac{1}{f} - \frac{M+1}{1+f}\right)\frac{\partial p}{\partial g} + \frac{mc^2 n_c\, g^{3/2}}{(1+f)^{M+1}(1+g)^{N-1/2}}\times \\
& \sum p_{mn} f^m g^n m\left[n + \frac{5}{2} + g(4+n-N)\right], \\
\frac{\partial^2 p}{\partial g^2} =& \left(\frac{3}{2g} - \frac{N-\frac{1}{2}}{1+g}\right)\frac{\partial p}{\partial g} + \frac{mc^2 n_c\, f g^{3/2}}{(1+f)^{M+1}(1+g)^{N-1/2}}\times \\
& \sum p_{mn} f^m g^n \left[\frac{n(n+\frac{5}{2})}{g} + n(4+n-N) + (4+n-N)\right].
\end{aligned} \tag{B.12}$$

From thermodynamic quantities, we can get

$$\begin{aligned}
n =& \frac{1}{T}\left(\frac{\partial p}{\partial \psi}\right)_T = \frac{1}{T}\frac{\partial f}{\partial \psi}\left(\frac{\partial p}{\partial f} + \frac{\partial g}{\partial f}\frac{\partial p}{\partial g}\right) \\
=& \frac{1}{mc^2}\left(\frac{1}{g}\frac{f\sqrt{1+f}}{1+f/a}\frac{\partial p}{\partial f} + \frac{f}{2\sqrt{1+f}\sqrt{1+f/a}}\frac{\partial p}{\partial g}\right) \\
ns =& \left(\frac{\partial p}{\partial T}\right)_\psi - n\psi = \frac{\sqrt{1+f}}{mc^2}\frac{\partial p}{\partial g} - n\psi\,.
\end{aligned} \tag{B.13}$$

The derivatives of the above items w.r.t f and g are given by

$$\begin{aligned}
\frac{\partial n}{\partial f} =& \left(\frac{1}{f} - \frac{1}{2a(1+f/a)}\right)n + \frac{1}{mc^2}\frac{f}{2g\sqrt{1+f}\sqrt{1+f/a}}\times \\
& \left(\frac{\partial p}{\partial f} + 2(1+f)\frac{\partial^2 p}{\partial f^2} - \frac{1}{2}\frac{g}{1+f}\frac{\partial p}{\partial g} + g\frac{\partial^2 p}{\partial f \partial g}\right), \\
\frac{\partial n}{\partial g} =& \frac{1}{mc^2}\frac{f}{\sqrt{1+f/a}}\left(-\frac{\sqrt{1+f}}{g^2}\frac{\partial p}{\partial f} + \frac{\sqrt{1+f}}{g}\frac{\partial^2 p}{\partial f \partial g} + \frac{1}{2\sqrt{1+f}}\frac{\partial^2 p}{\partial g^2}\right), \\
\frac{\partial (ns)}{\partial f} =& \frac{1}{2mc^2}\frac{1}{\sqrt{1+f}}\frac{\partial p}{\partial g} + \frac{\sqrt{1+f}}{mc^2}\frac{\partial^2 p}{\partial f \partial g} - \psi\frac{\partial n}{\partial f} - n\frac{\sqrt{1+f/a}}{f}, \\
\frac{\partial (ns)}{\partial g} =& \frac{\sqrt{1+f}}{mc^2}\frac{\partial^2 p}{\partial g^2} - \frac{\partial n}{\partial g}\psi\,.
\end{aligned} \tag{B.14}$$

Finally we can get thermodynamic derivatives using the above formulae and constraints

with differentials,

$$\begin{aligned}
\left(\frac{\partial p}{\partial n}\right)_T &= \left(\frac{\partial p}{\partial f} + \frac{g}{2(1+f)}\frac{\partial p}{\partial g}\right)\left(\frac{\partial n}{\partial f} + \frac{g}{2(1+f)}\frac{\partial n}{\partial g}\right)^{-1} \\
\left(\frac{\partial p}{\partial T}\right)_n &= -\frac{\sqrt{1+f}}{mc^2}\left(\frac{\partial p}{\partial f} - \frac{\partial p}{\partial g}\frac{\partial n}{\partial f}\left(\frac{\partial n}{\partial g}\right)^{-1}\right)\left(\frac{g}{2(1+f)} + \frac{\partial n}{\partial f}\left(\frac{\partial n}{\partial g}\right)^{-1}\right)^{-1} \\
\left(\frac{\partial (ns)}{\partial T}\right)_n &= -\frac{\sqrt{1+f}}{mc^2}\left(\frac{\partial (ns)}{\partial f} - \frac{\partial (ns)}{\partial g}\frac{\partial n}{\partial f}\left(\frac{\partial n}{\partial g}\right)^{-1}\right)\left(\frac{g}{2(1+f)} + \frac{\partial n}{\partial f}\left(\frac{\partial n}{\partial g}\right)^{-1}\right)^{-1}
\end{aligned} \tag{B.15}$$

Appendix C

Phase coexistence

Bulk equilibrium of dense and dilute matter is the simplified case of heavy nuclei and nucleon gas in neutron stars' inner crust. This bulk equilibrium can be made by the free energy minimization process.
For given density, we have total free energy density

$$\begin{aligned} F =& uF_I(\rho_I) + (1-u)F_{II}(\rho_{II})\,, \\ \rho =& u\rho_I + (1-u)\rho_{II} \end{aligned} \tag{C.1}$$

where u is the volume fraction of phase I and F_I and F_{II} are free energy density of each phase. The free energy density should be minimized with respect to u, $\rho_I(\rho_{II})$. Then we have

$$\begin{aligned} \frac{\partial F}{\partial \rho_I} =& u\frac{\partial F_I}{\partial \rho_I} + (1-u)\frac{\partial F_{II}}{\partial \rho_{II}}\frac{\partial \rho_{II}}{\partial \rho_I} = u(\mu_I - \mu_{II}) = 0\,, \\ \frac{\partial F}{\partial u} =& F_I - F_{II} + (1-u)\frac{\partial F_I}{\partial \rho_I}\frac{\partial \rho_{II}}{\partial u} \\ =& F_I - F_{II} + (1-u)\frac{\partial F_{II}}{\partial \rho_{II}}\frac{\rho_{II}-\rho_I}{(1-u)} = 0 \end{aligned} \tag{C.2}$$

From eq (C.2), we have $\mu_I = \mu_{II}$ and $p_I = p_{II}$. In case of neutron and proton matter, this can be generalized as

$$\mu_{nI} = \mu_{nII}\,, \quad \mu_{pI} = \mu_{pI}\,, \quad p_I = p_{II}\,. \tag{C.3}$$

To find the mixed phase of quark and nuclear matter, we use a similar method in nuclear matter cases.

$$F = F_N u + F_Q(1-u) + \frac{3}{4}\hbar c(3\pi^2\rho_N x_N)^{1/3}\rho_N x_N u + \frac{3}{4}\hbar c(3\pi^2\rho_Q x_Q)^{1/3}\rho_Q x_Q(1-u)\,, \tag{C.4}$$

where F is the free energy density, u is the volume fraction of the nuclear matter, ρ_N is the nuclear matter density, ρ_Q is the quark matter density, x_N is electron fraction of nuclear

matter, and x_Q is electron fraction of quark matter. There are two constrains which are

$$\begin{aligned} \rho_B &= \rho_N u + \rho_Q (1-u) \\ \rho_B Y_e &= \rho_N x_N u + \rho_Q x_Q (1-u)\,. \end{aligned} \tag{C.5}$$

We set $G(\rho_N, \rho_Q, x_N, x_Q, u)$

$$\begin{aligned} G(\rho_N, \rho_Q, x_N, x_Q, u) =& F - \alpha(\rho_B - \rho_N u + \rho_Q(1-u)) \\ & - \beta(\rho_B Y_e - \rho_N x_N u + \rho_Q x_Q (1-u))\,, \end{aligned} \tag{C.6}$$

and find the minimum of F using Lagrangian multiplier method.
$\partial G/\partial x_N$ gives

$$\beta = -\mu_{e,N} \tag{C.7}$$

From $\partial G/\partial x_Q = 0$, we have

$$\mu_{e,N} = \mu_{e,Q}\,. \tag{C.8}$$

With ρ_N and ρ_Q, we have

$$\frac{\partial G}{\partial \rho_N} = \; u + \hbar c (3\pi^2 \rho_N x_N)^{1/3} x_N u + \alpha u + \beta x_N u = 0\,, \tag{C.9}$$

thus

$$\frac{\partial F_N}{\partial \rho_N} = \frac{\partial F_Q}{\partial \rho_Q} = -\alpha\,. \tag{C.10}$$

Furthermore, we get

$$\frac{\partial F_N}{\partial \rho_N} = \frac{\partial \rho_n}{\partial \rho_N}\frac{\partial F_N}{\partial \rho_n} + \frac{\partial \rho_p}{\partial \rho_N}\frac{\partial F_N}{\partial \rho_p} = (1-x_N)\mu_n + x_N \mu_p \tag{C.11}$$

and

$$\begin{aligned} \frac{\partial F_Q}{\partial \rho_Q} &= \frac{\partial \rho_u}{\partial \rho_Q}\frac{\partial F_Q}{\partial \rho_u} + \frac{\partial \rho_d}{\partial \rho_Q}\frac{\partial F_Q}{\partial \rho_d} + \frac{\partial \rho_s}{\partial \rho_Q}\frac{\partial F_Q}{\partial \rho_s} \\ &= (1+x_Q)\mu_u + \frac{1}{2}(2-x_Q)\mu_d + \frac{1}{2}(2-x_Q)\mu_s \\ &= \mu_u + \mu_d + \mu_s + x_Q(\mu_u - \frac{1}{2}\mu_d - \frac{1}{2}\mu_s) \\ &= \mu_u + 2\mu_d + x_Q(\mu_u - \mu_d) \end{aligned} \tag{C.12}$$

where we have used massless quark limits. Therefore

$$(1-x_N)\mu_n + x_N \mu_p = \mu_u + 2\mu_d + x_Q(\mu_u - \mu_d)\,. \tag{C.13}$$

The partial derivative of G w.r.t u simply gives pressure equations which are

$$F_N - \rho_N \frac{\partial F_N}{\partial \rho_N} = p_N = F_Q - \rho_Q \frac{\partial F_Q}{\partial \rho_Q} = p_Q\,. \tag{C.14}$$

To summarize, we need to solve 5 equations, which are

$$\begin{aligned}
(1-x_N)\mu_n + x_N\mu_p &= \mu_u + 2\mu_d + x_Q(\mu_u - \mu_d)\,, \\
\mu_{e,N} &= \mu_{e,Q}\,, \\
p_N &= p_Q\,, \\
\rho_B &= \rho_N u + \rho_Q(1-u)\,, \\
\rho_B Y_e &= \rho_N x_N u + \rho_Q x_Q(1-u)\,,
\end{aligned} \tag{C.15}$$

with 5 unknowns,

$$\rho_N\,, \rho_Q\,, x_N\,, x_Q\,, u\,. \tag{C.16}$$

The above equations and unknown can be solved numerically using typical Newton-Raphson method.

Appendix D

Numerical Techniques in Heavy Nuclei in Dense Matter

The heavy nuclei in dense matter exist in the narrow range of densities ($2.0 \times 10^{-4} \sim 8.0 \times 10^{-2}/\mathrm{fm}^3$). However, this is the most difficult part of calculations in FRTF model and Nuclear E.O.S. table. We now explain the numerical techniques in FRTF model.
The total energy in the cell can be obtained from

$$E_{tot} = \int \mathcal{E}_{np} + \mathcal{E}_e + \mathcal{E}_C \, d^3r \,, \tag{D.1}$$

where $\mathcal{E}_n p$ is a nuclear energy density and

$$\mathcal{E}_c = \frac{m_e^4}{8\pi^2(\hbar c)^3}\Big[x_e(2x_e^2+1)\sqrt{x_e^2+1} - \ln(x_e + \sqrt{1+x_e^2})\Big] \tag{D.2a}$$

$$\mathcal{E}_C = \frac{1}{2}(\rho_p - \rho_e)\Delta\mu_p(r) \,. \tag{D.2b}$$

Here,

$$x_e = \frac{\hbar c}{m_e}(3\pi^2\rho_e)^{1/3} \,, \tag{D.3}$$

and

$$\Delta\mu_p = 4\pi e^2\Big[\frac{1}{r}\int_0^r r'^2\big[\rho_p(r') - \rho_e(r')\big]\,dr' + \int_r^{R_c} r'\big[\rho_p(r') - \rho_e(r')\big]\,dr'\Big] \,. \tag{D.4}$$

If we assume that the inner cell or numerical boundary (R_b) for computational purpose is smaller than the actual Wigner-Seitz cell and the nuclear and electron densities are constant outside the inner cell, then we have ($r < R_b < R_c$)

$$\begin{aligned}\Delta\mu_p(r) =& 4\pi e^2\Big[\frac{1}{r}\int_0^r r'^2\big[\rho_p(r') - \rho_e(r')\big]\,dr' + \int_r^{R_b} r'\big[\rho_p(r') - \rho_e(r')\big]\,dr'\Big] \\ & - 2\pi e^2\rho_{e,o}(R_c^2 - R_b^2) \,.\end{aligned} \tag{D.5}$$

D.1 Non-uniform electron density approximation

Total energy contribution from the outer cell [†] is given by

$$E_{tot,o} = \frac{4\pi}{3}(R_c^3 - R_b^3)(\mathcal{E}_{np,o} + \mathcal{E}_{e,o}) - \frac{1}{2}\int_{R_b,R_c} \rho_{e,o}\Delta\mu_p(r)\, d^3r\,, \tag{D.6}$$

For $R_b < r < R_c$,

$$\Delta\mu_p(r) = \frac{e^2}{r}(z - z_e') - \frac{2\pi}{3}e^2\rho_{e,o}\Big(3R_c^2 - 2\frac{R_b^3}{r} - r^2\Big) \tag{D.7}$$

where z_e' is the total number of electrons in the inner cell. Then we can have

$$E_{C,o} = -\pi e^2(z - z_e')\rho_{e,o}(R_c^2 - R_b^2) + \frac{8\pi^2}{15}\rho_{e,o}^2(2R_c^5 - 5R_c^2R_b^3 + 3R_b^5) \tag{D.8}$$

For energy minimization,

$$F = \int \mathcal{E}_{tot} - \lambda_1\Big(\int(\rho_n + \rho_p)\, d^3r - \frac{4\pi}{3}R_c^3\rho\Big) - \lambda_2\Big(\int \rho_p\, d^3r - \int \rho_e\, d^3r\Big) \tag{D.9}$$

I chose unknowns with ρ_n, ρ_p, ρ_e, and $\lambda_{1,2}$, then we have equations to solve

$$\begin{aligned}
0 = F_{0,N}: &\quad \mu_n(\rho_n,\rho_p) - \mu_{n,0} = 0\\
0 = F_{N+1,2N+1}: &\quad \mu_p(\rho_n,\rho_p) + \Delta\mu_p(\rho_p,\rho_e) - \mu_{n,0} + \mu_{e,0} = 0\\
0 = F_{2N+2,3N+2}: &\quad \mu_e(\rho_p,\rho_e) - \Delta\mu_p(\rho_p,\rho_e) - \mu_{e,0} = 0\\
0 = F_{3N+3}: &\quad \int(\rho_n + \rho_p)d^3r - \frac{4}{3}\pi R_c^3\rho = 0\\
0 = F_{3N+4}: &\quad \int \rho_p d^3r - \int \rho_e d^3r = 0
\end{aligned} \tag{D.10}$$

D.2 Uniform electron density approximation

In case of constant electron density approximation,

$$\begin{aligned}
\Delta\mu_p(r) =& 4\pi e^2\Big[\frac{1}{r}\int_0^r r'^2\rho_p(r')\, dr' + \int_r^{R_b} r'\rho_p(r')\, dr'\Big]\\
&- \frac{2}{3}\pi e^2\rho_e(3R_c^2 - r^2)\,.
\end{aligned} \tag{D.11}$$

[†]We divide the Wigner-Seitz cell by inner cell and outer cell. In the inner cell, the nuclear density profile varies. On the other hand, the nuclear density profile is uniform in the outer cell. The radius for inner cell is set to 15 fm for the numerical calculations.

For $R_b < r < R_c$, we have

$$\Delta\mu_p(r) = \frac{ze^2}{r} - \frac{2}{3}\pi e^2\rho_e(3R_c^2 - r^2)\,. \tag{D.12}$$

The energy contribution from outside the inner cell is given by

$$E_{C,o} = -\pi z\rho_e e^2(R_c^2 - R_b^2) + \frac{4\pi^2}{15}\rho_e^2(4R_c^5 - 5R_c^2R_b^3 + R_b^5)\,. \tag{D.13}$$

For energy minimization, we have

$$F = \int \mathcal{E}_{tot} - \lambda_1\Big(\int(\rho_n + \rho_p)\,d^3r - \frac{4\pi}{3}R_c^3\rho\Big) - \lambda_2\Big(\int \rho_p\,d^3r - \frac{4\pi}{3}R_c^3\rho Y_e\Big) \tag{D.14}$$

I chose unknowns with ρ_n, ρ_p, Y_e, $\mu_{n,0}$, and $\mu_{p,0}$ then we have equations to solve

$$\begin{aligned}
0 = F_{0,N}: &\quad \mu_n(\rho_n,\rho_p) - \mu_{n,0} = 0\\
0 = F_{N+1,2N+1}: &\quad \mu_p(\rho_n,\rho_p) - \mu_{p,0} = 0\\
0 = F_{2N+2}: &\quad \int(\rho_n+\rho_p)d^3r - \frac{4}{3}\pi R_c^3\rho = 0\\
0 = F_{2N+3}: &\quad \int \rho_p\,d^3r - \frac{4}{3}\pi R_c^3\rho Y_e = 0\\
0 = F_{2N+4}: &\quad \mu_{n,0} - \mu_{p,0} - \mu_e(Y_e) = 0
\end{aligned} \tag{D.15}$$

In the lower density ($\rho < 0.01/\mathrm{fm}^3$) region, two methods give almost same result. As density increases, the uniform electron density approximation is unstable numerically in FRTF model.

Appendix E

Nuclear Quantities in Non-relativistic Models

We present nuclear properties of non-relativistic potential (Skyrme force) models. These properties can be used to restrict nuclear parameters when we make new force models.

E.1 Mathematical relation between nuclear parameters and quantities

Once we are given nuclear parameters ($x_0, \ldots, x_3$, $t_0, \ldots, t_3$) in Skyrme force model, we can extract nuclear quantities (B, K, M^*, S_v, L, ρ_o) from its mathematical expression of bulk matter Hamiltonian density[32].
In the standard Skyrme force models,

$$\frac{p(\rho_o)}{\rho_o} = 0 = \frac{2}{3}C\rho_o^{2/3}\left(1+\frac{5}{2}\beta\rho_o\right) + \frac{3}{8}t_0\rho_o + \frac{t_3}{16}(\epsilon+1)\rho_o^{\epsilon+1}\,, \tag{E.1}$$

where

$$C = \frac{3\hbar^2}{10M}\left(\frac{3\pi^2}{2}\right)^{2/3}\;; \qquad \beta = \frac{M}{2\hbar^2}\left[\frac{1}{4}(3t_1+5t_2)+t_2x_2\right]\,. \tag{E.2}$$

From the pressure expression, we can get ρ_o using the Newton-Raphson method, with which we can get the binding energy per baryon, effective mass, and nuclear incompressibility in standard nuclear matter,

$$\begin{aligned} B &= -\frac{E}{A} = -C\rho_o^{2/3}(1+\beta\rho_o) - \frac{3t_0}{8}\rho_o - \frac{t_3}{16}\rho_o^{1+\epsilon}\,, \\ M^* &= \frac{M}{1+\beta\rho_o}\,, \\ K &= 9\rho^2\frac{\partial^2 E/A}{\partial\rho^2}\Big|_{\rho=\rho_o} = -2C\rho_o^{2/3} + 10C\rho_o^{5/3} + \frac{9t_3}{16}\epsilon(\epsilon+1)\rho_o^{\epsilon+1}\,. \end{aligned} \tag{E.3}$$

Other important quantities, S_v and L can be obtained

$$\begin{aligned} S_v = \frac{\rho_o^2}{8}\frac{\partial^2 E/A}{\partial x^2} &= \frac{5}{9}C\rho_o^2 + \frac{10CM}{3\hbar^2}\left[\frac{t_2}{6}\left(1+\frac{5}{4}x_2\right) - \frac{1}{8}t_1x_1\right]\rho_o^{5/3} \\ &\quad - \frac{t_3}{24}\left(\frac{1}{2}+x_3\right)\rho_o^{1+\epsilon} - \frac{t_o}{4}\left(\frac{1}{2}+x_o\right)\rho_o\,, \\ L = \frac{3\rho_o}{8}\frac{\partial^3 E/A}{\partial\rho\partial x^2}\Big|_{\rho=\rho_o,x=1/2} &= \frac{10}{27}C\rho_o^2 + \frac{50CM}{9\hbar^2}\left[\frac{t_2}{6}\left(1+\frac{5}{4}x_2\right) - \frac{1}{8}t_1x_1\right]\rho_o^{5/3} \\ &\quad - \frac{t_3}{24}(1+\epsilon)\left(\frac{1}{2}+x_3\right)\rho_o^{1+\epsilon} - \frac{t_o}{4}\left(\frac{1}{2}+x_o\right)\rho_o\,, \end{aligned} \tag{E.4}$$

In this way, we can obtain nuclear quantities in standard Skyrme force model.
As an inverse process to find $x_0, \ldots, t_3$ in Skyrme force model, we can use E/A, $p(\rho_o, x = 1/2) = 0$, $M*$, K, S_v, L, and ρ_o. Since we only have 7 quantities for 8 parameters, we may use the pure neutron matter effective mass M_n^* or the energy difference $Q_1 = e_N - e_S - S_v$ as described in section (3.2).

The maximum mass of the cold neutron star can be obtained using T.O.V equation and varying the central density of neutron stars. To get a more precise maximum mass of neutron stars, we may use numerical Newton Rapshon with numerical derivative of

$$f = \frac{M_2 - M_1}{\rho_{c2} - \rho_{c1}} \tag{E.5}$$

and find the solution which makes $f = 0$.

Table E.1: Non-relativistic Skyrme force model and maximum mass of cold neutron star

Model	B (MeV)	S_v(MeV)	L (MeV)	K (MeV)	M^*/M	ρ_0 (fm^{-3})	M/M$_\odot$
Gs	-15.6023	31.3749	94.0305	237.3811	0.7838	0.1576	2.192
$M^*(0.811)$	-15.6992	30.7657	79.3938	237.1923	0.8110	0.1609	2.114
$M^*(0.9)$	-15.5659	27.7811	69.9636	240.2086	0.8957	0.1610	2.114
$M^*(1.0)$	-15.4172	24.8108	59.5481	240.2216	1.0000	0.1611	2.087
Rs	-15.6019	30.5851	85.7058	237.5088	0.7826	0.1578	2.177
SGI	-15.9073	28.3271	63.8631	261.9091	0.6078	0.1545	2.287
SGII	-15.6085	26.8270	37.6101	214.7885	0.7855	0.1584	1.663
SIV	-15.9733	31.2164	63.4859	324.7265	0.4707	0.1510	2.391
Ska	-16.0055	32.9103	74.6226	263.3100	0.6082	0.1554	2.244
SkI1	-15.9660	37.5327	161.0952	242.8726	0.6929	0.1604	2.242
SkI2	-15.7895	33.3788	104.3625	241.0820	0.6847	0.1576	2.255
SkI3	-15.9944	34.8366	100.5490	258.3483	0.5771	0.1578	2.339
SkI4	-15.9573	29.5010	60.3980	248.0753	0.6492	0.1602	2.236
SkI5	-15.8603	36.6487	129.3675	255.9506	0.5785	0.1558	2.349
SkI6	-15.9310	30.0894	59.7002	248.7457	0.6396	0.1591	2.245
SkkT8	-15.9571	29.9178	33.6999	235.8483	0.8326	0.1607	1.691
SkM	-15.7851	30.7446	49.3262	216.7496	0.7884	0.1604	1.680
SkM$'$	-15.5749	29.8860	70.3127	231.0207	0.6533	0.1571	2.148
SkM*	-15.7851	30.0312	45.7590	216.7496	0.7884	0.1604	1.618
SkT1	-15.9935	32.0171	56.1694	236.3034	1.0000	0.1611	1.849
SkT1s	-15.9921	32.0154	56.0964	236.1374	1.0000	0.1603	1.8517
SkT2	-15.9581	31.9977	56.1523	235.8796	1.0000	0.1611	1.848
SkT3	-15.9592	31.4965	55.3027	235.8903	1.0000	0.1611	1.854
SkT3s	-15.9924	31.6811	55.8395	236.1412	1.0000	0.1603	1.860
SkT4	-15.9694	35.4579	94.1479	235.6446	1.0000	0.1591	2.128
SkT5	-16.0120	37.0107	98.5508	201.8260	1.0000	0.1641	1.920
SkT7	-15.9519	29.5138	31.0932	235.7859	0.8325	0.1607	1.431
SkT8	-15.9571	29.9178	33.6999	235.8483	0.8326	0.1607	1.698
SkT9	-15.8968	29.7525	33.7134	235.0521	0.8329	0.1604	1.704
SLy0	-15.9860	31.9800	47.1008	229.8049	0.6977	0.1604	2.067
SLy1	-15.9997	31.9905	47.0548	229.9593	0.6976	0.1604	2.067
SLy2	-16.0003	32.0018	47.4436	230.0627	0.6973	0.1606	2.068
SLy3	-15.9850	31.9894	45.2930	230.0423	0.6961	0.1605	2.057
SLy4	-15.9868	31.9986	45.9305	230.0602	0.6944	0.1596	2.070
SLy5	-15.9991	32.0080	48.1339	230.0656	0.6973	0.1606	2.070
SLy6	-15.9342	31.9555	47.4365	230.0047	0.6897	0.1590	2.090
SLy7	-15.9145	31.9861	46.9306	229.8984	0.6878	0.1584	2.090
SLy8	-15.9828	31.9934	47.1634	230.0383	0.6958	0.1604	2.070
SLy9	-15.8081	31.9814	54.8507	229.9855	0.6655	0.1512	2.200
SLy10	-15.9159	31.9775	38.7279	229.8270	0.6832	0.1556	2.056
SV	-16.0615	32.8243	96.1003	305.8488	0.3827	0.1551	2.510